Rotational Spectra of Elusive Molecules in the Laboratory and in Space

Silvia Spezzano
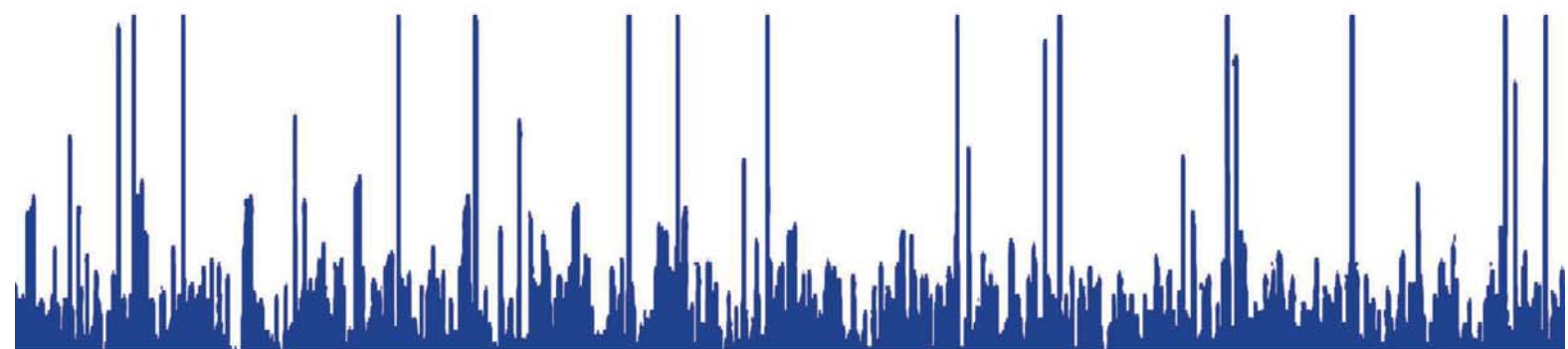
Rotational Spectra of Elusive Molecules in the Laboratory and in Space

Rotational Spectra of Elusive Molecules in the Laboratory and in Space

INAUGURAL-DISSERTATION

zur

Erlangung des Doktorgrades
der Mathematisch-Naturwissenschaftlichen Fakultät
der Universität zu Köln

vorgelegt von

Silvia Spezzano

aus Corigliano, Italien

Köln 2013

Berichterstatter: Prof. Dr. S. Schlemmer

                                     Prof. Dr. K. M. Menten

Tag der letzten mündlichen Prüfung: 9. Dezember 2013

Article 26

Everyone has the right to education. Education shall be free, at least in the elementary and fundamental stages. Elementary education shall be compulsory. Technical and professional education shall be made generally available and higher education shall be equally accessible to all on the basis of merit.

Education shall be directed to the full development of the human personality and to the strengthening of respect for human rights and fundamental freedoms. It shall promote understanding, tolerance and friendship among all nations, racial or religious groups, and shall further the activities of the United Nations for the maintenance of peace.

<div align="right">The Universal Declaration of Human Rights</div>

Abstract

Molecules are important tools to unveil the history, the structure and the evolution of the Universe. In this thesis I underline the importance of high resolution spectroscopy in the laboratory and in space, and the symbiotic bond between laboratory spectroscopy and radioastronomy. My work is divided in two parts. The first part concerns high resolution spectroscopy of unstable molecules in the laboratory. The second part deals with radioastronomical observations of deuterated molecules in dense cores.

CO^+ is the cation of the second most abundant molecule in space, carbon monoxide, and it is a good tracer of Photon-Dominated Regions (PDRs). In this work the rotational spectra of CO^+, $^{13}CO^+$ and $C^{18}O^+$ in the $v = 0$ and 1 vibrational states have been measured in the submillimeter-wave range. Furthermore, the first THz spectra of the main isotopic species have been measured in the course of this thesis. An isotopically invariant fit has been performed, and a set of independent molecular parameters has been derived. The measured and predicted high frequency transitions of CO^+ will guide new astronomical observations. Performing high resolution spectroscopy on ions is not trivial. The ions are unstable molecules and have to be produced in situ, at cryogenic temperatures by using a DC electrical discharge. An experimental setup to produce and probe ions in the laboratory, based on a new cryogenic discharge cell, has been developed and tested. The new experiment is reliable, the discharge cell is vacuum tighter and it has a better control of the temperature with respect to the one previously used for the production of CO^+. The new experiment is presented, and some possible implementations for the future are discussed.

The doubly deuterated cyclopropenylidene, c-C_3D_2, has been detected for the first time in space toward the starless cores TMC-1C and L1544. The chemistry of deuterated molecules in space is connected to the early stages of star formation. Having more probes to study these processes is therefore crucial. Lines of the main

species, c-C_3H_2, the singly deuterated c-C_3HD, and the species with one ^{13}C off of the principal axis of the molecule, c-$H^{13}CC_2H$, have also been detected. The lines of c-C_3D_2 have been observed with high signal-to-noise ratio, better than 7.5σ in TMC-1C and 9σ in L1544. The c-C_3D_2/c-C_3H_2 ratio is found to be around 1% in both sources. The chemistry that leads to the formation of c-C_3D_2 has been studied and is discussed in this thesis. The observed abundances of c-C_3D_2 can be explained solely by gas-phase processes, supporting the idea that c-C_3H_2 is an excellent probe of gas-phase deuteration. l-C_3HD is the monodeuterated isotopologue of the linear isomer of cyclopropenylidene, propadienylidene. l-C_3HD has been tentatively detected towards TMC-1C and L1544. One line of l-C_3HD has been observed both in TMC-1C and L1544. In order to confirm this detection, a proposal has been submitted to the IRAM 30 m telescope to observe one additional line. If this detection will be confirmed, this would be the first interstellar detection of this molecule. Furthermore, the observed ratio l-C_3HD/l-C_3H_2 is around 50% in TMC-1C and 30% in L1544. This deuteration ratio is the highest detected in space so far. If confirmed, it will put stringent constraints on the chemistry regulating deuterium fractionation.

Kurzzusammenfassung

Moleküle sind wichtige Botenstoffe zur Erkundung der Geschichte, Struktur und Evolution des Universums. In dieser Arbeit beleuchte ich die Bedeutung von hochauflösender Spektroskopie im Labor und im All, und die symbiotische Verbindung zwischen Laborspektroskopie und Radioastronomie. Meine Arbeit besteht aus zwei Teilen. Der erste Teil behandelt die hochauflösende Spektroskopie instabiler Moleküle im Labor. Der zweite Teil beschäftigt sich mit radioastronomischen Beobachtungen von deuterierten Molekülen in interstellaren Dunkelwolken.

CO^+ ist das Kation des zweithäufigsten Moleküls im Weltall, Kohlenmonoxid, und gilt als gutes Indikator-Molekül ("tracer") in sogenannten photonendominierten Gebieten (PDRs, "photon dominated regions"). In dieser Arbeit wurden die Rotationsspektren von CO^+, $^{13}CO^+$, und $C^{18}O^+$ in den Vibrationszuständen $v = 0$ und 1 im Submillimeter-Wellenlängenbereich gemessen. Zusätzlich wurden zum ersten Mal Terahertz (THz)-Spektren des Hauptisotopomers aufgenommen. Die gewonnenen Daten wurden an ein isotopen-invariantes Modell angepaßt, und unabhängige Molekülparameter wurden bestimmt. Die gemessenen und für höhere Frequenzen mit Hilfe des Modells berechneten CO^+ Übergangsfrequenzen können für neue astronomische Beobachtungen verwendet werden. Hochauflösende spektroskopische Untersuchungen an Ionen sind nicht leicht durchzuführen. Ionen sind instabile, reaktive Moleküle, die in situ bei kryogenen Temperaturen durch eine Gleichstrom-Entladung erzeugt werden müssen. Basierend auf einer neuen kryogenen Entladungs-Absorptionszelle wurde in dieser Arbeit ein Labor-Experiment zur Erzeugung und spektroskopischen Untersuchung von Ionen entwickelt und im Anschluss chrakterisiert. Der neue experimentelle Aufbau liefert im Vergleich zu einer zuvor für die Messungen an CO+ verwendeten Version deutlich reproduzierbarere Ergebnisse, da in der neuentwickelten Entladungszelle ein besseres

Vakuum erreicht werden kann, und sie außerdem eine verbesserte Temperaturkontrolle ermöglicht. Der neue Aufbau wird präsentiert, und mögliche zukünftige Verbesserungen und Erweiterungen werden diskutiert.

Doppelt deuteriertes Cyclopropenyliden (c-C_3D_2) wurde zum ersten Mal im All entdeckt, in den Dunkelwolken TMC-1C und L1544. Die Chemie interstellarer deuterierter Moleküle ist eng mit den frühen Phasen der Sternentstehung verbunden. Die Entdeckung neuer Indikator-Moleküle, wie c-C_3D_2, ist Voraussetzung zur Untersuchung der dort ablaufenden Prozesse. Es wurden außerdem Rotations-Linien des Hauptisotopomers, c-C_3H_2, sowie des einfach deuterierten c-C_3HD, und des einfach substituierten c-$H^{13}CC_2H$ detektiert. Linien von c-C_3D_2 wurden mit einem hohen Signal-zu-Rausch-Verhältnis beobachtet, größer als 7.5σ in TMC-1C und 9σ in L1544. Das Verhältnis von c-C_3D_2 zu c-C_3H_2 wurde in beiden Quellen zu etwa 1% bestimmt. Die Entdeckung von c-C_3D_2 und die seiner Bildung zugrundeliegenden chemischen Prozesse werden in dieser Arbeit diskutiert. Die beobachteten interstellaren Häufigkeiten von c-C_3D_2 können allein durch Gasphasen-Prozesse erklärt werden. Dadurch wird die Vermutung unterstützt, dass c-C_3H_2 sich hervorragend als Indikator-Molekül zur Untersuchung von Deuterierungs-Prozessen in der Gasphase eignet. l-C_3HD, das einfach deuterierte Isotopomer des linearen Isomers von Cyclopropenyliden, Propadienyliden, wurde eventuell in denselben Dunkelwolken entdeckt. Es wurde jeweils nur eine Rotationslinie detektiert. Um diese Detektion durch die Beobachtung einer weiteren Linie zu bestätigen wurde ein Antrag auf Beobachtungszeit am IRAM 30m Teleskop gestellt. Wenn die Identifizierung bestätigt wird, wäre es die Erstdetektion dieses Moleküls im interstellaren Medium. Das beobachtete Verhältnis von l-C_3HD zu l-C_3H_2 liegt bei etwa 50% in TMC-1C und etwa 30% in L1544. Diese Deuteriungsrate wäre die höchste bisher im All gemessene, so dass eine Bestätigung starke Bedingungen an die interstellare Deuteriums-Chemie stellen wird.

Contents

List of Figures

List of Tables

Chapter 1

Molecular Spectroscopy:
a Tool to Unveil the Universe

1.1   Spectroscopy and radioastronomy: symbiotic sciences

Most of the mass that composes the Universe is not molecular. Actually most of the mass that composes the Universe is not even baryonic material: dark matter counts for 90% of the mass of the Universe. Most of the remaining 10% is locked in stars, and just 1% of the total mass is gas distributed around the stars, the so-called Interstellar Medium (ISM), and half of it is molecular. The reason why studying the molecular composition of the Universe is important, is that astrophysical events such as galaxy, star, and planetary system formation happen in the dense parts of the Universe, which can be traced by molecules. The gas composing the ISM is at the same time the "exhaust" from old stars and galaxies, and the material that "feeds" the birth and growth of new galaxies, new stars, and eventually new planets. Understanding the chemistry that drives these phenomena is crucial to understand the phenomena themselves. The chemical inventory of a source, or of a source prototype, can unveil the evolution of the source itself. Furthermore molecules are tracers of physical properties such as temperature, density and the kinematics of astrophysical sources. For example, although it was quite disputed at the beginning of the 1970s [1, 2], the gravitational collapse that occurs prior to the formation of a star is traceable by the line profile of molecular transitions [3].

1

In order to interpret the steadily increasing amount of high resolution astronomical data, high resolution laboratory spectroscopy data are necessary. It is thanks to accurate spectroscopic data that in the last 50 years just few misidentification happened. In order to firmly detect a new molecule in space, prior (or subsequent) laboratory identification is mandatory. Furthermore, precise rest frequencies allow the spatial correlation of different species, which is very important for the consistency of astrochemical models.

1.1.1   Interstellar molecules

CH, CH^+ and CN have been the first molecules observed in space in 1937. The identification happened a little later [4]. It was not understood at that time that the very low rotational temperature inferred from the intensity ratio of the $N = 0$ and $N = 1$ CN lines had indeed a physical meaning. The measured rotational temperature of 2.7 K was in fact due to the cosmic microwave background radiation [5]. The cyanide radical, CN, was acting as a molecular thermometer by measuring the blackbody temperature of the Universe. The study of interstellar molecules has flourished in the 1980s, and it developed in parallel with the millimeter receiver technology. Up to date, around 180 different interstellar molecules have been detected, ranging from simple diatomic to complex organic molecules. The molecules detected in the ISM so far are listed in Table 1.1. One of the most interesting open questions in astrochemistry at the moment is how far the molecular complexity can go in space, and what is the link between the prebiotic molecules detected in space and the life on our planet, and eventually other planets. Molecular spectroscopy and radioastronomy are symbiotic sciences concerning the effort to answer these, and other questions.

TABLE 1.1: Molecules detected in the interstellar medium and circumstellar shells up to July 2013 (CDMS: http://www.astro.uni-koeln.de/cdms/molecules)

Number of atoms	Molecules
2	H_2, AlF, AlCl, C_2, CH, CH^+, CN, CO, CP, SiC, HCl, KCl, NH NO, NS, NaCl, OH, PN, SO, SO^+, SiN, SiO, SiS, CS, HF, HD FeO, O_2, CF^+, SiH, PO, AlO, OH^+, CN^-, SH^+, SH, HCl^+, TiO
3	C_3, C_2H, C_2O, C_2S, CH_2, HCN, HCO, HCO^+, HCS^+, HOC^+, H_2O, H_2S HCN, HNO, MgCN, MgNC, N_2H^+, N_2O, NaCN, OCS, SO_2, c-SiC_2, CO_2, NH_2, H_3^+ SiCN, AlCN, SiNC, HCP, CCP, AlOH, H_2O^+, H_2Cl^+, KCN, FeCN, HO_2, TiO_2
4	c-C_3H, l-C_3H, C_3N, C_3O, C_3S, C_2H_2, NH_3, HCCN, $HCNC^+$, HNCO HNCS, $HOCO^+$, H_2CO, H_2CN, H_2CS, H_3O^+, c-SiC_3, CH_3, C_3N^-, PH_3 HCNO, HOCN, HSCN, H_2O_2, C_3H^+
5	C_5, C_4H, C_4Si, l-C_3H_2, c-C_3H_2, H_2CCN, CH_4, HC_3N, HC_2NC, H_2C_2O H_2NCN, HNC_3, SiH_4, H_2COH^+, C_4H^-, $HC(O)CN$, HNCNH, CH_3O, NH_4^+
6	C_5H, l-H_2C_4, C_2H_4, CH_3CN, CH_3NC, CH_3OH, CH_3SH, HC_3N^+, HC_2CHO, NH_2CHO C_5N, l-HC_4H, l-HC_4N, c-H_2C_3O, H_2CCNH, C_5N^-, HNCHCN
7	C_6H, CH_2CHCN, CH_3C_2H, HC_5N, CH_3CHO, CH_3NH_2, c-C_2H_4O, H_2CCHOH, C_6H^-
8	CH_3C_3N, $HC(O)OCH_3$, CH_3COOH, C_7H, C_6H_2, CH_2OHCHO l-HC_6H, CH_2CHCHO, CH_2CCHCN, H_2NCH_2CN, CH_3CHNH
9	CH_3C_4H, CH_3CH_2CN, $(CH_2)_2O$, CH_3CH_2OH, HC_7N, C_8H, $CH_3C(O)NH_2$, C_8H^-, C_3H_6
10	CH_3C_5N, $(CH_3)_2CO$, $(CH_2OH)_2$, CH_3CH_2CHO
11	HC_9N, CH_3C_6H, C_2H_5OCHO, $CH_3OC(O)CH_3$
12	c-C_6H_6, $C_2H_5OCH_3$, n-C_3H_7CN
more than 12	$HC_{11}N$, C_{60}, C_{70}

1.2   New radio and far-infrared observatories

The upcoming radio and far-infrared observatories will challenge the work of spectroscopists. Laboratory data is urgently needed in order to interpret the astronomical spectra that have been taken with instruments such as HIFI on the Herschel satellite, and that will be taken at new and upcoming observatories such as ALMA, SOFIA and CCAT.

The Atacama Large Millimeter/submillimeter Array (ALMA), see Figure 1.1, is an interferometric array, composed initially of 66 antennas located at 5000 meters altitude on the Chajnantor Plateau, in northern Chile. ALMA provides an unprecedented sensitivity, angular resolution, spectral resolution and imaging fidelity in the frequency range between 84 and 950 GHz. ALMA is a giant array of 12-m antennas, with baselines up to 16 km, and an additional compact array of 7-m and 12-m antennas to image extended targets. Rare isotopologues and vibrationally excited states of known astronomical species, as well as new interstellar molecules will be detected by ALMA in the upcoming years. For the proper identification of these species, laboratory data is necessary.
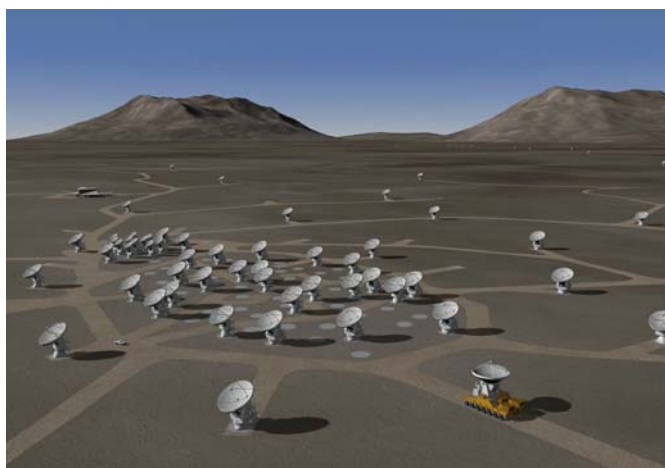
FIGURE 1.1: The Atacama Large Millimeter/submillimeter Array. Credits: www.eso.com

SOFIA, the Stratospheric Observatory For Infrared Astronomy, see Figure 1.2, is the largest airborne observatory in the world, working at far-infrared and submillimeter wavelengths. SOFIA performs observations at wavelengths that are impossible to observe also for the largest and highest ground-based telescopes. A 2.5-meter telescope is housed in a Boeing 747-SP aircraft in order to make sensitive infrared

measurements at an altitude 12.5 km, where the pw, precipitable water vapor level, is less than 7 micron. The telescope has a pointing accuracy better than 1 arcsec. GREAT (German REceiver for Astronomy at TeraHertz frequencies) is an infrared heterodyne spectrometer working in the frequency range of (1.25 - 1.5) THz and (1.82 - 1.92) THz, and allowing a maximum resolution of 47 kHz. This combination of frequency coverage and resolution has never been reached before. GREAT will allow to study, among other, small light molecules that could not be studied before.

FIGURE 1.2: SOFIA, the Stratospheric Observatory For Infrared Astronomy. Credits: www.dlr.de

CCAT will be a 25-meter telescope for astronomy in the submillimeter-wave range, see Figure 1.3. It will be located at 5600 m altitude on Cerro Chajnantor in northern Chile. CCAT will combine high sensitivity, a wide field of view, and a broad wavelength range to provide an unprecedented capability for deep, large-area, multicolor submillimeter surveys. First light for CCAT is planned for 2017. Given its high angular resolution, 3.5 arcsec at 350 micron, CCAT maps will resolve structural features and allow to study processes that are crucial for star formation.
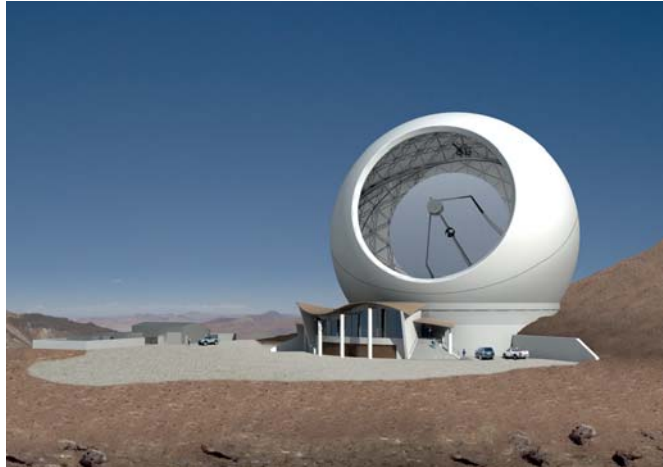
FIGURE 1.3: Concept View of the CCAT on Cerro Chajnantor, Chile. Credits: www.ccatobservatory.org

In the course of this thesis I have performed observations with the IRAM 30 m telescope located at almost 3000 m altitude on Pico Veleta in Sierra Nevada (Spain), see Figure 1.4. It is a sensitive single dish telescope with a 30 m antenna, operating at 3, 2, 1, and 0.9 mm. In particular, for my observations I used the EMIR receiver in the 3 mm band (E090 band) with the Fourier Transform Spectrometer (FTS) backend at high spectral resolution (50 kHz). The total instantaneous bandwidth at a resolution of 50 kHz is 7.2 GHz, while at 200 kHz is 16 GHz.

FIGURE 1.4: The IRAM 30 m telescope, located in Pico Veleta in Sierra Nevada (Spain).

1.3   Necessity of laboratory data

The facilities described in the previous section promise to unveil the physics and chemistry of the interstellar and circumstellar medium. This will only be possible if the molecular databases used by radioastronomers will be fed with high quality new data. The most frequently used databases in the field of radioastronomy are the Cologne Database for Molecular Spectroscopy (CDMS) [6], and the JPL catalog, [7]. These catalogs are both intended to be a guide during the preparation of observations, and a reference for the identification of molecular species. In the CDMS and in the JPL catalog the same programs are used for fitting the spectra and generating the spectral catalog, SPFIT and SPCAT [8] respectively, so the output format is the same. The catalog lists frequencies with calculated uncertainties, intensities (300 K is used as a default temperature, but other temperatures may be requested in the catalog search form of the CDMS), the energies of the lower rotational levels, and the quantum numbers. The catalogs are generated by least-squares fitting of published spectral lines. The wider in frequency the set of measured lines is, the more accurate and reliable will be the generated catalog also at higher frequencies. Frequency accuracies well below the spectral resolution of the instrument are of crucial importance when analyzing an astronomical spectrum. Now that the far-infrared region of the electromagnetic spectrum is accessible, a big effort has to be made by the spectroscopic community in order to provide high quality data also at high frequencies.

Furthermore, with the high sensitivity of new facilities, new molecular species will be detected. Without high resolution spectroscopic studies, these molecular species will not be identified. Molecules with rare isotopes will finally come out of the noise where they were hidden in old surveys. Observations of all the isotopologues, or isomers, of a molecular species are important for astrochemical models in order to understand the path of formation of a molecule, or of a certain class of molecules.

Deuterium enrichment has been proven to be a good indicator of the early stages of star formation. With the upcoming observatories many more deuterated and multiple deuterated species will be observed.

The study of organic molecules such as methanol and dimethylether is also important, as they are widely distributed in space and have a dense spectrum. Sources such as Orion KL, an high-mass star-forming region, have a complicated spectrum to analyze. The spectrum is dominated by the features of complex molecules, such

as methanol. Until the lines of methanol are not all assigned, it will be difficult to identify new species in such a spectrum. The only means to identify all the new features in the upcoming data (isotopologues, excited states, new molecular species) is to have very accurate rest frequencies, and this can only be accomplished with laboratory measurements.

1.4   This thesis

During my PhD thesis I have observed and analyzed spectra of elusive molecules in laboratory and in space.

The theory on which is based the analysis of the molecules object of my study, is introduced in Chapter 2.

I have developed a new discharge cell to produce and study unstable molecules such as molecular ions. The problems and challenges encountered during the development of the new discharge cell, as well as the first results, are described in Chapter 3.

I have also extended the frequency coverage on CO^+. The first THz spectra of this small cation have been measured in this work. All the available data for several isotopologues of CO^+ in the millimeter and submillimeter frequency range have been fitted together for the first time in an isotopically invariant fit. A much more accurate catalog at high frequencies is now available. This part of my work is described in Chapter 4. CO^+ is a good tracer of photon-dissociation regions (PDRs). PDRs are regions around massive young stars, in which far ultraviolet photons strongly influence the gas chemistry. So far CO^+ was detected just in the 2 lowest rotational transitions, and with very low rotational temperatures (around 10 K) compared to the surrounding medium (hundreds of Kelvin). Since few rotational levels have been probed, the processes responsible for its excitation cannot be fully understood. Recently the N = 5 - 4 at 500 GHz transition was detected toward Orion South [9]. This is the first high N detection of CO^+. We have performed observations with the APEX telescope* in order to map CO^+ in this source, and to observe also other transitions to better understand and model the excitation of this small cation.

---

*APEX, the Atacama Pathfinder Experiment, is a 12 m diameter antenna on the high altitude site of Llano Chajnantor in Chile.

Furthermore, I detected a new doubly deuterated molecule in space. c-C_3D_2 was observed toward two starless cores, TMC-1C and L1544, during a dedicated observing run at the IRAM 30 m telescope in the fall of 2012. The details and implications of this detection are discussed in Chapter 5.

In the data collected for the detection of c-C_3D_2, also l-C_3HD has been tentatively detected for the first time with a surprisingly high abundance in TMC-1C. The observed ratio between the fully hydrogenated and the monodeuterated linear C_3H_2 is around 50%. This is much more than the ratio observed for the cyclic isomer, around 10%, or for any other deuterated molecule observed so far. A new proposal has been submitted at the IRAM 30 m telescope in order to confirm this detection. The tentative detection of l-C_3HD is described in Chapter 6.

Chapter 2

Theoretical Considerations

2.1 Introduction

Rotational spectroscopy is an important tool used to study the structure of molecules in the gas phase. Compared to vibrational and electronic spectra, rotational spectra are very selective: spectral superimpositions are very unlikely to occur. Given the high selectivity of rotational spectroscopy, it is often not required to have a purified gaseous sample. This is of particular importance in case of unstable molecules such as ions. High accurate spectroscopic data are used to derive molecular parameters. Once the molecular parameters are derived, it is possible to predict the spectrum of a certain molecular species. During my PhD work I have measured accurate rest frequencies for CO^+ in different isotopic species and vibrationally excited states, and performed an isotopically invariant fit by collecting all the available experimental data (see Chapter 4). In this chapter a brief description of the theoretical background of this analysis is reported. Important detections are described in the radioastronomical part of the thesis, namely the first detection of c-C_3D_2 and the tentative detection of l-C_3HD. Accurate rest frequencies predicted from laboratory measured lines are necessary for a reliable detection of a molecule in space. The spectroscopic work prior to the astronomical observation of c-C_3D_2 and l-C_3HD is summarized in Chapter 5 and 6, the theoretical background necessary to understand the spectra of these molecules is reported in this chapter.

Dunham's approach to study the spectrum of a diatomic molecule will be explained with regard to its application on the study of CO^+. The limit of the use of

Born-Oppenheimer approximation, as well as the consequent necessity to use the so-called Born-Oppenheimer breakdown parameters will be addressed. Given the presence of one unpaired electron, the spectrum of CO^+ possesses a fine structure. The effects on the energy levels of the molecule will be clarified by using one of Hund's coupling schemes. Furthermore $^{13}CO^+$ presents a hyperfine structure, owing to the nuclear spin of ^{13}C. The additional splitting of the energy levels due to the hyperfine structure will be described.

Both cyclic and linear C_3H_2 are asymmetric top rotors, close to the oblate and prolate symmetric top, respectively. The energy level structures and the allowed rotational transitions will be described for both cases.

This chapter is mainly based on the textbooks by Townes & Shawlow [10], Bernath [11], and Gordy & Cook [12].

2.2   Rotational motion of a molecule

The simplest approach to describe a rotating molecule is considering it as a rigid rotor. With this approximation, the distance between the nuclei is assumed to be constant and independent from the rotation of the molecule. The Hamiltonian associated with this simplified description of the molecule is:

$$\hat{H}_{rot} = \frac{\hat{J}^2}{2I} = \frac{\hbar^2 J(J+1)}{2I} \tag{2.1}$$

where $\hat{J}$ is the angular momentum operator, J is the rotational quantum number and I is the moment of inertia. The energy of a rotational level for a diatomic molecule is

$$E_J = BJ(J+1) \tag{2.2}$$

The units of (2.2) depend on the units chosen for B. B is the rotational constant and it is defined as

$$B = \frac{\hbar}{4\pi I} \times 10^{-6}[\text{MHz}] \qquad (2.3)$$

The spectrum described in such an approach consists of a series of equidistant lines, separated by $2B$. Assuming that the distance between the two nuclei does not change as the molecule rotates is, of course, a very rough approximation. Due to centrifugal distortion effects the distance (i.e the bond length) changes, and as a consequence the lines composing the spectrum will not be equidistant. The spacing in fact will decrease as J increases. In order to take this effect into account, higher order terms have to be included when describing the energy associated to the rotational level :

$$E_J = BJ(J+1) - DJ^2(J+1)^2 + HJ^3(J+1)^3 + ... \qquad (2.4)$$

Figure 2.1 showns the scheme of rotational levels for a diatomic molecule.
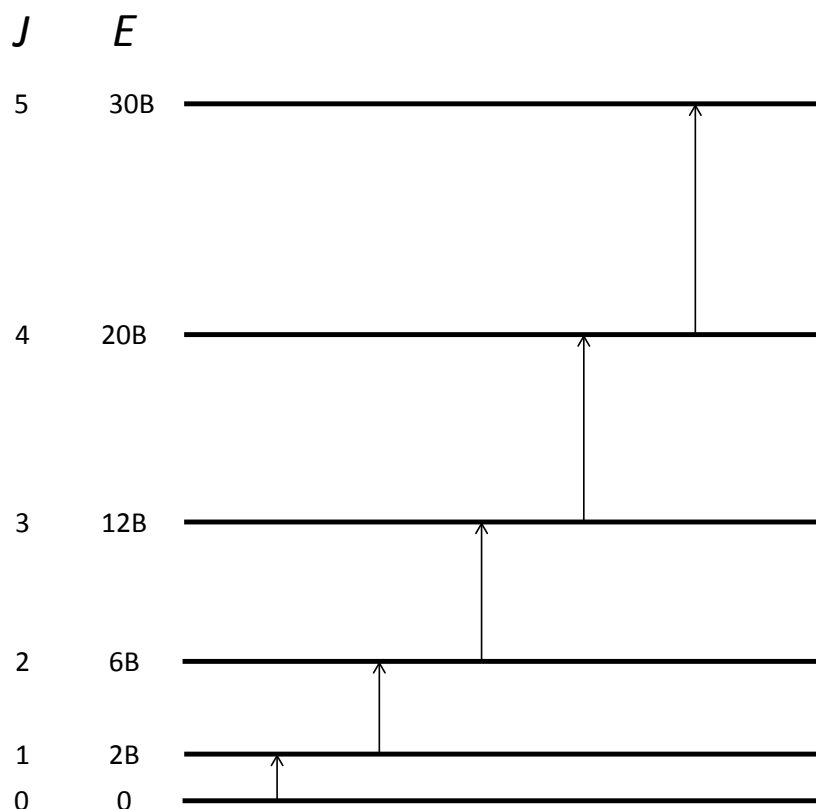
FIGURE 2.1: Scheme of the rotational energy levels for a diatomic molecule described as a rigid rotor. The arrows indicate the rotational transitions.

2.3   Diatomic molecules - CO^+

The description of a diatomic molecule is simplified by the fact that it can be treated as a distorted vibrating rotor. Its potential is a function of the bond length, and just the stretching vibrational mode occurs. In this work high resolution spectroscopy of CO^+ has been performed. An isotopically invariant fit has been used to analyze the whole experimental dataset available for most of the isotopologues of CO^+ (see Chapter 4). The theoretical model used was studied by Dunham [13] in 1932, and it will be described in the following subsection.

2.3.1   Dunham's solution

The approach introduced by Dunham [13] to describe the potential of a diatomic uses the Born-Oppenheimer approximation [14]. According to the Born-Oppenheimer approximation, it is possible to separate the electronic and nuclear wave functions assuming that the electrons instantaneously follow the motion of the nuclei, given the big difference in their respective masses. The electronic potential is assumed to be independent of the masses of the nuclei and their motion, so it is the same for every isotopologue. Therefore, within this approximation the equilibrium bond lengths do not change in different isotopic species of a given diatomic molecule.

The Dunham approach works well far from the dissociation. In the case of a very deep potential, the Dunham formalism can be employed to rather high v and J, whereas it may fail for a very flat potential.

Dunham describes the potential function $U(\xi)$ as a series expansion:

$$U(\xi) = a_0\xi^2(1 + a_1\xi + a_2\xi^2 + a_3\xi^3 + ..) + B_e J(J+1)(1 - 2\xi + 3\xi^2 - 4\xi^3 + ..) \quad (2.5)$$

with $\xi = \dfrac{r - r_e}{r_e}$ and a_0, a_1, etc. being potential constants.

The energy of the levels is expressed as follows:

$$\frac{E_{v,J}}{h} = \sum_{l,m} Y_{l,m}(v + \frac{1}{2})^l J^m (J+1)^m \quad (2.6)$$

$Y_{l,m}$ are the so-called Dunham's constants. They can be considered as equivalent to the constants more familiar to a spectroscopist:

$$Y_{0,1} \simeq B_e \qquad Y_{1,2} \simeq -\beta_e$$
$$Y_{0,2} \simeq -D_e \qquad Y_{2,1} \simeq \gamma_e$$
$$Y_{0,3} \simeq H_e \qquad Y_{1,0} \simeq \omega_e$$
$$Y_{1,1} \simeq -\alpha_e \qquad Y_{2,0} \simeq -\omega_e x_e$$

Dunham's parameters $Y_{l,m}$ depend on the masses of the two nuclei composing the diatomic, A and B

$$Y_{l,m} \propto \mu^{-(\frac{l}{2}+m)} \tag{2.7}$$

where μ is the reduced mass $\dfrac{M_A M_B}{M_A + M_B}$. In case of an ion, like CO^+, the charge has to be taken into account, and the reduced mass has to be modified as following:

$$\mu = \frac{M_A M_B}{M_A + M_B - C m_e} \tag{2.8}$$

with C being the charge number and m_e the mass of the electron. Dunham's parameters $Y_{l,m}$ therefore cannot be considered isotopically invariant. It is possible to define a set of isotopically invarant parameters, $U_{l,m}$, in the following way:

$$U_{l,m} = \frac{Y_{l,m}}{\mu^{-(\frac{l}{2}+m)}} \tag{2.9}$$

The Born-Oppenheimer approximation is normally a good framework for the analysis of spectra of diatomics, it introduces, in fact, a very small error. Nevertheless, high resolution spectroscopic data of several isotopic species of a diatomic can give information on the limitations of this approximation, for example when analyzing the spectra as it was done in this work for CO^+ (see Chapter 4). The expression (2.9) can be modified by introducing the so-called Born-Oppenheimer breakdown parameters $\Delta_{l,m}$. Watson [15] studied the isotopic dependence of the Dunham coefficients, and derived the following way to express those coefficients in terms of mass-independent parameters $U_{l,m}$ and corrections $\Delta_{l,m}$ to the Born-Oppenheimer approximation

$$Y_{l,m} = U_{l,m}\left(1 + \frac{m_e \Delta_{l,m}^A}{M_A} + \frac{m_e \Delta_{l,m}^B}{M_B}\right)\mu^{-(\frac{l}{2}+m)} \tag{2.10}$$

where $U_{l,m}$ is an isotopic invariant coefficient, m_e is the electron mass, M_A and M_B are the atomic masses, μ is the charge modified reduced mass introduced by Watson, and $\Delta_{l,m}$ are the Born-Oppenheimer breakdown correction terms.

2.3.2   Spectra of radicals and ions

The electronic ground state for CO^+ is $^2\Sigma^+$. CO^+ possesses an electronic spin of $\frac{1}{2}$, and the coupling of the spin with the overall rotation of the molecules has to be taken into account. Radicals, such as CO^+, are classified as follows:

$$^{2S+1}\Lambda^{(+/-)} \tag{2.11}$$

$(2S+1)$ is the electron multiplicity, where S is the total electron spin, Λ is the total electronic angular momentum, and $(+/-)$ indicates th reflection through a plane containing the internuclear axis ($+$ = symmetric, $-$ = antisymmetric). CO^+, for example, has an electronic angular momentum along the molecular axis equal to zero ($\Lambda = 0$), so it is denoted as a Σ state. As its electronic spin, S, is equal to $\frac{1}{2}$, CO^+ is a doublet, hence $^2\Sigma^+$. Hund has described 5 different possibilities for the coupling of the electron spin, and eventually the electronic angular momentum, with the overall rotation of the molecule. Hereafter I will briefly describe just the Hund's b case, as it is the best suited for CO^+. The description of the other coupling possibilities can be found in the book Gordy & Cook [12].

2.3.3   Hund's case b for $^2\Sigma$ molecules, the fine structure of CO^+

The fine structure in a molecular spectrum can arise from the following interactions: electronic spin-rotation, spin-orbit, and spin-spin coupling. Molecules with one unpaired electron, such as CO^+, present electron spin-rotation fine structure. The spin-orbit fine structure arises in molecules with non-zero electronic orbital angular momentum, while the spin-spin fine structure emerges when the molecule has more than one unpaired electron. The only fine structure present in the CO^+ spectrum is due to the electron spin-rotation interaction. The electronic spin is coupled to the rotational axis through the interaction of the spin magnetic mo-

ment with the weak magnetic field generated by the rotation of the molecule. The Hamiltonian for $^2\Sigma$ rotating molecules is

$$\hat{H} = B_v \hat{N}^2 - D_v \hat{N}^4 + \gamma_v \hat{S} \hat{N} \tag{2.12}$$

where $\hat{N}$ is the rotation operator, $\hat{S}$ is the electronic spin operator, B_v is the rotational constant, D_v is the centrifugal distortion constant, and γ_v is the spin rotation coupling constant (all for the vibrational state v). A vector diagram of this coupling is shown in Figure 2.2. The angular momentum J is then defined as

$$\hat{J}^2 = \hat{N}^2 + \hat{S}^2 - 2\hat{S}\hat{N} \tag{2.13}$$

As it is shown in Figure 2.3, the rotational levels for a molecule in a $^2\Sigma$ state are split into doublets by the spin rotation interaction. The lowest level corresponds to $J = \frac{1}{2}$.

The selection rules for rotational transitions are:
$\Delta N = \pm 1$ and $\Delta J = 0, \pm 1$
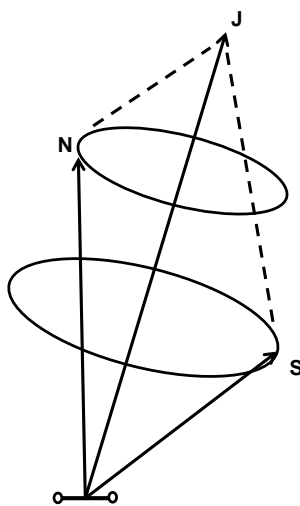
FIGURE 2.2: Scheme of the Hund's case b coupling for molecules like CO^+ in a $^2\Sigma$ electronic ground state.
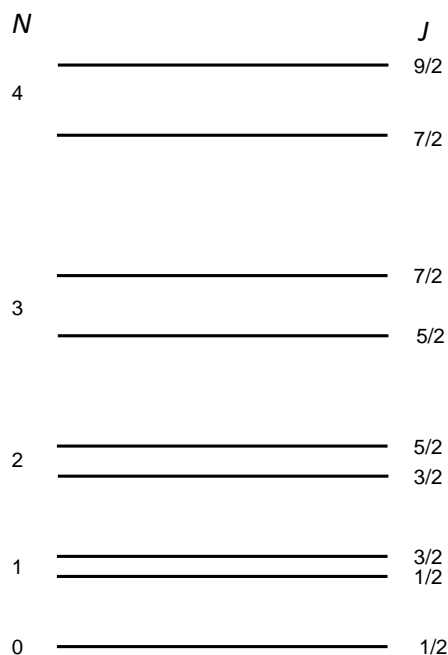
FIGURE 2.3: Energy level diagram for the rotational level of a diatomic molecule in a $^2\Sigma$ electronic ground state.

2.3.4   The hyperfine structure of CO$^+$

Molecules with at least one atom that possesses a non-zero nuclear spin exhibit hyperfine structure. The hyperfine splitting is often very small, normally smaller than the fine splitting. In the case of the set of isotopologues of CO$^+$ studied in this work, ^{13}CO$^+$ is the only one that has an hyperfine structure since ^{13}C has a nuclear spin of $-\frac{1}{2}$. Several types of interaction can produce hyperfine structures. In the case of ^{13}CO$^+$ it arises from the interaction of the electronic spin with the nuclear spin. The two constants to account for this interaction are b_F and c, see Chapter 4, which are the isotropic and anisotropic parts of the electron-spin nuclear-spin interaction. In Figure 2.4 the hyperfine splitting of the $N = 2$ rotational level of ^{13}CO$^+$ is presented as an example.
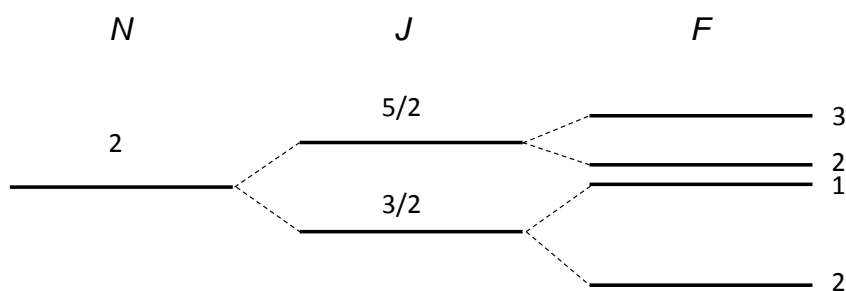
FIGURE 2.4: Hyperfine splitting of the $N = 2$ level of $^{13}CO^+$.

2.4 Asymmetric tops - cyclic and linear C_3H_2

In an asymmetric top molecule the moments of inertia along the three principal axes are different, i.e. $I_A \neq I_B \neq I_C$. The Schrödinger equation for the asymmetric top has no analytical solution, it has to be solved numerically. The two isomers of C_3H_2, cyclic and linear, studied in this work (Chapter 5 and 6) are both asymmetric tops. The "Ray asymmetry parameter" κ is a measure of the asymmetry of a molecule, and it is defined as:

$$\kappa = \frac{2B - A - C}{A - C} \tag{2.14}$$

where A, B and C are the rotational constants of the molecule. The values of κ are in the range from -1 for a prolate symmetric top, to $+1$ for an oblate symmetric top. Being $\kappa = +0.69$ for c-C_3H_2 and $\kappa = -0.99$ for l-C_3H_2, the cyclic C_3H_2 can be considered as an oblate asymmetric top, while the linear C_3H_2 is a prolate asymmetric top. The labeling of the energy levels of an asymmetric top is usually $J_{K_aK_c}$, with J being the rotational quantum number and K_a and K_c the quantum numbers of the prolate and oblate symmetric top energy levels. Figure 2.5 shows the energy levels for the case of an oblate and a prolate symmetric top, while in Figure 2.6 the prolate-oblate correlation is presented.

Prolate symmetric top   Oblate symmetric top
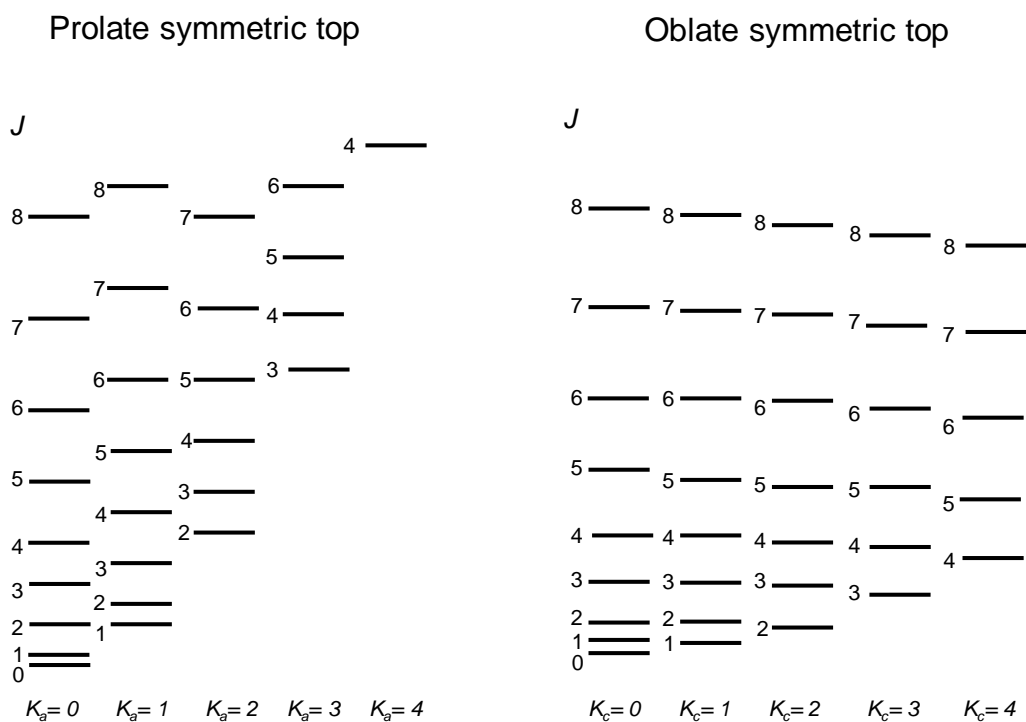
FIGURE 2.5: Energy levels of a prolate and oblate symmetric top.
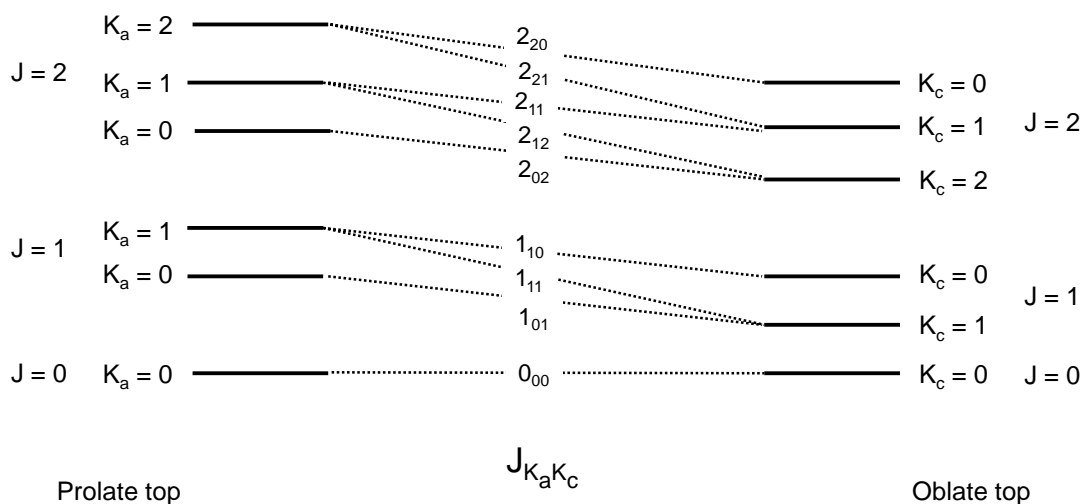
FIGURE 2.6: Labeling of the asymmetric top energy levels: prolate-oblate correlation diagram.

Compared to a symmetric top, there are more allowed transitions for an asymmetric top. The selection rules for an asymmetric rotor are $\Delta J = 0, +1, -1$. They

originate Q, R and P transitions, respectively. The selection rules for the quantum numbers K_a and K_c depend on the non-vanishing dipole moment components along the three principal axes, namely μ_a, μ_b and μ_c :

a-type transitions	b-type transitions	c-type transitions
$\mu_a \neq 0$	$\mu_b \neq 0$	$\mu_c \neq 0$
$\Delta K_a = 0 \, (\pm 2, ..)$	$\Delta K_a = \pm 1 \, (\pm 3, ..)$	$\Delta K_a = \pm 1 \, (\pm 3, ..)$
$\Delta K_c = \pm 1 \, (\pm 3, ..)$	$\Delta K_c = \pm 1 \, (\pm 3, ..)$	$\Delta K_c = 0 \, (\pm 2, ..)$

When the dipole moment has non-vanishing components with respect to each of the three principal axes, all the transitions listed above are allowed. The most intense transitions are the ones related to the largest components of the dipole moment. Furthermore, the ones corresponding to smaller ΔK are stronger. In Figure 2.7 are shown the three types of transition.
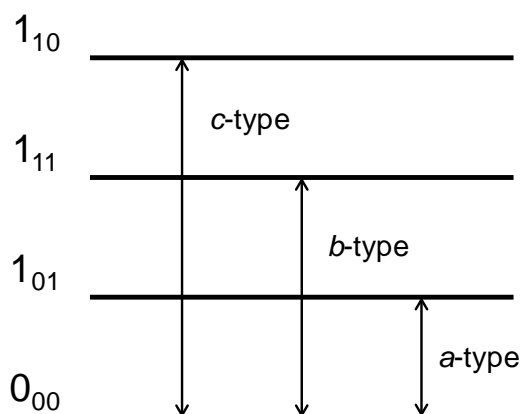
FIGURE 2.7: A sketch of the a-, b- and c-type rotational transitions in asymmetric tops.

2.4.1 Nuclear spin statistics : *ortho* and *para* states in C_3H_2 and C_3D_2

When a molecule possesses two identical nuclei, like C_3H_2 and C_3D_2, the nuclear spin statistic has an effect on the population of the molecular states and therefore also on the intensity of the transitions. As a consequence of the Pauli exclusion principle, for bosons (integer nuclear spin, such as deuterium) or fermions (half-integer nuclear spin, such as hydrogen) the total wave function must be

either symmetric or antisymmetric when the coordinates of two identical nuclei are interchanged, respectively. The effects on the spectra of C_3H_2 and C_3D_2 will be the presence of ortho and para states with peculiar intensity ratios. For C_3H_2 the symmetric levels ($J_{K_aK_c}$ with K_a and K_c both even or both odd) will have a statistical weight of 1, while asymmetric levels ($J_{K_aK_c}$ with K_a and K_c of different parity) will have a statistical weight of 3. For C_3D_2, instead, the symmetric levels ($J_{K_aK_c}$ with K_a and K_c both even or both odd) will have a statistical weight of 6, while asymmetric levels ($J_{K_aK_c}$ with K_a and K_c of different parity) will have a statistical weight of 3. States with higher spin degeneracy are called *ortho*, while states with lower spin degeneracy are called *para*. The *ortho/para* intensity ratio is defined as $\dfrac{I+1}{I}$, where I is the nuclear spin. As hydrogen has a nuclear spin spin of $\frac{1}{2}$, the *ortho/para* intensity ratio for C_3H_2 will be 3. Deuterium, instead, has a nuclear spin of 1, so the *ortho/para* intensity ratio for C_3D_2 will be 2. These characteristics are summarized in Table 2.1.

TABLE 2.1: Spin statistics in C_3H_2 and C_3D_2

	Symm. Level	**Stat. Weight**	**Symm. Level**	**Stat. Weight**
[c-C_3H_2]	ee,oo (*para*)	1	eo,oe (*ortho*)	3
[c-C_3D_2]	ee,oo (*ortho*)	6	eo,oe (*para*)	3

The ortho-para intensity alternation is a powerful tool because it possesses unique informations on the molecular species, and sometimes it acts as a fingerprint. c-C_3H_2, for example, is produced in the laboratory in a discharge of acetylene. When discharging acetylene, many molecular species are formed. The intensity alternation of the ortho and para transitions has been used as a tool to assign for the first time the transitions of c-C_3H_2 in the millimeter-wave region [16].

Chapter 3

Experimental Setup

3.1 Introduction

In this work I have performed absorption spectroscopy of molecular ions in a DC electrical discharge. The experimental setup that I have used is composed by radiation source, absorption cell, and broadband detector. The main feature of my experiment is the discharge cell. Since molecular ions are elusive species that need to be produced in situ, the whole experiment is focused on the production of the ions. The radiation sources, the discharge cells, and the detector that I have used in the course of my PhD work will be described in this chapter.

3.2 Radiation sources

During my PhD thesis I have used two different kinds of radiation sources: in the range of 200-400 GHz, a frequency stabilized backward wave oscillator (BWO[*], Figure 3.1), and in the range of 1.1-1.3 THz a VDI[†] multiplier chain. Figure 3.2 shows a sketch of the experimental setup, while using the BWO. An electron beam is produced by the cathode and accelerated by high voltage, ranging from 1 to 6 kV. The beam is then passing through a periodic slow-wave structure where it is de- and accelerated so that it emits a coherent radiation in the opposite direction of its trajectory. The electrons are focused by a strong magnetic field generated

---

[*]ISTOK RPC, Fryazino, Russia
[†]Virginia Diodes, Inc.

by an electromagnet. Depending on the voltage applied, i.e. the acceleration of the electron beam, a different output frequency is generated. The BWO has to be frequency stabilized, otherwise frequency fluctuations would be in the order of several MHz per minute. This is much more than the desired precision of the spectrometer. The phase stabilization of the BWO is realized in the following way: a small part of the output radiation, around 10%, is coupled through a beam splitter into a harmonic mixer device, where it is mixed with the output of a commercial frequency synthesizer (Rohde&Schwarz [‡]). The harmonic mixer generates harmonics (IF) of the two input frequencies in the following way

$$\nu_{IF} = \pm m \times \nu_{BWO} \pm n \times \nu_{synth} \tag{3.1}$$

To stabilize the BWO, n and ν_{synth} are chosen in a way to obtain a ν_{IF} of 350 MHz for the desired BWO frequency, with $m = 1$. The IF signal is then compared to the reference signal from a rubidium atomic clock ($\Delta\nu \ / \ \nu = 10^{-11}$). Any change of phase is converted by the phase lock loop circuit (PLL) into a voltage and applied to the BWO. By using this stabilization method, the BWO reaches a frequency accuracy $\Delta\nu \ / \ \nu$ better than 10^{-6}. Around 300 GHz the BWO provides usually an output power of 2-5 mW.

At 1.1-1.3 THz, the radiation is generated by a commercial multiplier chain (Virginia Diodes, Inc.) which generates the 72nd harmonic of a synthesizer signal. Usually the output power is around 2 μW.

[‡]Rohde&Schwarz SMF 100 A
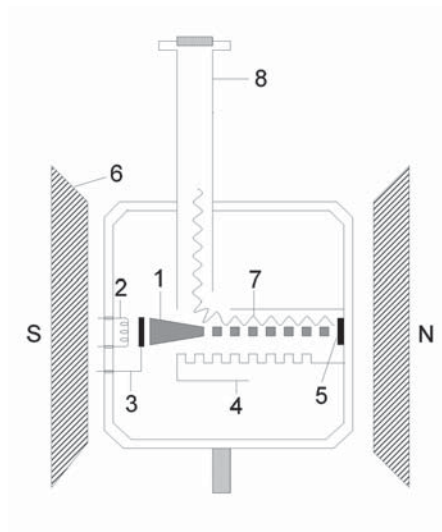
FIGURE 3.1: Schematic view of the backward wave oscillator (BWO). Electron beam (1), filament (2), cathode (3), slow wave structure (4), anode (5), magnet (6), electromagnetic radiation (7), exit (8). [17]
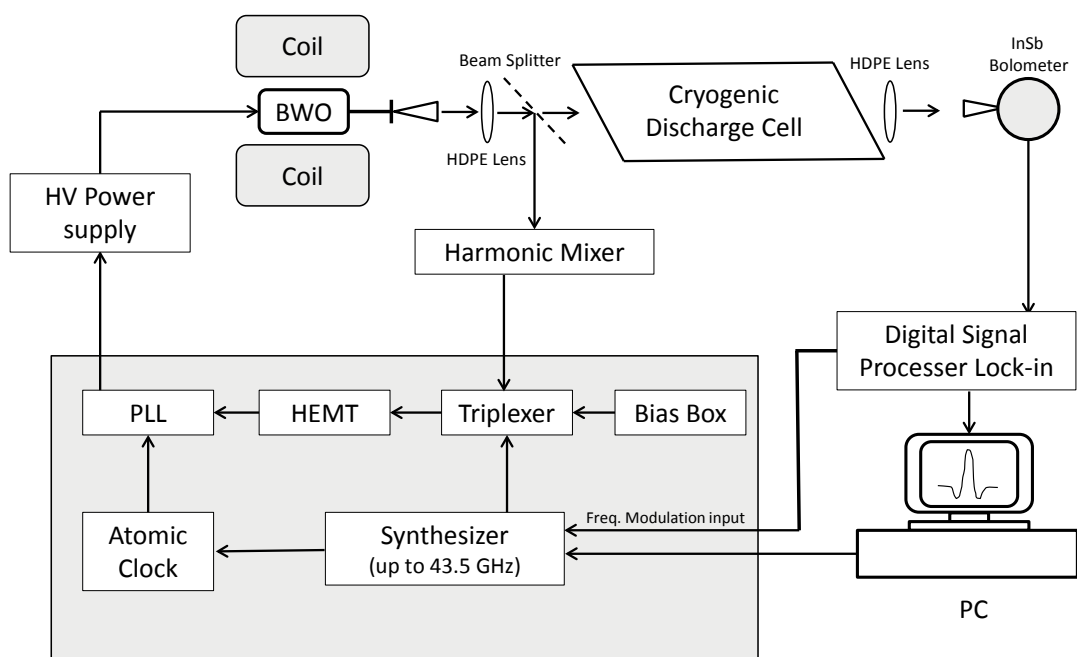
FIGURE 3.2: Scheme of the spectrometer, with the backward wave oscillator as radiation source.

3.3   Detector

A broadband helium cooled InSb Hot Electron Bolometer[§] has been used to record the spectra for this work. Once the incident radiation is absorbed by the InSb, the change of temperature is resulting in a change in the resistance. The very short relaxation time, around 1μs, allows a frequency modulation of the radiation source up to 50 kHz. The operating temperature of the InSb bolometer is 4.2 K, and it is reached with liquid helium. The 4.2 K stage is protected from thermal radiation by a helium gas cooled shield (around 20 K) and a liquid nitrogen cooled shield (77 K). High vacuum (10^{-6} - 10^{-7} mbar) is also needed for thermal insulation of the system.

3.4   High Resolution Spectroscopy of Molecular Ions

Unstable molecules, such as ions and radicals, are very difficult to produce and probe in the laboratory. The development of high resolution spectroscopy of molecular ions is tightly bound to the developments in the field of radioastronomy. During a search for hydrogen cyanide in 1970, Buhl and Snyder [18] detected a line with "unknown extraterrestrial origin" at 89 GHz with the 36-foot telescope of the National Radio Astronomy Observatory in Tucson, Arizona. William Klemperer proposed HCO^+ to be the carrier of this line [19], but the detection was not definitive until the first laboratory detection of HCO^+ in a DC discharge [20]. Other examples of molecules detected first in the Interstellar Medium and subsequently in the laboratory are N_2H^+, HCS^+ and HCO_2^+. The importance of ions in interstellar chemistry has been recognized very soon, Herbst and Klemperer proposed it in 1973 [21]. Since ion-neutral reactions often do not have activation energy barriers, they play a very important role especially in cold regions despite the low fractional ionization. A great impulse to the field has been given by Takeshi Oka with the detection of H_3^+ in the laboratory [22], and its interstellar detection later on [23]. H_3^+ initiates the chain reactions that produce most of the molecular

---

[§]QMC, Cardiff, UK

complexity observed in space so far, see Figure 3.3. The reactions that lead to the formation of H_3^+ in space are the following:

$$H_2 + h\nu \rightarrow H_2^+ + e^-$$
$$H_2^+ + H_2 \rightarrow H_3^+ + H$$
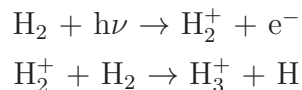
Molecular hydrogen is the most abundant molecule in space, and it is ionized by cosmic rays, which remove an electron and form H_2^+. H_2^+ reacts immediately (within one day in interstellar time scales) with molecular hydrogen to form the H_3^+ ion. As H_3^+ does not react with H_2, it becomes abundant. It took quite a number of years until H_3^+ was finally detected in space. As it does not have any dipole moment and consequently any rotational spectrum, Prof. Oka had to wait until the infrared technology was sensitive enough in order to detect H_3^+ in space [24]. Another important discovery in the field was the first detection of a molecular anion by McCarthy and coworkers in 2006 [25]. Prior to this discovery molecular anions were postulated to exist in the interstellar medium [26], but no high resolution laboratory data was available to conduct a proper search, excluding OH^- and SH^-. Up to date the following six molecular anions have been positively detected in space: C_4H^-, C_6H^-, C_8H^-, CN^-, C_3N^-, C_5N^- [25, 27–31].
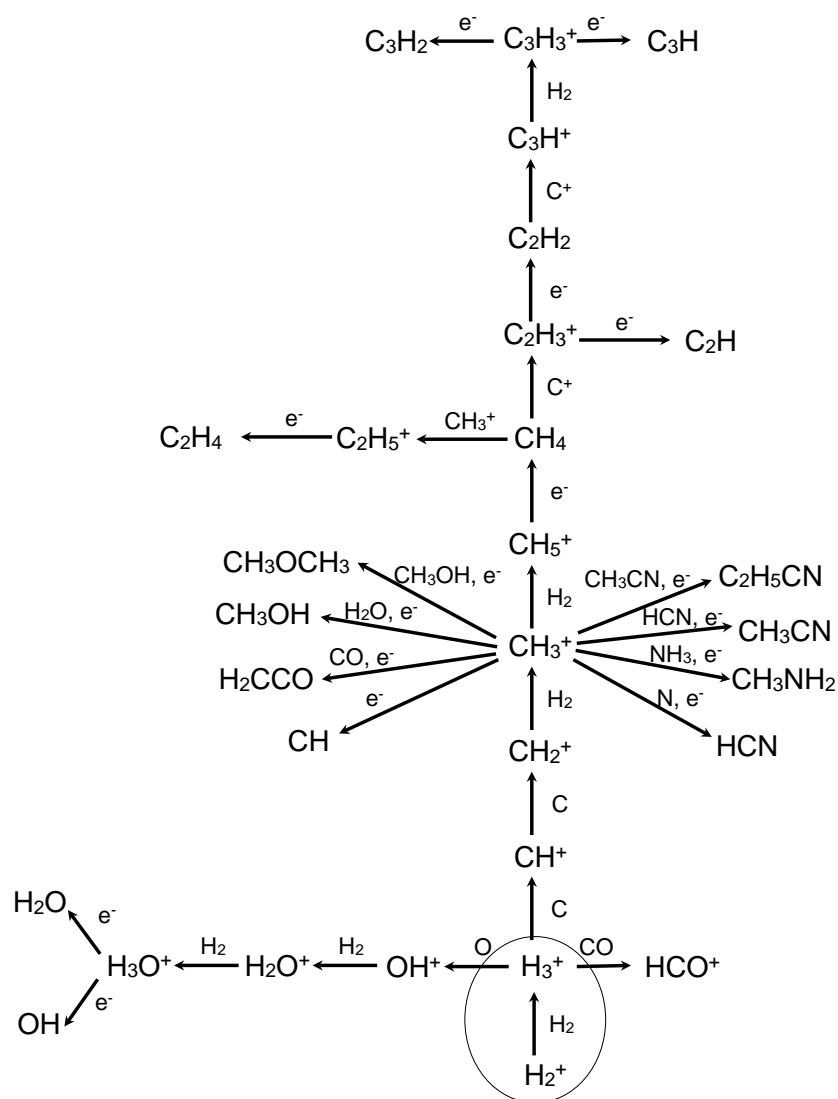
FIGURE 3.3: Interstellar ion-neutral reactions initiated by the formation of H_3^+

3.5   Overview of different techniques

Spectroscopy of molecular ions is difficult because of the very low concentrations that can be produced in low pressure plasmas. The ratio of the ion with respect to the neutral precursor is generally in the range of 10^{-5}-10^{-6}. During the years, the production of molecular ions in DC discharges has been implemented in many ways. The characteristics of the glow discharge depend on several parameters such as the carrier gas, its pressure and the type of electrodes that are used [32]. The plasma in the discharge is not homogeneous. The discharge can be divided

in several regions with different characteristics. Starting from the cathode, the discharge consists of the Aston dark space, the cathodic glow, the cathodic dark space, the negative glow, the Faraday dark space, the positive column, the anodic glow, and the anode dark space, see Figure 3.4. Ions are produced in the so-called "positive column" and "negative glow". The positive column is a region where the electric field is moderate and uniform, which induces a Doppler shift in the absorption frequencies of the ions. This shift is not present in neutrals or radicals, so it is a way of discriminating the lines belonging to the ions from the lines belonging to other carriers. Despite the low electron density, the majority of the ions are produced in the positive column under normal conditions, as it occupies the largest part of the cell. The negative glow is the brightest region of the discharge, and it is located close to the cathode. Here the electric field is weak and the Doppler shift is negligible. Usually the negative glow is much smaller than the positive column, but the ionic density is one order of magnitude higher. The variation of the electric field, charge and current densities along the length of the discharge are shown in Figure 3.5.

The temperature plays a crucial role in the production of molecular ions. Low temperatures, from 77 to 150 K usually, are needed. The low temperature is important given the very low concentration of ions that can be produced in the discharge, as it increases the absorption coefficients. It also lowers the amount of undesired molecules present in the cell. Water, for example, will freeze on the cell walls. One of the most important destruction paths for the ions is the collision with the cell walls. Low temperature helps to minimize these collisions by slowing down the ions.
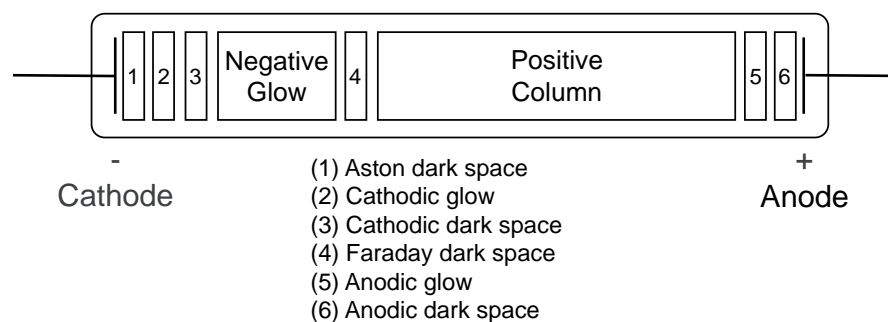
FIGURE 3.4: Different regions that compose the DC glow discharge: the ions are produced in the negative glow and in the positive column.
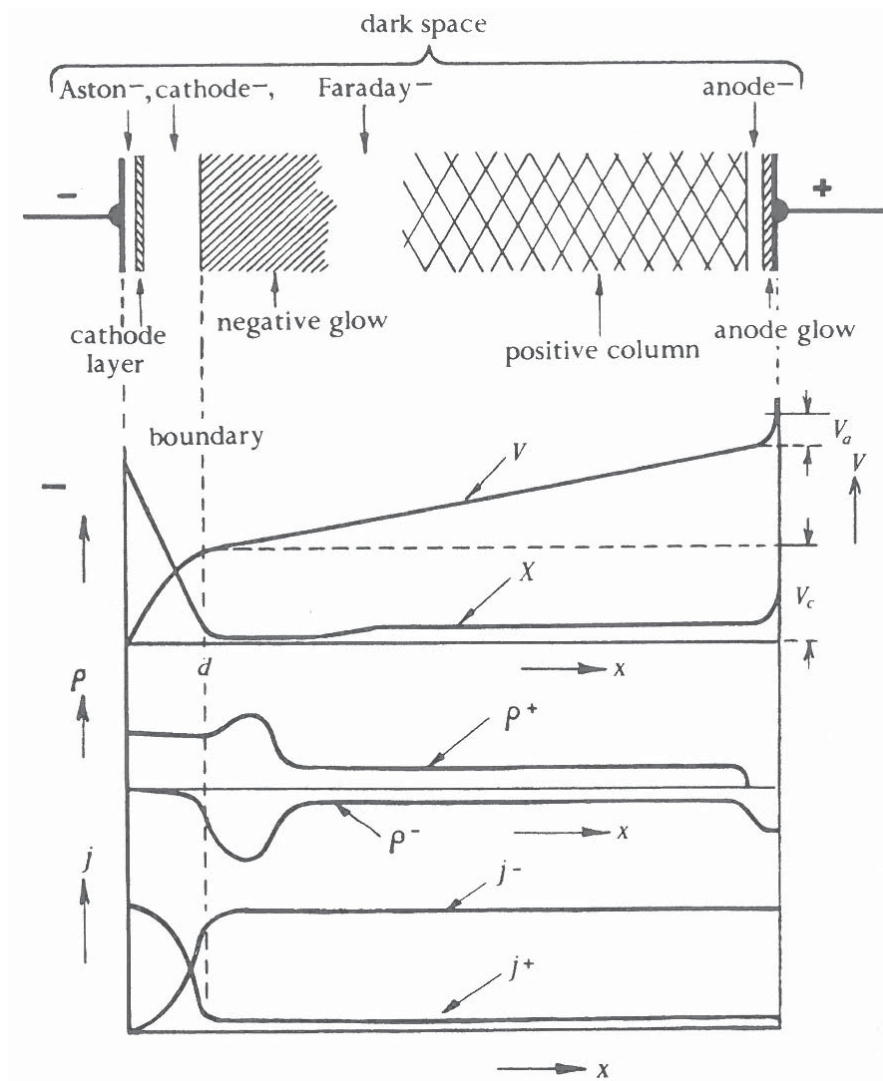
FIGURE 3.5: Schematic spatial distribution of electric field X, space-charge density ρ^+ and ρ^-, and current densities j^+ and j^- in a glow discharge [32].

3.5.1   Hollow cathode

The hollow cathode DC discharge uses a long cathode, and a shorter anode. The advantage is the elongation of the negative glow region of the discharge [33, 34]. An ion-rich, field-free negative glow is then created over the entire length of the cathode. The electrons form an axial beam that enhances the density of ions in the cell.

3.5.2 Extended negative glow

This method also aims at extending the length of the negative glow in the cell by using a magnetic field [35, 36]. An external magnetic field is used to confine the electrons and the ions in the center of the cell and to limit the diffusion to the walls. Normally the magnetic fields applied are in the order of 200 Gauss.

3.5.3 Velocity modulation

Saykally and co-workers have developed a very elegant method to detect complex ions, whose lines normally would be "hidden" by the much stronger lines of their precursors [37, 38] (more abundant by a factor of 10^5-10^6). The mobility of the ions in the plasma is the basis of this method: by applying an AC discharge, the Doppler shift modulates the line position. This method also discriminates between positive and negative ions.

3.6 Old experiment

The discharge cell that I have used for the laboratory work discussed in Chapter 4 is shown in Figure 3.6. The cell is composed of two glass cells, one inside the other. The cell's inner diameter is 5 cm and harbors two electrodes made of stainless-steel sheets. Around the cell there is a copper solenoid coil used for cooling and eventually generating a magnetic field by applying a current. In order not to provoke stress and eventually break the inner cell, the copper coil is not directly in contact with the glass. There is a thin layer of silicon glue acting as a thermal contact between the copper coil and the cell. The silicon glue is not specified for cryo-temperatures, so it breaks and falls apart gradually by cooling it. The signal to noise of the ions' lines become worse until the lines completely vanish with decreasing thermal contact since the lifetime of the ions is strictly connected to the temperature. It was necessary to open and re-glue the coil to the cell every one to two months, depending on use. The reliability of the results was compromised by the continuous degradation of the ions' signal. The outer cell is evacuated in order to minimize the heating of the inner cell due to conduction. All the connections are on the same side of the cell for safety reasons, because on the opposite side is placed the high voltage connection. As you can see in Figure 3.7, the inlet and

outlet of the gas in the inner cell, as well as the connection to pump the outer cell, are placed on the same window. Another weak point of this cell is that all the connections are passing through the side of the window. This limits the flow in the cell as the pumping goes through a very small cross section ($\sim$1 cm^2). The connections passing through the sides of the window gives also rise to problems with the vacuum, since it is not possible to make them perfectly vacuum tight. In order to improve the ion production, we designed a new discharge cell where we focused on the following aspects:

- Temperature control

- Flow control

- Better vacuum

- Reliability

- More easy to handle, disassemble and change parts
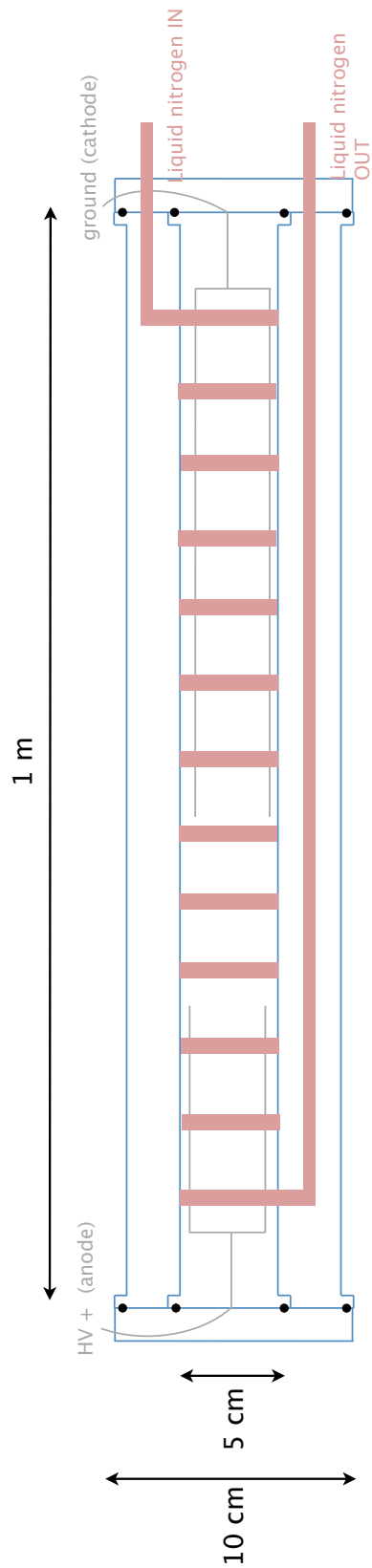
FIGURE 3.6: Old discharge cell used for the laboratory work described in Chapter 4. It is composed by two glass cells, one inside the other. The inner cell contains the electrodes and is surrounded by a copper solenoid used for cooling.
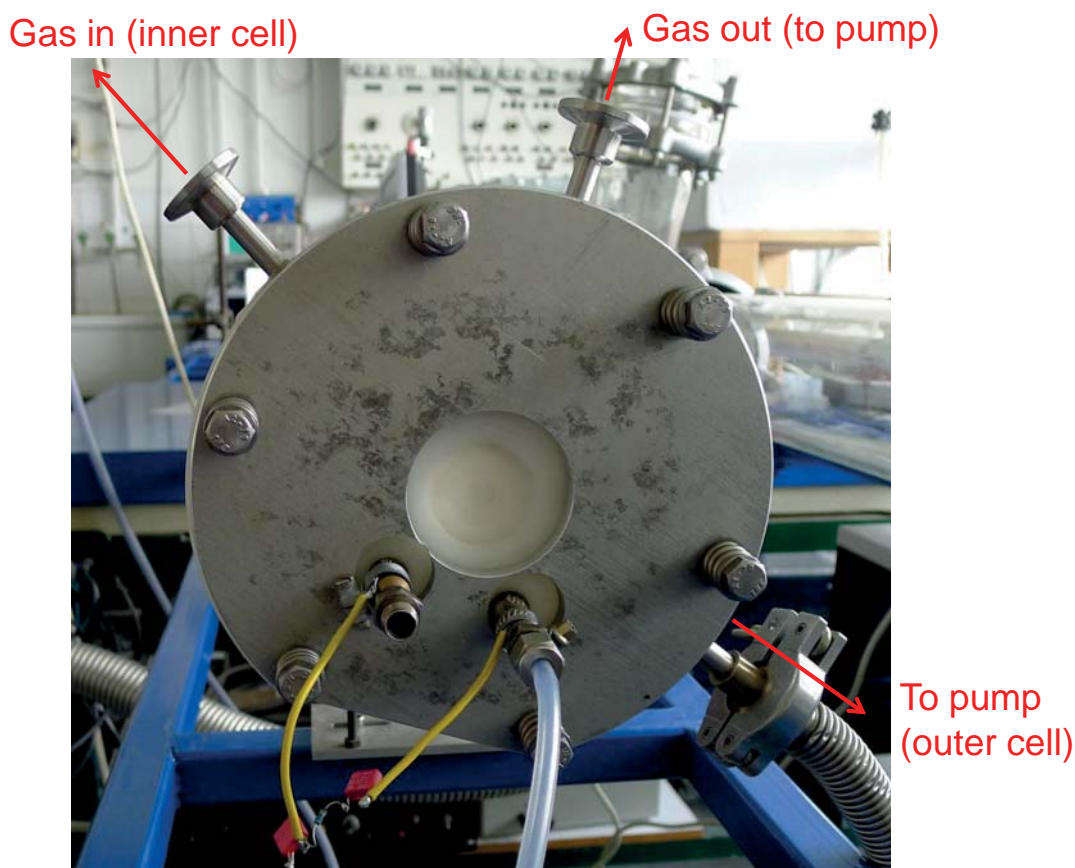
FIGURE 3.7: Side view of the old discharge cell. All the connections from the outside to the inside of the cell pass through the side of the window (pumps and precursor gases).

3.7   Development of the new discharge cell

The new discharge cell can be seen in Figure 3.8. The two main requirements for the new discharge cell are the control of the temperature and the control of the flow in order to be able to control better the performances of the cell, and finally produce more ions. To control the temperature now a jacketed cell is used. Figure 3.9 shows a prototype of this cell. The liquid nitrogen, or any other cooling agent, passes through the jacketed cell, and is in direct contact with the inner cell, where the electrodes are, leading to an improved thermal contact. Figure 3.10 shows the electrodes inside the cell. Another improvement concerns the usage of the liquid nitrogen. In the old cell the liquid nitrogen was continuously pumped inside the cell from a vacuum insulated container. Hence, a lot of liquid nitrogen was wasted. In the new cell a so-called "chicken feeder" is used. The liquid

nitrogen is stored in a box on top of the cell, and it continuously drops into the cooling jacket of the cell. The advantage of using the chicken feeder is that there is no waste of liquid nitrogen, as the system is self regulating and consumes just the necessary amount of it. The glass cell was manufactured by the glass blower at the Chemistry Department of the University of Cologne. First we tried to manufacture a glass cell with three layers. The idea was to evacuate the external layer and insulate the cooling layer from the ambient. Unfortunately this cell broke during the cooling tests with liquid nitrogen. The stress that the glass cell has to sustain in a liquid nitrogen cooled discharge experiment, is high. The cell is evacuated, cooled to 77 Kelvin, and the discharge heats the cell with a power usually ranging from 40 to 80 Watts. As the three-layers tentative failed, a cell with two layers has been finally manufactured. The length of the cell is 1.3 m. The length has been chosen so that the cell could fit into an oven and could be tempered, for strengthening purposes. To minimize the thermal stress onto the cell, I wrapped around it several layers of air filled foam as insulating material (see the white wrap around the cell in Figure 3.8).

To control the flow, a four-way cross piece has been placed at the end of the cell. Now the cell is pumped through a cross section of ~ 20 cm^2, while the old discharge cell was pumped through a cross section of ~ 1 cm^2. The flow is 40 times larger than in the old cell.
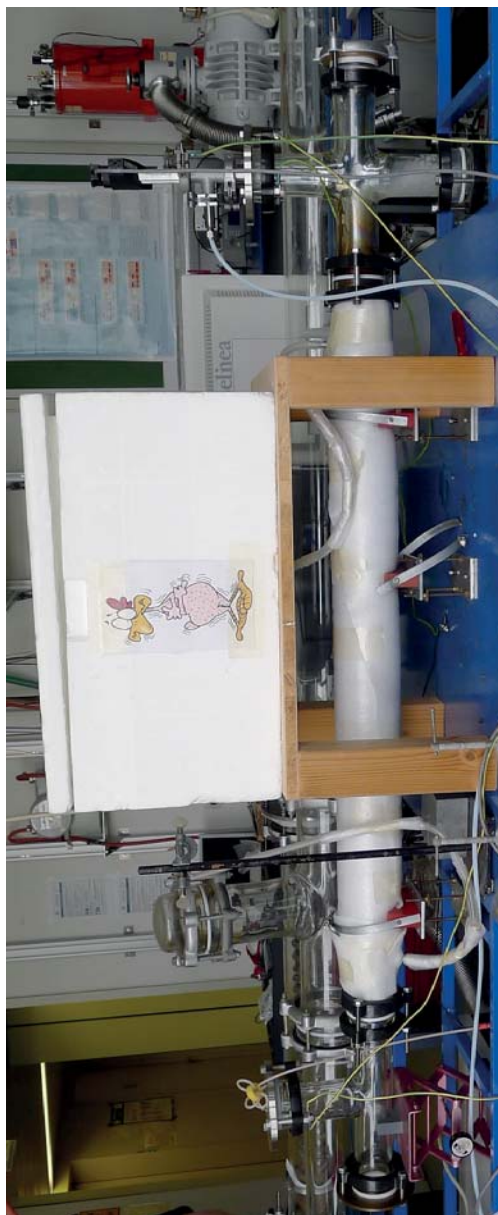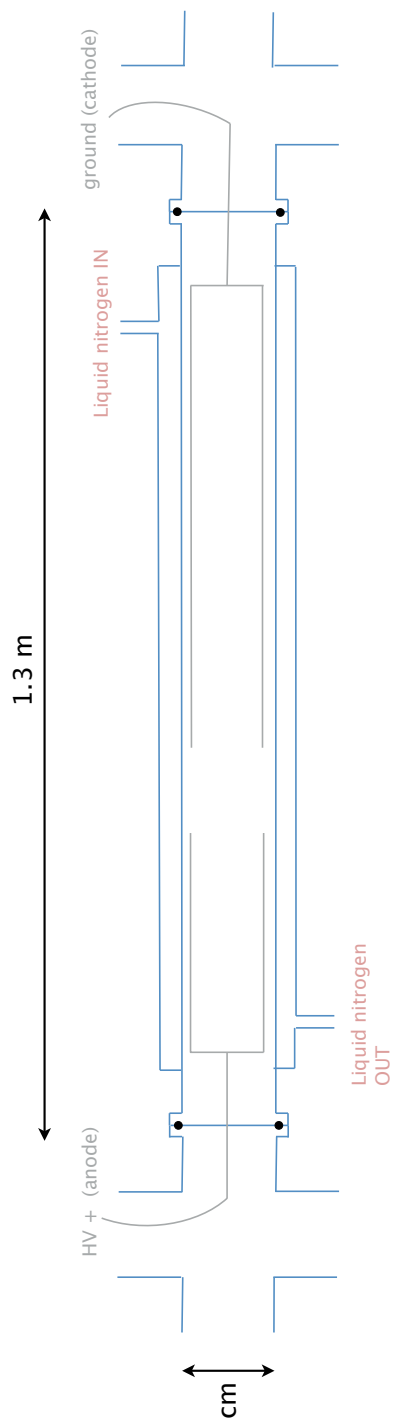
FIGURE 3.8: The newly developed discharge cell. It is composed by two layers. The outer layer contains the cooling liquid, while the inner cell contains the electrodes.

FIGURE 3.9: Jacket cell cooling system. A prototype of the new discharge cell made by the glass blower at the University of Cologne. It is composed by two layers. The outer layer is used for cooling the inner cell, where the electrodes are placed.

FIGURE 3.10: Example of a stainless steel electrode inside the new cell.
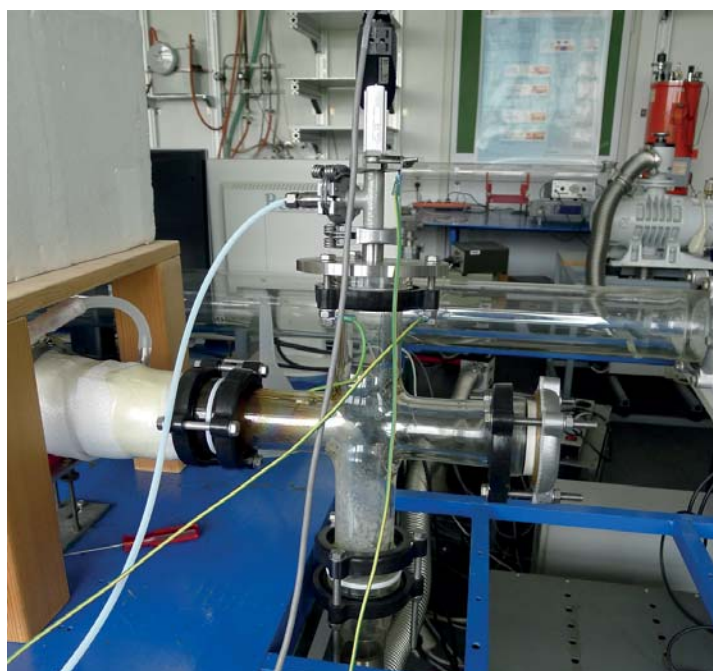
FIGURE 3.11: Connections in the New Discharge Cell

3.8 Characterization of the new discharge cell

One of the disadvantages in the old experiment was the lack of reliability. As the glue was falling off, the thermal connection between the coil and the inner cell was deteriorating. As a result, the spectra were not reproducible as the intensity of the lines was continuously changing. In the new experiment this problem has been solved by using a jacketed cell, so that the cooling agent is directly in contact with the inner cell, and the walls are directly cooled to 77 K. As a first step to characterize the cell, I decided to check the reliability of the spectra, now that it was possible. Many factors influence the intensity of a line: the focus of the radiation at the detector, the lock of the BWO frequency, the pressure inside the cell, the cooling, and the flow. I wanted to know what was the systematic error of the intensity of a measured line. In order to check the reliability, I measured a line of CO under different conditions:

- at room temperature

- at liquid nitrogen temperature

- at liquid nitrogen temperature with discharge

Table 3.1 summarizes these tests. During the tests the chopped power at the detector was kept constant, and the attenuation at the detector was 40 dBm. In the cases where the discharge was employed, the current was 80 mA and the voltage 0.5 kV. I took three measurements, five minutes away from each other (Experiment 1). In the table is reported the average of their intensities. All the measurements were repeated under the same conditions after switching off the whole instrument for few hours (Experiment 2). Finally I repeated the experiment 24 hours later (Experiment 3). The final result is that the relative error of a single measurement can be estimated to be around 20 %. The relative error has been calculated as the standard deviation divided by the mean value. In Figure 3.12 is shown the spectrum of the $N = 3$ - 2 transition of carbon monoxide at 345 GHz at a pressure of 5.1×10^{-2} mbar at room temperature, liquid nitrogen temperature, and with the discharge (at liquid nitrogen temperature). The line observed at liquid nitrogen temperature is more intense than the line at room temperature because the low temperature will enhance the population of the lower rotational levels of the carbon monoxide. The line measured with the discharge on is less intense

than the line measured with the discharge off (both measurements are taken at liquid nitrogen temperature). The reason for this behavior is a combination of the depletion of the carbon monoxide because of the discharge, and an increase in temperature because of the power introduced by the discharge in the gas, around 40 W. Also the population of the rotational levels will be affected by the discharge, leading to a decrease in signal intensity.
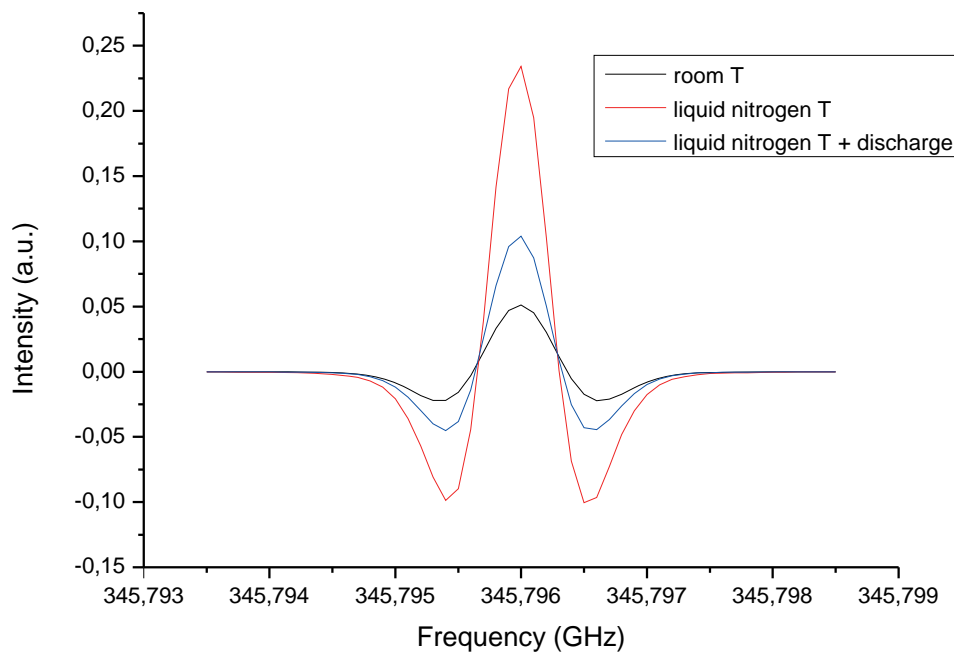
FIGURE 3.12: Spectrum of the $N = 3$ - 2 transition of carbon monoxide at 345 GHz at a pressure of 5.1×10^{-2} mbar at room temperature, liquid nitrogen temperature, and with the discharge (at liquid nitrogen temperature).

3.8.1   Production of ions

As can be seen in Figure 3.13 the first results with the new discharge cell were not as good as expected. The signal-to-noise (S/N) ratio in the spectrum of HCO^+ taken with the old cell is over 2500 while the same ratio in the first spectrum taken with the new cell is around 15, see Figure 3.13. The S/N has ben calculated per channel, by averaging the noise in some channels and taking the value of the channel with maximum intensity. The optimum conditions for the production of HCO^+ were slightly different, e.g. the optimal pressure in the new experiment

TABLE 3.1: Reliability tests for the new discharge cell

Experiment	Temperature (K)	pressure (mbar)	Discharge off	Intensity (arbitrary units)	Average Intensity	Relative Error
1	300	7.6×10^{-3}	off	283		
2	300	7.6×10^{-3}	off	283		
3	300	7.6×10^{-3}	off	386	317	15%
1	300	1.7×10^{-2}	off	160		
2	300	1.7×10^{-2}	off	193		
3	300	1.7×10^{-2}	off	225	193	14%
1	300	5.1×10^{-2}	off	509		
2	300	5.1×10^{-2}	off	589		
3	300	5.1×10^{-2}	off	775	624	18%
1	77	7.6×10^{-3}	off	185		
2	77	7.6×10^{-3}	off	137		
3	77	7.6×10^{-3}	off	229	184	20%
1	77	1.7×10^{-2}	off	103		
2	77	1.7×10^{-2}	off	90		
3	77	1.7×10^{-2}	off	133	109	17%
1	77	5.1×10^{-2}	off	237		
2	77	5.1×10^{-2}	off	209		
3	77	5.1×10^{-2}	off	361	269	25%
2	77	5.1×10^{-2}	on	103		
3	77	5.1×10^{-2}	on	162	132	18%

is one order of magnitude lower with respect to the old experiment. In the old experiment I was using a pressure of 4 mbar, while in the new experiment I use a pressure of 0.2 mbar. This was considered to be of secondary importance as the conditions were also different compared to the ones reported in the literature for similar experiments [39, 40]. I performed a series of tests in order to check whether a small amount of ions or a loss of radiation power was the reason for the worse signal-to-noise in the new experiment.

3.8.2   Less power or less ions

First I checked the possible losses in radiation power in three different ways:

- I tested the influence of the discharge on the noise of the spectrum by comparing the line of carbon monoxide with the discharge on and off. There was not a notable change in the noise.

- I tested the influence of a band pass filter and different detector gains on the noise, in order to check whether noise was added to the signal while processing it. Also this was found not to be the case.
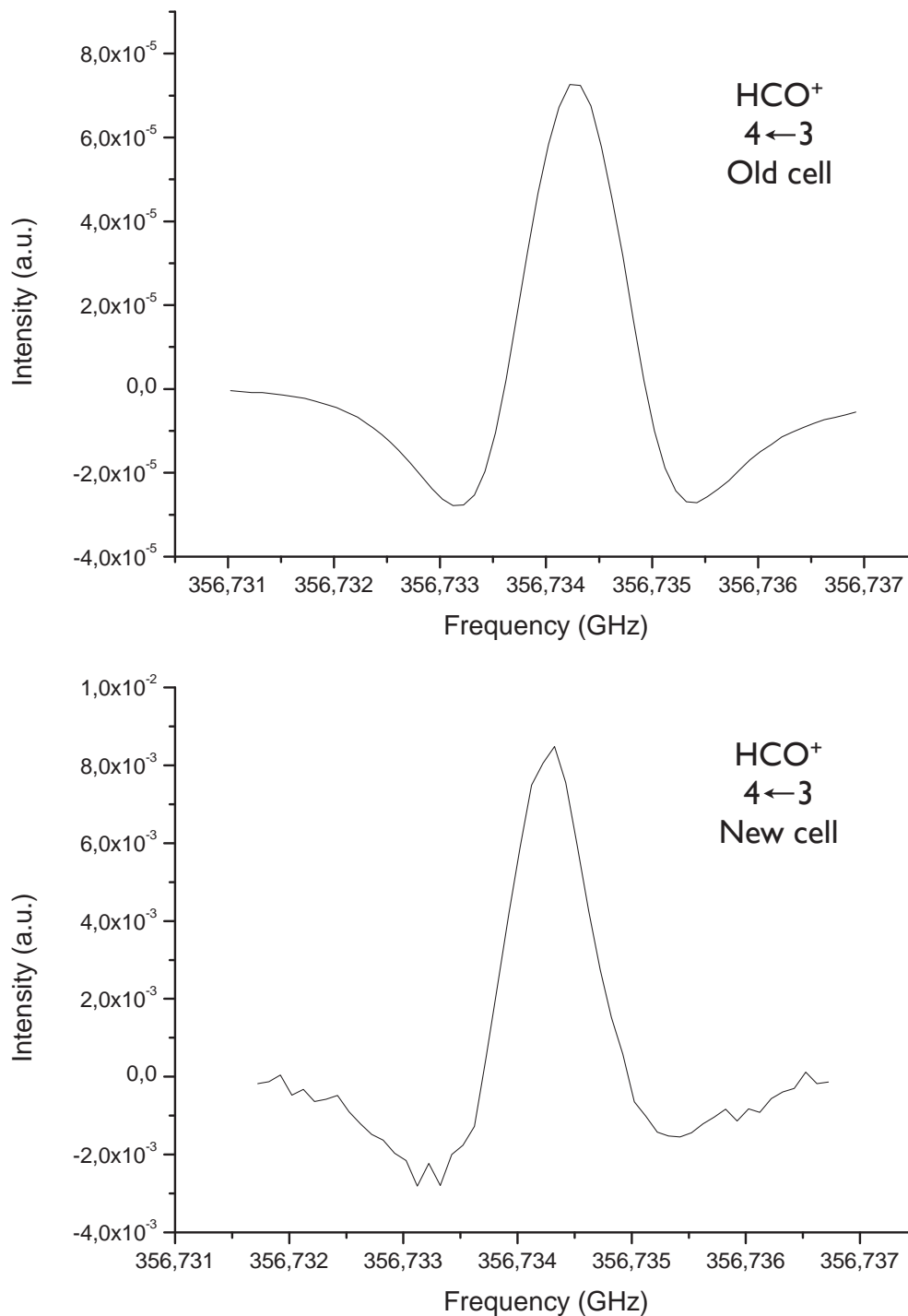
FIGURE 3.13: Comparison of the spectrum of HCO^+ in the old and the new discharge cell. The signal-to-noise in the old cell is 2500, while in the new cell is 15. Intensity units are arbitrary.

- One line of C^{18}O measured with the old experiment was compared to the same line measured with the new experiment in the same conditions. The signal-to-noise level was comparable.

These tests show that there is not less radiation power in the new experiment compared to the old one, as no notable change in the noise was found between the two experiments.

If less ions were produced, the reason could have been that the improvements done to have more ions were going in the wrong direction. The two main improvements from the old to the new cell were the better cooling, and the higher flow. In order to check whether less ions were produced, some tests were made to check whether the temperature was too low, or the flow too high. To check the latter, the line of HCO$^+$ was monitored while closing the valve that connects the cell with the pump. By slowly closing the valve, the line of the ion showed a decrease in intensity when the valve was almost fully closed. Hence, a slower flow did not improve the intensity of the line, but quite the contrary. In order to check the effect of the temperature, the HCO$^+$ line was monitored while letting the cell warm up. As soon as the "chicken feeder" was empty, i.e. there was no liquid nitrogen flowing in the cell anymore, the line of the ion quickly disappeared. From the last two tests we can conclude that the temperature was not too low, and the flow was not too high. In order to check whether less ions are produced in the new discharge cell, an estimate of the amount of ions produced in both apparatus has been made.

3.8.3   Counting ions

By comparing the line of CO at a known pressure (i.e. known N, number of molecules per cubic centimeter) with the intensity of a CO$^+$ line, we can retrieve the amount of ions produced in the cell. CO and CO$^+$ have been used to test the production of the ions in the cell. The peak intensity of an absorption line of a diatomic is given by (Townes and Shawlow, p. 24, 1-77)

$$\gamma = \frac{4\pi^2 h N f_J \mu^2 \nu^3}{3c(kT)^2 \Delta\nu} \tag{3.2}$$

with

$$f_J = \frac{(2J+1)exp^{-hBJ(J+1)/(kT)}}{Q_T} \tag{3.3}$$

where N is the number of molecules per cubic centimeter in the cell, f is the fraction of molecules in the lower J state, μ^2 is the dipole moment, ν is the line center frequency, $\Delta\nu$ is the half width at half maximum, c is the speed of light, k is the Boltzmann constant, h is the Planck constant, and Q_T is the rotational partition function at the temperature T.

$$\frac{N_{CO^+}}{N_{CO}} = \frac{f_J(CO)\mu^2(CO)\nu^3(CO)\Delta\nu(CO^+)\gamma(CO^+)}{f_J(CO^+)\mu^2(CO^+)\nu^3(CO^+)\Delta\nu(CO)\gamma(CO)} \tag{3.4}$$

Comparing the intensity of two spectral lines has to be done carefully. One needs to be careful because the signal is processed in various ways, and if the settings are not exactly the same (detector amplification, band-pass filter settings, or lock-in sensitivity for example), some calibrations have to be taken into account. Furthermore some approximations have to be made. There are two unknown parameters in the formula that defines the peak intensity of the absorption line: the fraction of molecules in the lower rotational state, and the temperature. The temperature of the cell's walls is not necessarily the temperature of the molecules in the discharge. To know the rotational temperature of the molecules it would be necessary to measure it spectroscopically. This is easily done by comparing the intensities of the lines in the K-ladder of an asymmetric rotor, but in the case of CO and CO$^+$ a wide frequency range would have to be covered. I have calculated the CO$^+$/CO ratio at different temperatures. If we assume that both CO and CO$^+$ have the same temperature, the ratio CO$^+$/CO is not affected by the temperature . The latter assumption is quite reasonable.

Instead, using the fraction of molecules in the lower J state as if the level would be in equilibrium is not necessarily a reasonable assumption. Both the CO and the CO$^+$ lines have been measured in the discharge. While in the discharge, the population of the rotational levels are scrambled away from equilibrium. It is not rigorous then to assume the equilibrium. But it is anyhow the assumption that we make for both the CO and CO$^+$ line. The lines of CO and CO$^+$ in the

new experiment have been measured in a 100 mA discharge of CO and Argon at 0.01 mbar and 0.15 mbar respectively. In the old experiment the lines have been measured in a pure CO discharge with 80 mA current at 0.01 mbar and 0.9 mbar respectively. The CO^+/CO ratio found in both experiments is around 10^{-5}. The reason of the poorer signal-to-noise ratio in the new experiment has to be found simply in the lower pressure used. With less precursor gas, less ions are produced. The typical pressure used in the old experiment was around one millibar, while in the new experiment the typical pressure for producing CO^+ is 0.1 millibar. It is not possible to use higher pressures in the new experiment since the discharge becomes unstable. This problem will be investigated in the future.

3.9   Discussion and future developments

The new discharge cell is currently a running experiment. It has been proven that ions can be produced in sufficient amounts. The new experiment is easier to handle and faster to use with respect to the previous one. Cooling the old discharge cell takes almost two hours, while the new discharge cell reaches liquid nitrogen temperature within 15 minutes. The new discharge cell is vacuum tighter than the previous one. The connections of the old cell were placed at the side of the window, and it was not possible to have these connections vacuum tight. A good vacuum is crucial for the production of ions since collisions with water and oxygen, for example, will most likely destroy the ions. When producing ions, cooling the cell is crucial as it increases the absorption coefficients. Low temperatures also slow down the ions on their way to the cell walls, where they dissociate. The chemistry is also more controlled at lower temperatures, as most of the molecules that contaminate the vacuum freeze out. The new cell has a very effective cooling system: the liquid nitrogen, or any other cooling agent, is in direct contact with the inner cell, as it is contained in the jacket around the latter.

The flow in the new discharge cell has been improved by a factor of 40 with respect to the old one. In the present apparatus the cell is in fact pumped through a bigger cross section (~ 20 cm^2 instead of ~ 1 cm^2). The results obtained in the new experiment are reliable and reproducible. The quality of the results in the old experiment was instead degrading, Due to the non cryo-specified thermal connection between the solenoid coil transporting the liquid nitrogen and the inner cell, which was falling off continuously, the measurements were not reproducible

in the old discharge cell. However, the discharge in the new cell does not sustain high pressures, it becomes unstable at 0.5 mbar. This problem will be addressed in the future. A wider range in operating pressure to find the best conditions for the production of a specific ion is desirable.

A system to release the gas sample directly at the center of the cell will be built. In the present configuration, see Figure 3.8, the gas is released right above the vacuum pump connection. Most of the sample is pumped out of the cell before feeding the discharge inside the cell. Introducing the sample directly in the center of the cell will improve the efficiency of the ion production.

In addition it has been shown by De Lucia and coworkers [35] that using a magnetic field of 150 - 200 Gauss increases the signal of positive ions by a factor of 50. The solenoid copper coil of the old discharge cell can in principle be used also for applying a magnetic field. Given the low number of turns the magnetic field that can be achieved with a reasonable current is quite low, around 2 Gauss. The new cell will be implemented in a solenoid coil capable of producing a magnetic field of 200 Gauss.

Velocity modulation is a technique that allows to distinguish the signal of the ions from neutral and radical signal. The ions are accelerated toward the electrode with opposite sign, when changing the polarity of the discharge, the ions will move accordingly. The resulting shift in frequency is characteristic of the ions, and allows to discriminate them from neutrals and radicals. It would be interesting to modify the new experiment in order to have the possibility to do velocity modulation and study ions of astronomical molecules, e.g. protonated methanol. Methanol has a very dense and rich spectrum. When discharging methanol to produce $CH_3OH_2^+$, the resulting spectrum will still be dominated by features from the neutral methanol as the neutral/ion ratio is normally around $10^6 - 10^5$. With the velocity modulation technique this problem can be partially solved. Methanol, dimethylether and acetone are very abundant in the interstellar medium, additionally they have a dense spectrum. It is very likely the presence in space of the cations, and possibly also the anions, related to such abundant molecules.

Chapter 4

Accurate Rest Frequencies for CO$^+$, ideal tracer for Photon-Dominated Regions

4.1   Introduction

CO$^+$ is the cation of the second most abundant molecule in space, carbon monoxide. However this small, open-shell cation is not as widespread as its neutral counterpart. CO$^+$ is in fact easily destroyed as it reacts almost on every collision with H$_2$ and H. Its abundance becomes important only in hot layers of photon-dissociation regions (PDRs), where hydrogen is mostly atomic [41]. CO$^+$ was successfully detected towards several PDRs, some of them associated with planetary nebulae [42–45], where it appears to be a good tracer of hot gas. In Figure 4.1 is shown the planetary nebula NGC 7027 where CO$^+$ was detected for the first time. Thus far, CO$^+$ emission lines have been observed with a rotational excitation temperature of 10 K, much lower than the temperature of the surrounding medium in a PDR, ranging from hundreds to thousands of Kelvin [42]. The processes that are responsible for this anomalous excitation are still poorly understood: Stäuber & Bruderer [46] suggest that CO$^+$ may be excited upon formation. To test their model, observations of high-N rotational transitions in the THz region are needed, probing the population of higher energy levels. Up to date, CO$^+$ has been observed in space only in the lowest rotational transitions, normally $N = 2 \rightarrow 1$ and $3 \rightarrow 2$, since $N = 1 \rightarrow 0$ is not observable because of atmospheric O$_2$. The recent development

of facilities such as SOFIA (GREAT operates in the 1.25-1.5 and 1.82-1.92 THz range) and ALMA (in full science it will operate in all atmospheric windows accessible from the ground between 80 and 900 GHz), has opened the far-infrared region to radioastronomy: those facilities are well suited to study the rotational excitation of CO$^+$.

FIGURE 4.1: The planetary nebula NGC 7027 seen in infrared.
Credit: W. B. Latter (SIRTF /Caltech) et al., NICMOS, HST, NASA

4.2   Previous work

Prior to this work, precise THz measurements of CO$^+$ were missing: Dixon et al. [47] measured for the first time the two components of the $N = 0 \rightarrow 1$ transition, the measurements have been extended up to 470 GHz by Sastry et al. [48]. Isotopically substituted species and vibrational excited states have also been studied [49–51]: ^{13}CO$^+$ and C^{18}O$^+$ in the lowest rotational transition for $v = 0$, and the main isotopic species in $v = 0 - 4$, C^{18}O$^+$ $v = 0, 1$, ^{13}CO$^+$ $v = 0, 1$ and ^{13}C^{18}O$^+$ $v = 0$. Savage and Ziurys [52] measured transition frequencies of the main isotopic species in the 200-590 GHz range with a newly built velocity modulation spectrometer. The sub-millimeter spectrum of ^{13}CO$^+$ has been extensively studied by Klapper [53]. The only far-infrared (supra-THz) measurements have been performed by van den Heuvel et al. [34], who reported the detection of a single

transition of CO^+ with a FIR side-band spectrometer with an accuracy of 1 MHz at 1.06 THz. Motivated by the lack of accurate data at high frequencies, this work combines the new data set on CO^+ (see Table 4.1) with all previous high resolution data to perform a global analysis. The aim is to obtain spectroscopic parameters for predictions at high frequencies (THz) with the accuracy needed for astronomical identification.

TABLE 4.1: Summary of new laboratory measurements of CO^+ for different isotopic species

Isotopic Species	v	Spectral Range (GHz)	Rotational Transition
$^{12}C^{16}O^+$	0	353-943	10
		1110-1300	4
	1	350-351	2
		700	1
$^{12}C^{18}O^+$	0	336-337	2
$^{13}C^{16}O^+$	0	338-901	19

Note: Including the data of Klapper [53]

4.3   Experimental details

For the production of CO^+ a discharge cell as described in Gendriesch et al. [54] was used, modified with a long hollow cathode to optimize the production of positive ions [34]. A description of the discharge cell can be found in the section 3.6 of Chapter 3 in this thesis. Typically 80 mA discharge current was used, through pure CO at a pressure of about 0.3 mbar. The experimental conditions were optimized for the production of CO^+, and a compromise had to be made between low pressure conditions and the production of the ions in a detectable amount. Although pressure broadening was observed in the CO precursor ($J = 3 - 2$) line, no frequency shift was detectable. $C^{18}O^+$ was measured in natural abundance, and $^{13}CO^+$ was measured in natural abundance in the new measurements while Klapper [53] used a 99% enriched sample. The cell walls were cooled to liquid nitrogen temperature for all measurements. Due to the electric field in the DC discharge, molecular ions are accelerated, and this drift produces a frequency shift that is not trivial to take into account. In order to cancel this shift, all new

measurements were taken in a double pass configuration: by letting the radiation counter-propagate in the cell the effect of the drift velocity of the ions in one direction cancels out. It was found that in a single-pass arrangement the shifts are of the order of 30 kHz at 350 GHz, which is well within the measurement uncertainties, so that single-pass measurements by Klapper [53] were not needed to be corrected prior to the analysis. The radiation sources employed in the 300-900 GHz range are phase-locked Backward Wave Oscillators (BWO). An example of a line measured with a BWO is shown in Figure 4.2. The signal, detected by a liquid Helium cooled InSb bolometer, is frequency modulated at $f = 8.7$ kHz, and then $2f$-demodulated by a digital lock-in amplifier, leading to the observed 2nd derivative line shape. At 1.1-1.3 THz, the radiation is generated by a commercial multiplier chain (Virginia Diodes, Inc.) which generates the 72nd harmonic of a 18 GHz synthesizer signal (Rhode & Schwarz). The THz lines of CO$^+$ that have been measured, are shown in Figure 4.3. More details about the experimental setup are reported in Chapter 3. The measured lines are reported in Table 4.2. The accuracy of the lines was estimated on the basis of signal to noise ratio and line shape. The center line frequency was derived by fitting the line profiles with the 2nd derivative of a gaussian.
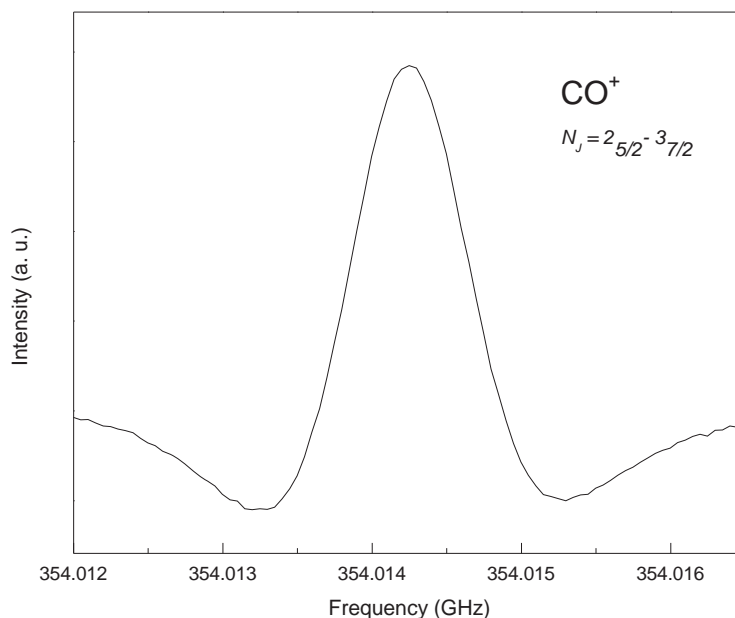
FIGURE 4.2: Spectrum of the $N_J = 2_{5/2} \rightarrow 3_{7/2}$ transition of ^{12}C^{16}O$^+$. The line shown is the sum of two scans, with total integration time of less than three minutes.

TABLE 4.2: Measured rotational transition frequencies of CO$^+$ [MHz] with uncertainties, quantum numbers and residuals *O-C* [kHz] between observed frequencies and those calculated from the final set of spectroscopic parameters

		CO$^+$					^{13}CO$^+$			
v	$N \to N'$	$J \to J'$	Frequency	O-C	v	$N \to N'$	$J \to J'$	$F \to F'$	Frequency	O-C
0	$0 \to 1$	$1/2 \to 1/2$	117692.360(30)^a	34	0	$0 \to 1$	$1/2 \to 1/2$	$1 \to 0$	112465.938(120)^a	-11
	$0 \to 1$	$1/2 \to 3/2$	118101.812(50)^a	15		$0 \to 1$	$1/2 \to 1/2$	$1 \to 1$	112695.175(80)^a	32
	$1 \to 2$	$3/2 \to 3/2$	235380.046(150)^b	-66		$0 \to 1$	$1/2 \to 3/2$	$1 \to 1$	112753.480(40)^a	37
	$1 \to 2$	$1/2 \to 3/2$	235789.641(30)^b	57		$0 \to 1$	$1/2 \to 3/2$	$1 \to 2$	112902.557(40)^a	80
	$1 \to 2$	$3/2 \to 5/2$	236062.553(20)^b	-11		$1 \to 2$	$1/2 \to 3/2$	$0 \to 1$	225444.382(200)^a	-55
	$2 \to 3$	$3/2 \to 5/2$	353741.223(30)^c	-49		$1 \to 2$	$3/2 \to 3/2$	$1 \to 2$	225504.854(70)^a	-17
	$2 \to 3$	$5/2 \to 7/2$	354014.257(20)^c	4		$1 \to 2$	$3/2 \to 5/2$	$2 \to 3$	225678.183(160)^a	-13
	$3 \to 4$	$5/2 \to 7/2$	471679.213(120)^b	-129		$2 \to 3$	$3/2 \to 5/2$	$1 \to 2$	338189.096(150)^c	143
	$3 \to 4$	$7/2 \to 9/2$	471952.343(100)^b	20		$2 \to 3$	$3/2 \to 5/2$	$2 \to 3$	338251.478(50)^c	47
	$4 \to 5$	$7/2 \to 9/2$	589599.236(100)^d	-15		$2 \to 3$	$5/2 \to 7/2$	$2 \to 3$	338377.449(50)^c	31
	$4 \to 5$	$9/2 \to 11/2$	589872.224(100)^d	-11		$2 \to 3$	$5/2 \to 7/2$	$3 \to 4$	338443.745(50)^c	33
	$5 \to 6$	$9/2 \to 11/2$	707496.506(100)^d	37		$3 \to 4$	$5/2 \to 7/2$	$2 \to 3$	450937.978(250)^d	-231
	$5 \to 6$	$11/2 \to 13/2$	707769.401(100)^d	-48		$3 \to 4$	$7/2 \to 9/2$	$3 \to 4$	451143.635(250)^d	-210
	$6 \to 7$	$11/2 \to 13/2$	825366.363(200)^d	-81		$3 \to 4$	$7/2 \to 9/2$	$4 \to 5$	451196.212(100)^d	-51
	$6 \to 7$	$13/2 \to 15/2$	825639.665(200)^d	240		$4 \to 5$	$7/2 \to 9/2$	$3 \to 4$	563672.549(100)^d	-231
	$7 \to 8$	$13/2 \to 15/2$	943204.603(250)^d	-35		$4 \to 5$	$7/2 \to 9/2$	$4 \to 5$	563713.663(100)^d	-78
	$7 \to 8$	$15/2 \to 17/2$	943477.836(200)^d	216		$4 \to 5$	$9/2 \to 11/2$	$4 \to 5$	563890.319(100)^d	-74
	$8 \to 9$	$15/2 \to 17/2$	1061005.9(10)^e	-611		$4 \to 5$	$9/2 \to 11/2$	$5 \to 6$	563931.766(250)^d	256
	$9 \to 10$	$17/2 \to 19/2$	1178767.451(200)^c	-69		$5 \to 6$	$9/2 \to 11/2$	$4 \to 5$	676387.165(200)^d	34
	$9 \to 10$	$19/2 \to 21/2$	1179040.392(100)^c	-108		$5 \to 6$	$9/2 \to 11/2$	$5 \to 6$	676420.085(100)^d	59
	$10 \to 11$	$19/2 \to 21/2$	1296756.174(100)^c	74		$5 \to 6$	$11/2 \to 13/2$	$5 \to 6$	676613.565(100)^d	6
	$10 \to 11$	$21/2 \to 23/2$	1296483.005(200)^c	-114		$6 \to 7$	$11/2 \to 13/2$	$5 \to 6$	789076.889(200)^d	97
1	$0 \to 1$	$1/2 \to 1/2$	116553.376(80)^a	111		$6 \to 7$	$11/2 \to 13/2$	$6 \to 7$	789103.863(200)^d	194
	$0 \to 1$	$1/2 \to 3/2$	116960.305(80)^a	16		$6 \to 7$	$13/2 \to 15/2$	$7 \to 8$	789336.965(200)^d	33
	$1 \to 2$	$1/2 \to 3/2$	233509.032(70)^a	18		$7 \to 8$	$13/2 \to 15/2$	$6 \to 7$	901737.536(100)^d	29
	$1 \to 2$	$3/2 \to 5/2$	233780.342(80)^a	22		$7 \to 8$	$15/2 \to 17/2$	$7 \to 8$	901975.512(100)^d	-39
	$2 \to 3$	$3/2 \to 5/2$	350320.005(50)^c	-5	1	$0 \to 1$	$1/2 \to 3/2$	$0 \to 1$	111687.554(70)^a	-146
	$2 \to 3$	$5/2 \to 7/2$	350591.300(50)^c	-60		$0 \to 1$	$1/2 \to 3/2$	$1 \to 2$	111835.716(100)^a	15
	$5 \to 6$	$6/2 \to 7/2$	700924.571(150)^d	91		$1 \to 2$	$3/2 \to 5/2$	$2 \to 3$	223545.426(80)^a	26
2	$0 \to 1$	$1/2 \to 1/2$	115411.284(80)^a	-7						
	$0 \to 1$	$1/2 \to 3/2$	115814.790(80)^a	82			^{13}C^{18}O$^+$				
	$1 \to 1$	$1/2 \to 3/2$	231221.423(180)^a	-36		$0 \to 1$	$1/2 \to 1/2$	$1 \to 1$	107081.520(80)^a	70
	$1 \to 1$	$3/2 \to 5/2$	231490.470(180)^a	66		$0 \to 1$	$1/2 \to 3/2$	$0 \to 1$	107137.965(60)^a	18
3	$0 \to 1$	$1/2 \to 3/2$	114665.212(120)^a	159		$0 \to 1$	$1/2 \to 3/2$	$1 \to 2$	107278.209(60)^a	89
4	$0 \to 1$	$1/2 \to 3/2$	113511.230(100)^a	-94						

		C^{18}O$^+$		
0	$0 \to 1$	$1/2 \to 1/2$	112088.491(40)^a	30
	$0 \to 1$	$1/2 \to 3/2$	112478.502(40)^a	91
	$1 \to 2$	$3/2 \to 3/2$	224172.862(180)^a	55
	$1 \to 2$	$1/2 \to 3/2$	224562.753(60)^a	-2
	$1 \to 2$	$3/2 \to 5/2$	224822.772(90)^a	51
	$2 \to 3$	$3/2 \to 5/2$	336898.495(100)^c	-338
	$2 \to 3$	$5/2 \to 7/2$	337158.761(100)^c	55
1	$0 \to 1$	$1/2 \to 3/2$	111417.700(60)^a	-36
	$1 \to 2$	$1/2 \to 3/2$	222443.650(140)^a	-5
	$1 \to 2$	$3/2 \to 5/2$	222702.180(70)^a	56

^{a} Bogey et al., 1983
^{b} Sastry et al., 1981
^{c} This work
^{d} Klapper, 2001
^{e} van den Heuvel, 1982

Note: Numbers in parentheses are 1σ uncertainties in kHz
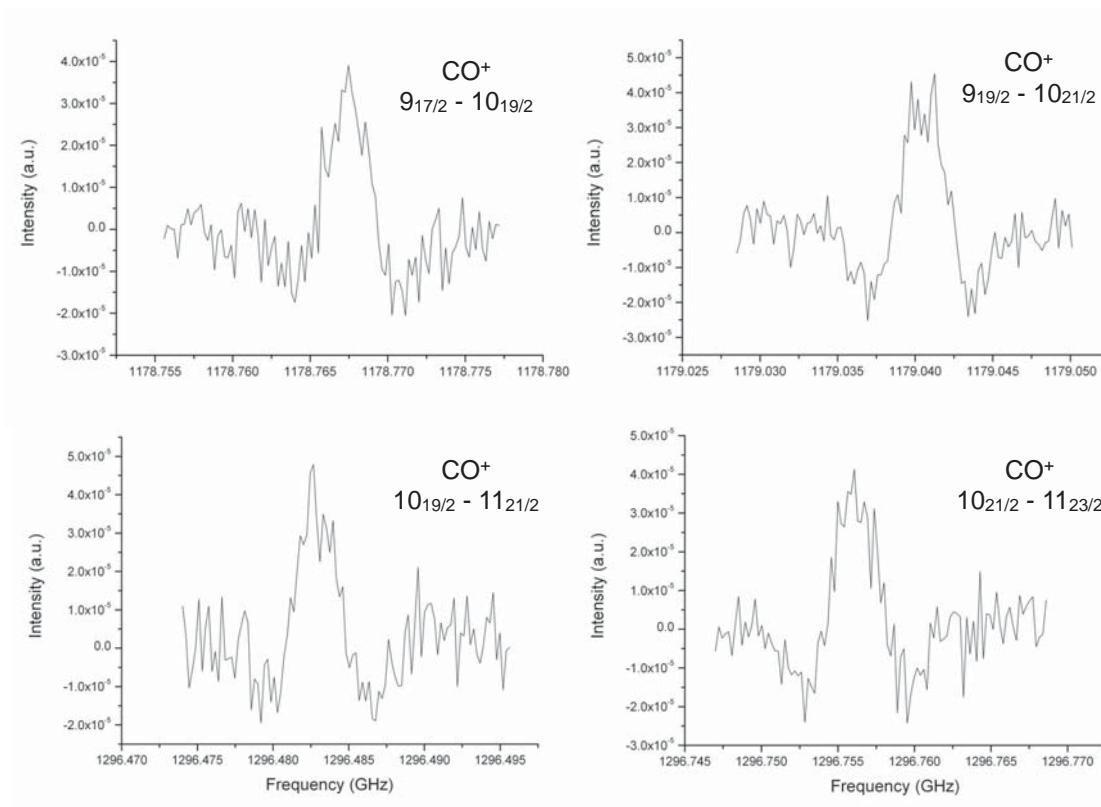
FIGURE 4.3: Spectra of the lines of CO$^+$ measured for this work. The lines shown are the average of forty scans, with a total integration time of about thirty minutes.

4.4 Analysis

The open shell CO$^+$ ($^2\Sigma^+$) has a considerably large dipole moment of 2.61 Debye [55]. Owing to the presence of an unpaired electron, CO$^+$ has an electronic spin of $\frac{1}{2}$ so each rotational level N is split in two, $J = N \pm 1/2$. The allowed transitions follow the $\Delta J = 0, \pm 1$ selection rule, but the transitions with $\Delta J = 0$ are much weaker than the other two, and have intensities below the noise level for most of the transitions. A scheme of the energy levels in CO$^+$ is reported in Figure 4.4. In the case of ^{13}CO$^+$ there is further splitting due to the presence of the nuclear spin of $I = \frac{1}{2}$ of ^{13}C, so the quantum numbers are expressed in this way: $J = N \pm 1/2$, and $F = J \pm 1/2$. In this case the selection rules are $\Delta J = 0, \pm 1$ and $\Delta F = 0, \pm 1$. An example of the energy levels in ^{13}CO$^+$ is reported in Figure 4.5: the solid lines represent the observed transitions, while the dotted lines are allowed but not observed transitions, because they are too weak.
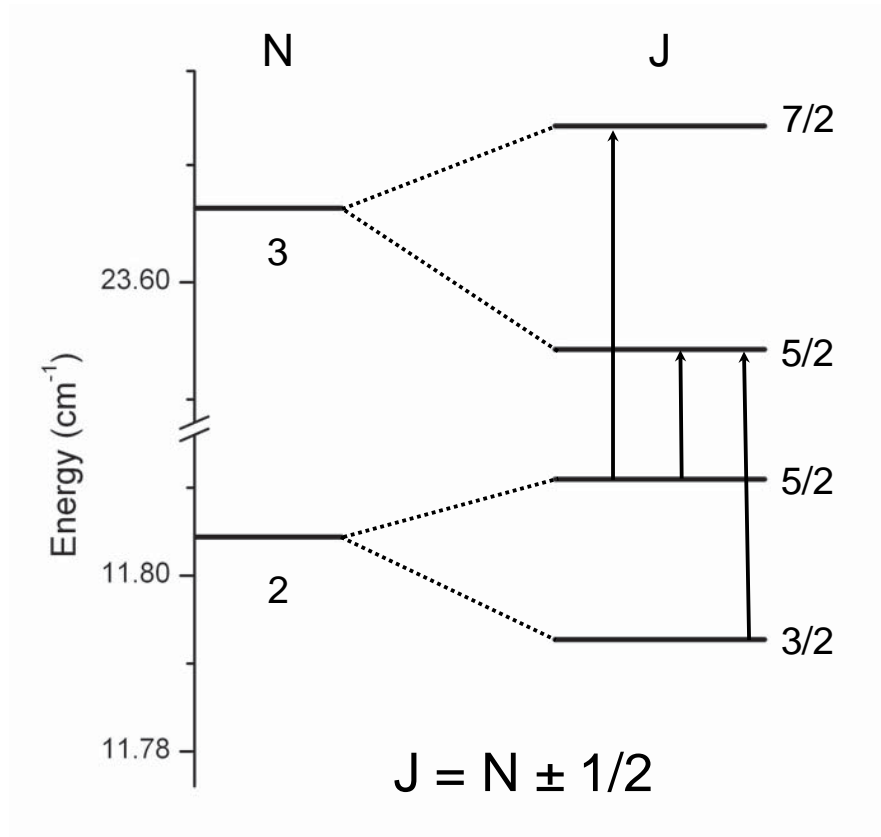
FIGURE 4.4: Energy levels of CO$^+$ involved in the $N = 2 \rightarrow 3$ transition

An isotopically invariant fit has been performed with SPFIT and SPCAT [8] using the data from this work, and from previous works [34, 48, 51, 53]. The theory is described in Chapter 2. All masses used in this work are taken from the 2003 Atomic Mass Evaluation (AME), except for ^{18}O which is taken from a more recent Penning-trap experiment [56]. All measurements included in the fit are summarized in Table 4.2. The molecular parameters derived from this fit are reported in Table 4.3, where $Y_{l,m}$ are the Dunham coefficients, $\Delta_{l,m}$ are the corrections to the BO approximation, $\gamma_{l,m}$ are the spin-rotation interaction constants, b_F and c are the isotropic (Fermi contact interaction) and anisotropic part of the electron spin-nuclear spin coupling constants respectively. Instead of Y_{01}, U_{01}/μ was determined in the fit because of the BO correction. Also the Δ_{01} were not determined directly, but $\delta_{01}^X = \Delta_{01}^X \times \frac{m_e}{M_X} \times \frac{U_{01}}{\mu}$ are used in the fit.

In the fit the value of Y_{03} could not be well determined, so it was calculated in the following way:

$$Y_{03} = H_e = \frac{2D_e}{3\omega_e^2}(12B_e^2 - \omega_e\alpha_e) = 1.2905 \times 10^{-7}\text{MHz} \qquad (4.1)$$
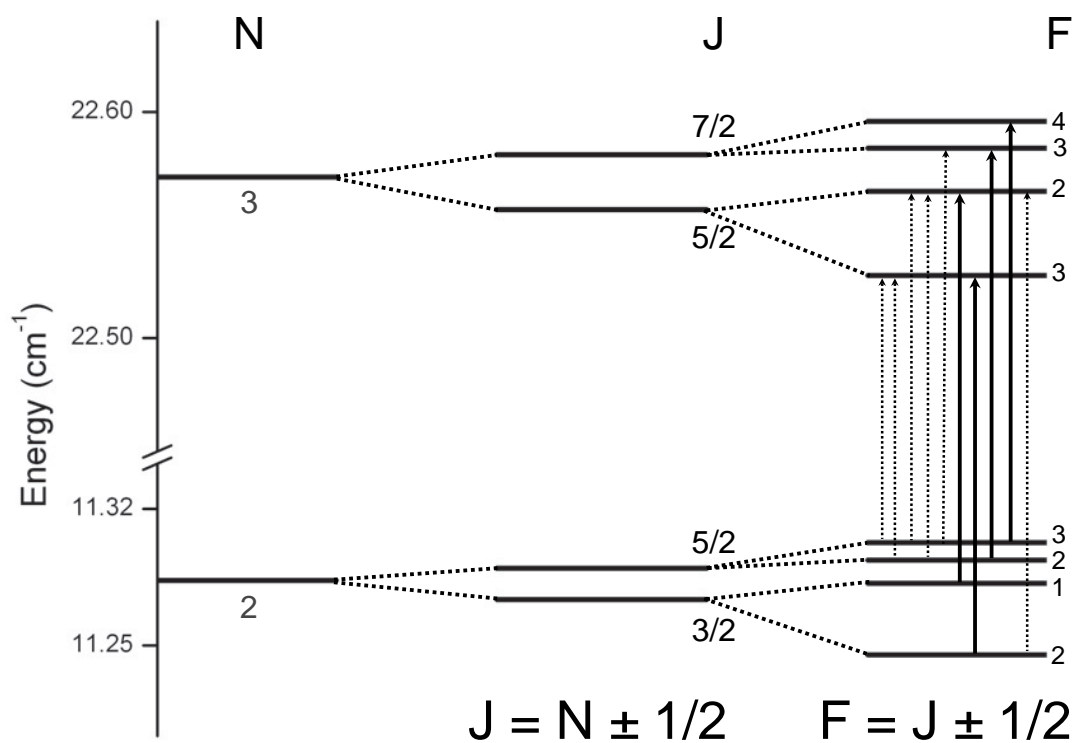
FIGURE 4.5: Energy levels of ^{13}CO$^+$ involved in the $N = 2 \to 3$ transition. The solid lines are observed lines, while the dotted lines are allowed but not observed lines.

using the constants given in Bogey et al. [51], and kept fixed during the fit. I tried to extract also the value of b_{F10} from the fit, the first vibrational correction to the Fermi contact constant, but the value of the parameter was not well determined.

TABLE 4.3: Spectroscopic parameters of ^{12}C^{16}O$^+$ (MHz)

	This work	Bogey et al. [51]
U_{01}/μ	59270.233(76)	59270.406(165)[a]
Y_{01}	59267.5143(80)[b]	59267.5205(103)
Δ_{01}^C	$-0.226(14)$[b,c]	$-0.269(36)$[a]
Δ_{01}^O	$-1.033(31)$[b,c]	$-1.060(28)$[a]
Y_{11}	$-568.503(18)$	$-568.492(20)$
Y_{21}	$-0.9217(19)$	$-0.9267(71)$
Y_{02}	$-0.189136(17)$	$-0.18965(21)$
$Y_{03} \times 10^{-7}$	1.2905[d]	–
γ_{00}	273.505(49)	273.550(43)
γ_{10}	$-0.856(104)$	$-0.936(91)$
γ_{20}	$-0.387(37)$	$-0.362(31)$
c_{00}	150.30(27)	–
b_{F00}	1526.86(74)	1525.8(12)

Note: Numbers in parentheses are 1σ uncertainties in units of the least significant figures, [a]Calculated from U_{01} and μ, [b]Derived value, [c]Dimensionless parameter, [d]Kept fixed during the fit

4.5   Discussion

As can be seen in Table 4.3, the spectroscopic parameters determined in the present study agree within their experimental uncertainties with those obtained by Bogey and co-workers [51], but they are considerably more accurate. The weighted rms (root-mean-square deviation) of our final global fit including all data is 0.94. The weighted rms for the partial fit which includes just the measurements from this work is 0.99. The weighted rms for the partial fit which includes just the data set of Bogey et al. [51] and Sastry et al. [48] are 0.78 and 1.03, respectively. The accuracies of the lines in Table 4.2 were estimated based on the line shape and signal-to-noise ratio, and were treated by SPFIT as absolute values. Table 4.4 compares the Born-Oppenheimer breakdown terms $\Delta_{l,m}$ derived for CO$^+$ with the $\Delta_{l,m}$ of CO and of the isoelectronic CN and BO. The Δ_{01} for CO and CO$^+$ are significantly different because the two species do not have the same number of valence electrons. On the contrary, with CN being isoelectronic with CO$^+$ the values for these two molecules are expected to be comparable. What we observe is that the Δ_{01}^C are quite different while the $\Delta_{01}^{O/N}$ are almost the same. A possible explanation for this behavior could be the fact that in both molecules the unpaired electron is largely localized on the carbon atom [57].

Further investigations on the Born-Oppenheimer breakdown parameters for iso-electronic molecules would be fruitful to check if it is possible to spot a trend in the behavior of these parameters. Boron monoxide, BO, is also isoelectronic with CO$^+$ and CN but a comparison with experimentally derived values of Δ_{01} is not possible. To my knowledge there is no isotopically invariant fit available in the literature. No accurate data is available for species containing ^{18}O, therefore there are no Δ_{01} values available and it was not possible to set up an isotopic invariant fit with the data available from the literature.

Gauss and Puzzarini [58] have demonstrated that quantum-chemical calculations can be used to determine Born-Oppenheimer breakdown parameters for the rotational constants of a diatomic. Recently they have extended their protocol to open-shell molecules for the determination of the Born-Oppenheimer breakdown parameters, and they used CO$^+$, CN and BO as a test [59]. The first calculation of Born-Oppenheimer breakdown parameters of boron monoxide, BO, is now available. The values are reported in Table 4.4, and their accuracy is expected by the authors to be in the order of 30%. The possible trend depending on the localization of the unpaired electron that can be spotted in the Δ_{01} of CO$^+$ and CN, is not found in the Δ_{01} values for boron monoxide. However, it may be a too simplistic way to look at the Born-Oppenheimer breakdown parameters. In the same paper, the values on CO$^+$ reported in this work have been used for testing their calculated values. I made a test to fit the experimental data set by using the constants reported in Table 4.3, but the Δ_{01}^C and Δ_{01}^O were kept fixed to the values reported in [59]. The rms of the fit goes from 0.9 to 10. Using higher order constants such as Δ_{11} or Δ_{02} in order to compensate helps the final rms of the fit. It becomes respectively 4 and 8, but the values of the Δ_{11} and Δ_{02} are too large to have a physical meaning.

TABLE 4.4: Comparison of Born-Oppenheimer breakdown terms

	CO$^+$ (present work)	CO (George et al. [60])	CN (Salek et al. [61])	BO (Puzzarini et al. [59])
$\Delta_{01}^{C/B}$	$-0.226(14)$	$-2.05603(23)$	$-0.895(11)$	-0.89
$\Delta_{01}^{O/N}$	$-1.033(31)$	$-2.09934(28)$	$-1.056(73)$	-1.77

4.5.1 Bond length

The equilibrium bond lengths for CO$^+$ are calculated for several isotopic species with $r_e = \sqrt{\frac{X}{B_e \times \mu}}$, as in Müller et al. [62], and are reported in Table 4.5.

$X = (505379.0094 \pm 0.0034)$ amu MHz Å^2 is a conversion factor and μ is the charge corrected reduced mass. The small difference between B_e and Y_{01} could not be determined with confidence for the present parameters plus those of the $A - X$ electronic spectrum [63], mainly because of the large uncertainty in Y_{20}, so we used $Y_{01} = B_e$. In the case of the Born-Oppenheimer approximation the bond distance has been calculated as $r_e = \sqrt{\frac{X}{U_{01}}}$, and is independent of the isotopic species. The difference in the bond lengths of the isotopic species, determined by taking into account the breakdown of the Born-Oppenheimer approximation, are in the order of 10^{-4} pm, and are thus very small as one might expect from the small Born-Oppenheimer breakdown parameters, but determined with significance. On the other hand, the Born-Oppenheimer equilibrium bond length differs by a much greater value, around 2.4×10^{-3} pm. The error introduced by the assumption $Y_{01} = B_e$ may lead to errors outside the uncertainties of the BO-corrected bond length, but is most probably within the uncertainty of the equilibrium bond length.

TABLE 4.5: Equilibrium bond length for CO⁺ in the Born-Oppenheimer approximation, and for several isotopic species considering the deviation from the Born-Oppenheimer approximation.

Species	r_e (pm)
CO$_e^{+(BO)}$	111.517760(64)
^{12}C^{16}O⁺	111.5203128(67)
^{13}C^{16}O⁺	111.5200927(65)
^{12}C^{18}O⁺	111.5202683(86)
^{13}C^{18}O⁺	111.5200482(86)

4.6 Conclusions

Accurate THz measurements have been performed on CO⁺, leading to a more accurate fit and improved predictions at high frequencies: for example the previously predicted value for the $N_J = 10_{21/2} \rightarrow 11_{23/2}$ line at 1.29 THz in the CDMS catalog was off by 1.5 MHz from the observed value, while with the improved predictions, this transition instead has a calculated uncertainty of only 560 kHz at 2.5 THz. The measured and predicted high-N transitions of CO⁺ will be useful for future astronomical observations. Ideal test candidates would be planetary nebulae and proto-planetary nebulae [42, 64].

Table 4.6 lists THz lines of possible astrophysical interest, reporting only the two strongest components of each rotational transition. Predictions based on the

present isotopically invariant fit are available online via the Cologne Database for Molecular Spectroscopy [6] at http://www.cdms.de.

TABLE 4.6: ^{12}C^{16}O$^+$ THz lines of astrophysical interest

$N \to N'$	$J \to J'$	Frequency (MHz)	
$8 \to 9$	$17/2 \to 19/2$	1061006.488(37)	HIFI
$8 \to 9$	$15/2 \to 17/2$	1061279.469(36)	HIFI
$10 \to 11$	$21/2 \to 23/2$	1296483.150(67)	APEX
$10 \to 11$	$19/2 \to 21/2$	1296756.131(66)	APEX
$11 \to 12$	$23/2 \to 25/2$	1414148.864(89)	GREAT
$11 \to 12$	$21/2 \to 23/2$	1414421.844(89)	GREAT
$15 \to 16$	$31/2 \to 33/2$	1884221.823(232)	GREAT
$15 \to 16$	$29/2 \to 31/2$	1884494.803(233)	GREAT

4.7   Perspectives

The $N = 5 \to 4$ transition of CO$^+$ has been recently detected toward Orion-S with the HIFI instrument on board of the Herschel Space Observatory in the framework of a project focused on the study of reactive ions in PDRs [9]. This is the first detection of CO$^+$ in Orion-S, and the first high-N CO$^+$ transition detected in space. Prior to this detection, CO$^+$ had only been observed in the $N = 2 \to 1$ and $N = 3 \to 2$ transitions, while the $N = 1 \to 0$ cannot be observed due to atmospheric O$_2$. It is puzzling that the same transition has not been detected toward the Orion bar for the same rms noise level. As the column densities in the two regions are predicted from the Meudon code* to be very similar, the difference is likely to be related to different excitation conditions in the regions, rather than differences in the chemistry. The comparison between CO$^+$ in the Orion-S and in the Orion bar cannot be made at the moment, as the $N = 5 \to 4$ transition is the first CO$^+$ line observed in Orion-S. Given the lack of lower N transitions, the information on the excitation of this small cation is limited. In order to fill this gap, observations of lower N transitions have been performed with the APEX telescope using the FLASH heterodyne receiver during the summer of 2013. A fairly large region covering most of the Orion-KL, Orion-S and the Orion bar has been imaged. Two fine components of the $N = 3 \to 2$ CO$^+$ transitions have been observed toward Orion-S. The analysis of the data is currently in progress.

---

*http://pdr.obspm.fr/PDRcode.html

Chapter 5

First Interstellar Detection of $c\text{-}\mathrm{C_3D_2}$

5.1 Introduction

Molecules are tracers of both physical and chemical properties of the Interstellar Medium (ISM). When studying an astrophysical object, we can infer information about physical quantities such as density, temperature and kinematics from the molecular line shapes. Furthermore the study of the chemical inventory of a particular source is crucial to understand the evolution of the source itself. As different regions of dense cores are traced by different molecules, it is required to have multiple line observations and continuum mapping in order to fully understand both structure and evolutionary status of a particular object that may eventually form a protostar. The molecular inventory changes very much from the warmer, less dense envelopes to the colder, denser cores. For example the chemistry of warm star forming regions is characterized by complex molecules such as dimethylether (DME) and methyl formate [65]. In the case of cold dark clouds instead, unsaturated molecules, long carbon chains and radicals are predominant [66]. Deuterium-bearing molecules, and even more their multiply deuterated variants, are good tracers for the colder interior regions of dense cores. Dense cloud cores have temperatures as low as 10 K and densities of 10^4 - 10^6 cm^{-3}. They are made of molecular material, mostly $\mathrm{H_2}$, and sometimes they are referred to as "dark clouds" because they are opaque in the optical wavelength regime. Low-mass stars are believed to be formed in these clouds.

5.1.1   Deuterium chemistry in the interstellar medium

Investigating deuterium chemistry is useful to put constraints on the ionization fraction, temperature, density and thermal history of dense molecular clouds [67–70]. The observations of multiply deuterated molecules in space, e.g. by Ceccarelli et al. (2007) [71] and references therein, have shown the necessity to reexamine some reaction rates in chemical networks [72], elemental D/H ratio in cold dense gas [73] and the density structure in sources such as L1544 and ρ Oph D [74], as well as the effects of accretion on grains [75], possible effects of internal dynamical motion [76], and the evolution of ice mantles in dense clouds and cores [69, 70].

The first multiply deuterated interstellar molecule detected has been D_2CO almost twenty years ago [77]. Since then, the study of deuterated molecules in the ISM has rapidly increased as they have been proven to be a unique observational probe of the early stages in low-mass star formation. Multiply deuterated species such as triply deuterated ammonia have been detected with a surprisingly high abundance ratio of 10^{-4} with respect to their fully hydrogenated forms [78]. By comparing this ratio to the elemental D/H ratio (1.65×10^{-5} [79]) it is easily seen that there is a remarkable enrichment in deuterium in this and other molecules. In IRAS 16293-2422 Ceccarelli and coworkers [80] measured the ratio of $D_2CO/H_2CO = 5\%$. In the same source Parise [81] measured $CD_3OH/CH_3OH = 1.4\%$. This enrichment in deuterium has mainly been explained by the exothermicity of the H-D exchange reactions, and by the depletion of CO and O onto dust grains [82, 83]. This depletion enhances the abundance of the multiply deuterated forms of H_3^+ and, upon dissociative recombination, the D/H ratio in molecules. Roberts et al. (2003) [84] calculated D/H abundance ratios close to 0.3 (20,000 times the cosmic value), in regions with large amount of CO freeze-out.

The multiply deuterated species detected in the ISM so far are:

- H_3^+ (H_2D^+, D_2H^+) [85]

- Water (HDO, D_2O) [86, 87]

- Methanol (CH_2DOH, CHD_2OH, CD_3OH) [81]

- Ammonia (NH_2D, NHD_2, ND_3) [88]

- Formaldehyde (HDCO, D_2CO) [80]

- Hydrogen Sulfide (HDS, D_2S) [89]

- Thioformaldehyde (HDCS, D_2CS) [90]

New probes for multiple deuteration are needed in order to constrain the models. Furthermore, probes for the reactions that happen in the gas phase are needed to better understand the interplay between the gas phase and grain surface deuteration reactions. Among the multiply deuterated species detected so far, only the isotopic species of H_3^+ are formed solely in the gas phase. Laboratory experiments have demonstrated that the deuteration of methanol at very low temperatures happens solely on grains [91–93]. For formaldehyde instead both gas phase- and grain surface-reactions are required to reproduce the observed abundances. Deuteration of ammonia can be reproduced with gas-phase models (e.g. Roueff et al. 2005 [88]), although NH_3 and its deuterated forms are also expected to form on grains [94]. Cyclopropenylidene is an unique probe to test the deuteration in the gas phase since it is believed to be formed solely in the gas phase [95].

5.1.2 Cyclopropenylidene

Cyclopropenylidene is a three-membered carbon ring. It is a reactive molecule, and the most stable molecule composed by three atoms of carbon and two atoms of hydrogen [96]. Its structure, derived from a study of eight isotopic species [97], is shown in Figure 5.1. It is a carbene, so it has two unshared valence electrons. Due to the presence of the two unshared electrons the molecule has a considerably high dipole moment (3.27 Debye [98]). Given its very bright lines, cyclopropenylidene was observed in the interstellar medium before its laboratory identification [99, 100]. This molecule is a nice example of the synergy between laboratory spectroscopy and observations that has driven the growth of molecular astrophysics and astrochemistry up to the point where we stand now. A very strong unidentified line, U85338, was detected and later on associated with some other unidentified radio lines. A laboratory search was performed by Thaddeus and coworkers at the Columbia University in order to find the carrier of these U-lines. They succeeded in producing these lines in the same acetylene-helium discharge that was used to produce C_3H [101]. The first detection of *c-*C_3H_2 in the laboratory [100] allowed the identification of several U-lines previously detected in space [99], namely the strong lines at 85338 and 18343 MHz. Since its first identification in 1985, *c-*C_3H_2

has been proven to be one of the most abundant and widespread molecules in our Galaxy. It has been observed in diffuse gas, cold dark clouds, giant molecular clouds, photodissociation regions, circumstellar envelopes, and planetary nebulae [100, 102–104]. Given the high abundance of the normal species, both *c*-C$_3$HD and the singly substituted ^{13}C species (off axis) have been observed with a good signal-to-noise ratio in cold dark clouds. Furthermore, cyclopropenylidene shows an enhancement in deuterium fractionation in cold dark clouds, e.g. Gerin et al. (1987) [105] measured a 1:5 intensity line ratio of the $2_{1,2}$ - $1_{0,1}$ lines of *c*-C$_3$HD and *c*-C$_3$H$_2$ in TMC1. The reactions which lead to such high deuteration are still poorly understood. Some rates of reactions which may be involved in the formation of deuterated *c*-C$_3$H$_2$ have been measured by Savíc et al. (2005) [52], but to my knowledge they have not been included in models so far. It was not until 2012 that high resolution laboratory data was available on the doubly deuterated species of *c*-C$_3$H$_2$, *c*-C$_3$D$_2$ [97], allowing its first search in space.
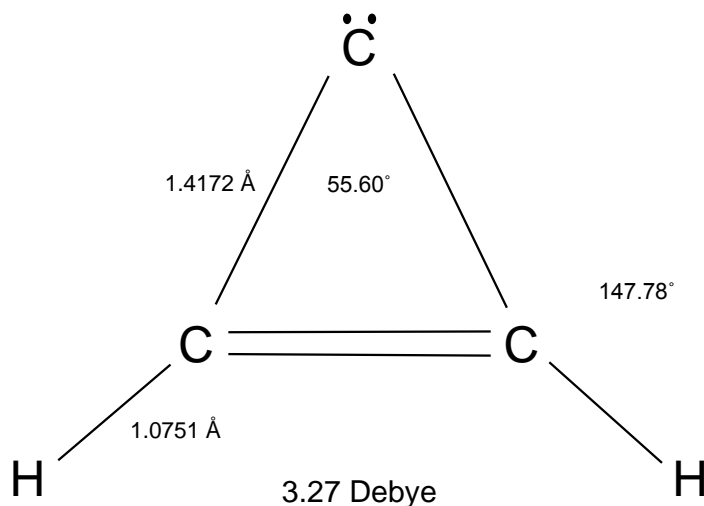
FIGURE 5.1: Empirical equilibrium structure of cyclopropenylidene. Bond lengths are in Å, and angles are in degrees [97].

5.1.3 Doubly deuterated cyclopropenylidene in the laboratory

I measured the rotational spectrum of *c*-C$_3$D$_2$ in the laboratory for the first time when I was a pre-doctoral fellow at the Harvard Smithsonian Center for Astrophysics in Cambridge (MA), USA [97]. Like its fully hydrogenated counterpart,

c-C$_3$D$_2$ presents the spectrum of an oblate asymmetric top with b-type transitions. Furthermore, c-C$_3$D$_2$ shows a deuterium quadrupole splitting resolvable at very low J. Given the presence of two equivalent off axis bosons, it has *ortho* and *para* symmetry species with a relative statistical weight of 2:1. The centimeter-wave spectra of normal and isotopic c-C$_3$H$_2$ were recorded with the same Fourier Transform Microwave (FTM) spectrometer and discharge source used to produce many highly reactive molecules [106]. c-C$_3$D$_2$ was observed in a discharge of fully deuterated acetylene. In Figure 5.2 an example of the spectra of c-C$_3$D$_2$ taken with the FTM spectrometer is shown. Millimeter-wave lines of c-C$_3$D$_2$ were measured with a 3 m long free space double-pass absorption spectrometer [107]. c-C$_3$D$_2$ was produced in a DC discharge (100 mA) of DCCD, CO, and Ar, with the walls of the discharge cell cooled to 150 K. Prior to this work, c-C$_3$D$_2$ had not been observed in the millimeter band, so the initial search was guided by frequencies calculated with spectroscopic constants derived from the centimeter-wave measurements. Unambiguous assignment of the first few lines was established by observing the *ortho/para* doublets at 178.3, 205.7, and 233.1 GHz with the predicted separation in frequency and 2:1 ratio in intensity. In Figure 5.3 is shown the doublet at 233 GHz as an example of the characteristic *ortho/para* intensity ratio in c-C$_3$D$_2$.
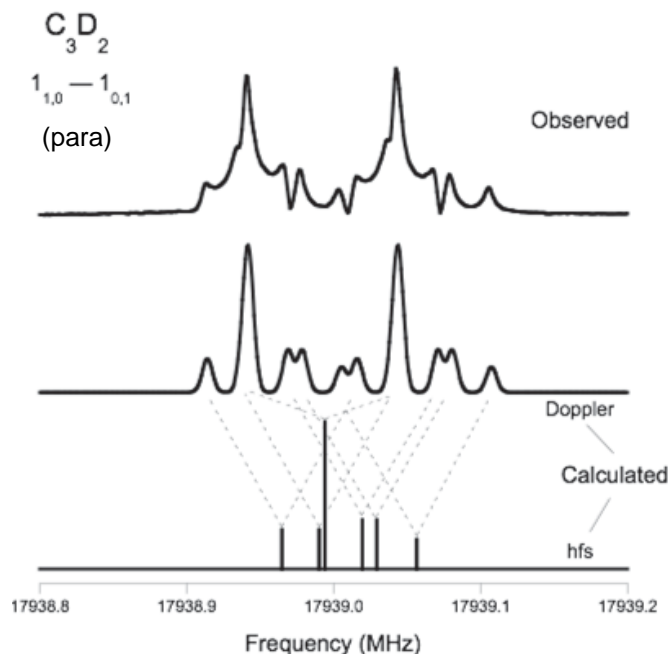
FIGURE 5.2: The $1_{1,0}$-$1_{0,1}$ transition of c-C$_3$D$_2$ observed with the Fourier Transform Microwave Spectrometer [97]. Since the molecular beam is co-axial with the axis of the cavity, each line is split into two Doppler components, and the rest frequency is the mean of these two components.
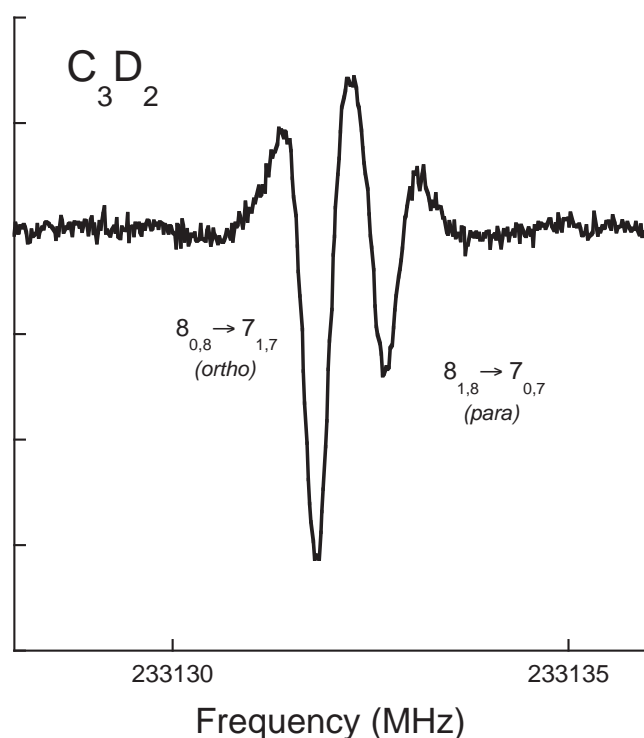
FIGURE 5.3: *Ortho/para* doublet of *c*-C_3D_2 observed near 233 GHz [97]. The distinctive 2:1 *ortho/para* intensity ratio has guided the initial search for *c*-C_3D_2 in the millimeter-wave band.

5.1.4 Doubly deuterated cyclopropenylidene in space

Unlike several of the six known multiply deuterated species observed in the radio band (D_2H^+, CHD_2OH, NHD_2, D_2CO, D_2S, and D_2CS), *c*-C_3H_2 is believed to form solely by gas phase reactions [95]. The interplay between the gas phase and grain surface reactions in the deuteration of interstellar molecules is not clear so far, partially because there are not many probes available for testing the models. *c*-C_3H_2 is an ideal molecule for this purpose because it is abundant and widespread, and it has the possibility of double deuteration. If also *c*-C_3D_2 is formed in the gas-phase like its fully hydrogenated counterpart, cyclopropenylidene will be a unique probe for the deuteration processes happening in the gas-phase. Furthermore, since *c*-C_3H_2 is, in terms of cloud evolution, an "early-type" molecule [108], it is a particular useful tool to investigate early stages of a molecular cloud. This

makes observations of its deuterated forms particularly important to test time-dependent chemical codes which include deuteration processes.

In the course of this thesis, I detected the doubly deuterated cyclopropenylidene toward the starless cores TMC-1C and L1544 using the IRAM 30m telescope. The $J_{K_a,K_c} = 3_{0,3} - 2_{1,2}$, $3_{1,3} - 2_{0,2}$, and $2_{2,1} - 1_{1,0}$ transitions of this species have been observed at 3 mm in both sources. The expected 1:2 intensity ratio has been found in the $3_{0,3}$ - $2_{1,2}$ and $3_{1,3}$ - $2_{0,2}$ lines, belonging to the *para* and *ortho* species respectively. I also observed lines of the main species, c-C$_3$H$_2$, the singly deuterated c-C$_3$HD, and the species with one ^{13}C off of the principal axis of the molecule, c-H^{13}CC$_2$H. The lines of c-C$_3$D$_2$ have been observed with high signal to noise ratio, better than 7.5σ in TMC-1C and 9σ in L1544.

5.2 Observations

The observations have been carried out from 2012 September 28 until October 2 at the IRAM 30 m telescope, located in Pico Veleta (Spain), towards the starless cores TMC-1C and L1544. The choice of the sources has been made on the basis of two simple criteria: the abundance of the normal species (c-C$_3$H$_2$) and a high deuterium fractionation. Both sources are in the Taurus Molecular Cloud, one of the closest dark cloud systems and low-mass star forming regions in our Galaxy. L1544 is a perfect test bed to investigate the initial conditions of protostellar collapse. Its structure is consistent with a contracting Bonnor-Ebert sphere, with central densities of about 10^7 cm^{-3} and a peak infall velocity of ~ 0.1 km s^{-1} at about 1000 AU from the center [109]. Its centrally concentrated structure and measured kinematics suggests that this is a pre-stellar core at a late stage of evolution, toward star formation. TMC-1C is a relatively young core, with evidence of accreting material towards a core and immersed in a cloud with densities higher than those surrounding the L1544 core [110].

The coordinates that were used are $\alpha_{2000} = 04^h41^m16^s.1$ $\delta_{2000} = +25°49'43''.8$ for TMC-1C, and $\alpha_{2000} = 05^h04^m17^s.21$ $\delta_{2000} = 25°10'42''.8$ for L1544. In the case of TMC-1C these are the same coordinates as reported by Bell et al. (1988) [111] and Gerin et al. (1987) [105], while in the case of L1544 they correspond to the coordinates of the peak of the 1.3 mm continuum dust emission from Ward-Thompson et al. (1999) [112]. In both cores I observed two lines of c-C$_3$H$_2$, one line of

c-H^{13}CC$_2$H (off axis), two lines of *c*-C$_3$HD and three lines of *c*-C$_3$D$_2$, using three different tuning settings. In Figure 5.4 the different tuning settings used during the observations are shown. With the setup 1 I observed the lines of the normal species, the ^{13}C isotopologue and the line of *c*-C$_3$HD at 104 GHz. While with setup 2 I observed the three lines of *c*-C$_3$D$_2$, and with set-up 3 I have observed the line of *c*-C$_3$HD at 95.9 GHz. A summary of the observed lines is reported in Table 5.1. The EMIR[*] receivers in the E090 configuration were employed, and observations were performed in a frequency switching mode with a throw of ± 4.3 MHz. All four EMIR sub-bands were connected to the Fourier Transform Spectrometer (FTS) set to high resolution mode; this delivered a final spectrum with 50 kHz channel spacing (corresponding to 0.15 km s^{-1} at 3 mm) and a total of 7.2 GHz of spectral coverage (nominal bandpass of 1.8 GHz per sub-band). The telescope pointing was checked every two hours on Jupiter and was found to be accurate to 3-4 arcsec.

TABLE 5.1: Molecular line transitions of isotopologues of cyclopropenylidene observed in TMC-1C and L1544

Molecule	Transition ($J_{K_a K_c}$)	Frequency (GHz)
c-C$_3$H$_2$	$2_{12} - 1_{01}$	85.338
	$2_{12} - 1_{01}$	85.338
	$3_{22} - 3_{13}$	84.727
c-H^{13}CC$_2$H	$2_{12} - 1_{01}$	84.185
c-C$_3$HD	$2_{11} - 1_{10}$	95.994
	$3_{03} - 2_{12}$	104.187
c-C$_3$D$_2$	$3_{03} - 2_{12}$	94.371
	$3_{13} - 2_{02}$	97.761
	$2_{21} - 1_{10}$	108.654

[*]EMIR is one of the heterodyne receivers in use at the 30 m telescope. Its E090 band covers the 83-117 GHz frequency range. http://www.iram.es/IRAMES/mainWiki/EmirforAstronomers
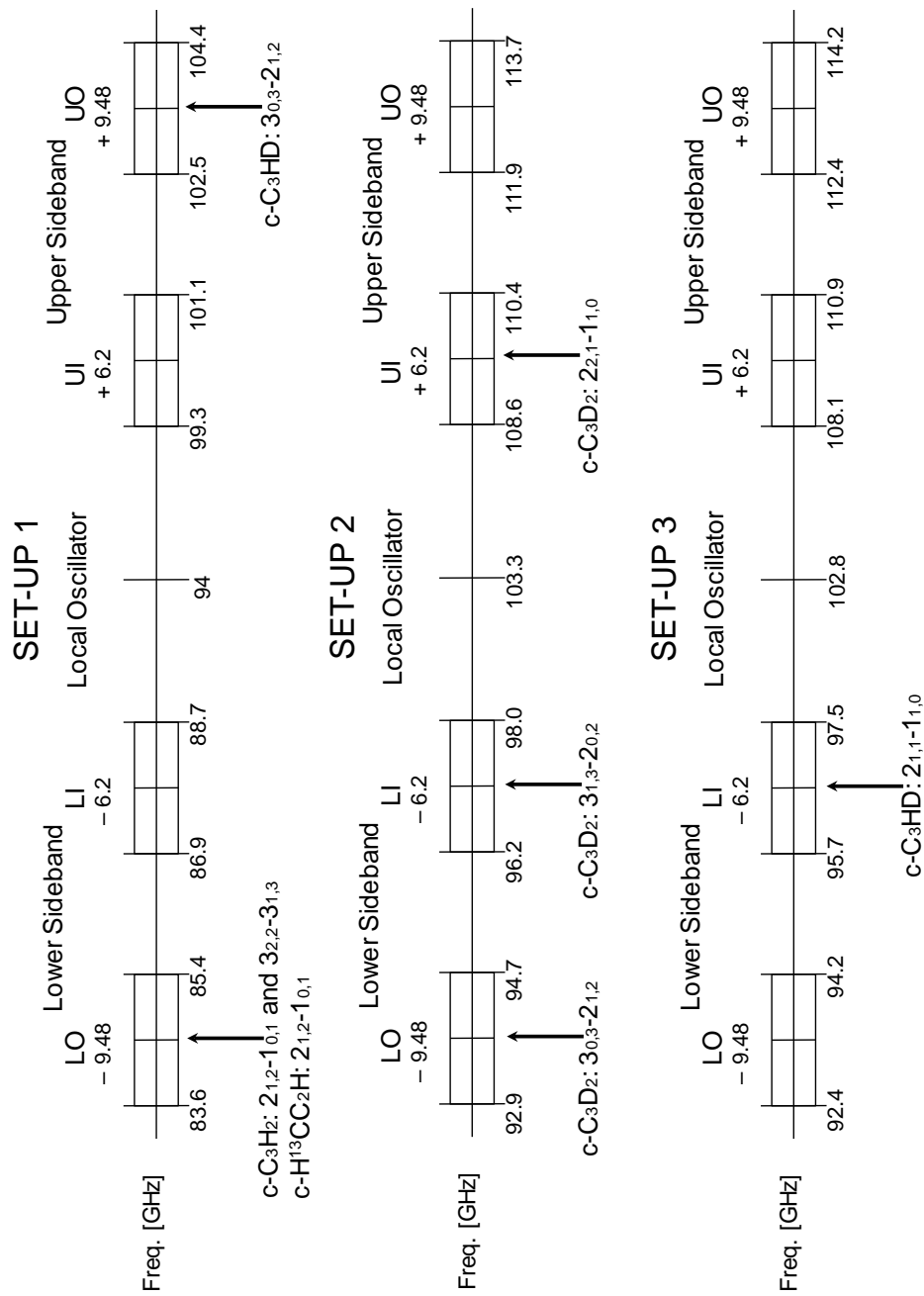
FIGURE 5.4: Three different tuning settings used during the observations. When using the FTS spectrometer with high resolution (50 kHz), just the central 1.8 GHz of every sub-band is available. The total frequency coverage per tuning setting was 7.2 GHz.

5.3   Results

Lines of the isotopologues of *c*-C$_3$H$_2$ listed in Table 5.1 have been detected in both
sources with very high signal-to-noise ratio. The spectra of *c*-C$_3$H$_2$ and isotopo-
logues in TMC-1C and L1544 are shown in Figure 5.5 and Figure 5.6 respectively.
Table 5.2 lists the observed line parameters. Even the weakest line of the doubly
deuterated species, 2_{21} - 1_{10} at 108 GHz, is detected at a 7.5σ level in TMC-1C
(T$_{mb,rms}$ = 2.5 mK), and at a 9σ level in L1544 (T$_{mb,rms}$ = 4.6 mK). The GILDAS[†]
software [113] was employed for the data processing. High order polynomials had
to be used for baseline subtraction given the strong baseline produced by the fre-
quency switching observing mode. The column densities and optical depths given
in Table 5.2 were calculated using the expressions given in the next section. As
it was already pointed out by Bell et al. (1988) [111], *c*-C$_3$H$_2$ shows two velocity
components towards TMC-1C, one more intense at 6 km s^{-1} and one less intense
at 5.4 km s^{-1}, see Figure 5.5. There is a hint of detection of the component at
5.4 km s^{-1} also in c-H^{13}CC$_2$H, but no clear presence in the deuterated species.
Assuming that all lines have the same excitation temperature in both compo-
nents, one expects for the component at 5.4 km s^{-1} a line intensity of 0.06 K for
c-C$_3$HD (3_{03} - 2_{12}) and 0.013 K for *c*-C$_3$D$_2$ (3_{13} - 2_{02}). Comparing these estimates
with the noise level in the observed spectra (0.007 K for *c*-C$_3$HD and 0.002 K for
c-C$_3$D$_2$) I can say that the lower velocity component is absent in the deuterated
species of cyclopropenylidene: this behavior may suggest that the lower velocity
component traces a hotter region, where the deuterated molecules are not present
in detectable amounts.

[†]http://www.iram.fr/IRAMFR/GILDAS
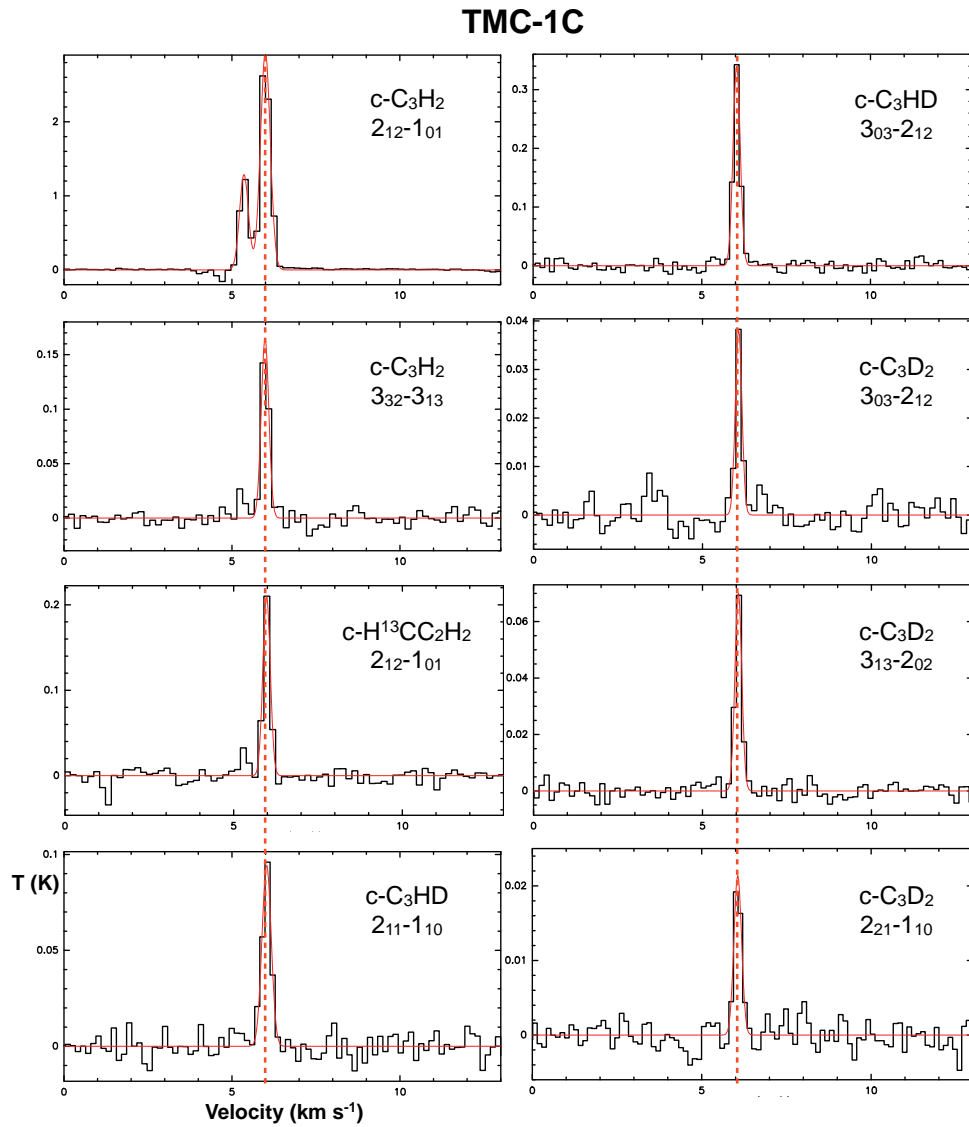
TMC-1C

FIGURE 5.5: Spectra of all isotopic species of c-C_3H_2 observed towards the starless core TMC-1C
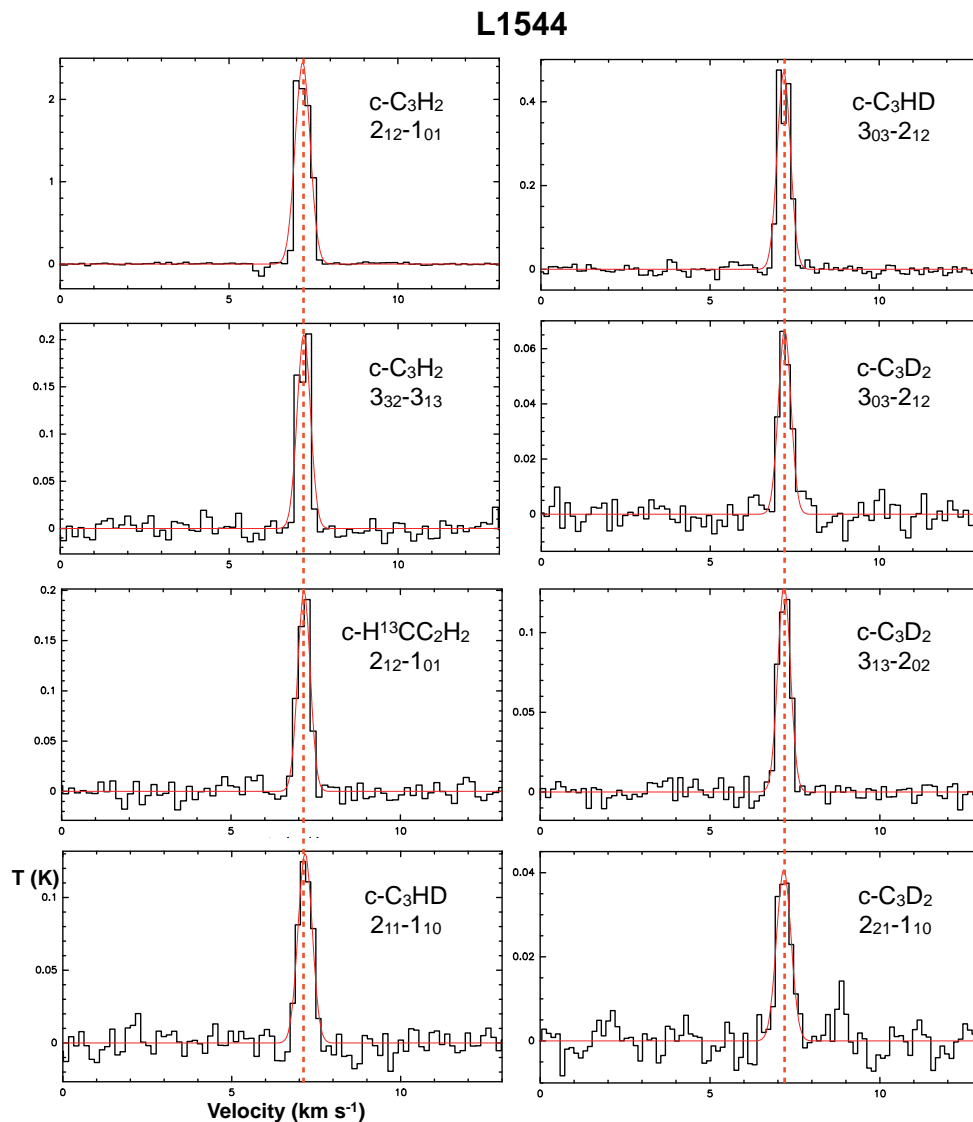
FIGURE 5.6: Spectra of all isotopic species of c-C_3H_2 observed towards the starless core L1544

5.3.1   Column density and optical depth

The column densities and optical depths given in Table 5.2 were calculated using the following expressions. The line center opacity τ_0 is

$$\tau_0 = \ln\left(\frac{J(T_{ex}) - J(T_{bg})}{J(T_{ex}) - J(T_{bg}) - T_{mb}}\right) \tag{5.1}$$

where $J(T) = \frac{h\nu}{k}(e^{\frac{h\nu}{kT}} - 1)^{-1}$ is the source function in Kelvin. The upper state column density in case of optically thin emission, and the total column density are defined as:

$$N_{up}^{thin} = \frac{8\pi\nu^3\sqrt{\pi}\Delta\nu\tau_0}{c^3 A_{ul} 2\sqrt{\ln 2}(e^{\frac{h\nu}{kT}} - 1)} \tag{5.2}$$

$$N_{tot} = \frac{N_u Q_{rot}(T_{ex})}{g_u} e^{(\frac{E_u}{kT_{ex}})} \tag{5.3}$$

where k is the Boltzmann constant, ν is the frequency of the line, h is the Planck constant, c is the speed of light, A_{ul} is the Einstein coefficient of the transition, $\Delta\nu$ is the full width at half maximum, g_u is the degeneracy of the upper state defined as the nuclear spin statistical weight (see Table 2.1) times the spin rotation degeneracy $2J+1$, E_u is the energy of the upper state, Q_{rot} is the partition function of the molecule at the given temperature T_{ex}. T_{ex}, T_{bg}, T_{mb} are the excitation, the background (2.7 K) and the main beam temperatures respectively, in K. To calculate N_{tot} and τ we assumed a T_{ex} of 7 K for TMC-1C and 5 K for L1544 for all deuterated isotopologues, following the paper from Gerin and coworkers [105], and 8 K for TMC-1C and 6 K for L1544 for the main species and the ^{13}C isotopologues as they trace also warmer regions of the cloud. The effect of the excitation temperature on the derived column density ratios in Table 5.3 was found to be small, with a change of few percent upon a variation of ±1 K. By using these expressions we assumed that the source fills the beam, and optically thin emission obeying Local Thermodynamic Equilibrium (LTE). Since lines of *c*-C$_3$H$_2$ are optically thick, we derived its total column density from the total column density of *c*-H^{13}CC$_2$H assuming a ^{12}C/^{13}C ratio of 77, determined by Wilson & Rood (1994) [114] from H$_2$CO and CO as a function of distance from the Galactic Center. N_u and τ for *c*-C$_3$H$_2$ were derived from N_{tot}.

TABLE 5.2: Observed line parameters in TMC-1C and L1544

Molecule	Transition (ortho/para)	Frequency (GHz)	Ref.	E_{up} (cm^{-1})	T_{mb} (K)	rms mK	W (K km s^{-1})	B_{eff} %	θ_{MB} (arcsec)	V_{LSR} (km s^{-1})	δV (km s^{-1})	N_u^a ($\times 10^{11}$ cm^{-2})	$N_{tot}^{b,c}$ ($\times 10^{12}$ cm^{-2})	τ^c
TMC-1C														
c-C_3H_2	$2_{12} - 1_{01}$ (o)	85.338	[100]	4.48	2.91	7	1.05(1)	81	29	5.996(2)	0.338(4)	25(1)	22(1)	1.887
	$2_{12} - 1_{01}$ (o)	85.338	[100]	4.48	1.27	7	0.414(9)	81	29	5.361(4)	0.307(8)			
	$3_{22} - 3_{13}$ (p)	84.727	[100]	11.21	0.16	7	0.047(2)	81	29	5.984(6)	0.27(2)	3.5(2)	22(1)	0.148
c-H^{13}CC$_2$H	$2_{12} - 1_{01}$	84.185	[115]	4.40	0.22	7	0.060(3)	81	29	5.977(7)	0.26(1)	0.52(2)	0.62(3)	0.056
c-C_3HD	$2_{11} - 1_{10}$	95.994	[115]	5.25	0.1	7	0.033(2)	80	27	6.03(1)	0.33(3)	1.8(1)	2.8(2)	0.026
	$3_{03} - 2_{12}$	104.187	[115]	7.54	0.34	7	0.091(2)	79	25	6.034(3)	0.250(6)	0.63(1)	1.1(3)	0.092
c-C_3D_2	$3_{03} - 2_{12}$ (p)	94.371	[97]	6.84	0.04	2	0.009(1)	80	27	6.07(1)	0.23(2)	0.063(5)	0.17(1)	0.010
	$3_{13} - 2_{02}$ (o)	97.761	[97]	6.87	0.07	2	0.017(1)	80	26	6.062(5)	0.233(9)	0.11(4)	0.15(6)	0.018
	$2_{21} - 1_{10}$ (p)	108.654	[97]	5.49	0.02	2	0.006(1)	78	24	6.06(1)	0.25(3)	0.032(4)	0.09(1)	0.005
L1544														
c-C_3H_2	$2_{12} - 1_{01}$ (o)	85.338	[100]	4.48	2.44	10	1.35(1)	81	29	7.180(2)	0.520(4)	50(2)	37(1)	3.579
	$3_{22} - 3_{13}$ (p)	84.727	[100]	11.21	0.21	10	0.10(1)	81	29	7.210(8)	0.46(1)	4.7(2)	37(1)	0.172
c-H^{13}CC$_2$H	$2_{12} - 1_{01}$	84.185	[115]	4.40	0.19	10	0.093(3)	81	29	7.154(8)	0.44(2)	0.92(4)	0.96(4)	0.096
c-C_3HD	$2_{11} - 1_{10}$	95.994	[115]	5.25	0.13	10	0.065(3)	80	27	7.17(1)	0.48(3)	4.1(2)	6.2(3)	0.066
	$3_{03} - 2_{12}$	104.187	[115]	7.54	0.48	10	0.238(4)	79	25	7.181(4)	0.468(9)	2.1(4)	4.5(9)	0.278
c-C_3D_2	$3_{03} - 2_{12}$ (p)	94.371	[97]	6.84	0.07	5	0.032(2)	80	27	7.20(1)	0.45(3)	0.26(2)	0.77(5)	0.035
	$3_{13} - 2_{02}$ (o)	97.761	[97]	6.87	0.13	5	0.059(2)	80	26	7.181(7)	0.43(2)	0.44(2)	0.66(2)	0.067
	$2_{21} - 1_{10}$ (p)	108.654	[97]	5.49	0.04	5	0.023(2)	78	24	7.17(2)	0.54(5)	0.16(1)	0.45(4)	0.020

[a] All N_u have been calculated with the optical thin assumption, except for c-C_3H_2

[b] Local thermodynamic equilibrium is assumed

[c] T_{ex} assumed is 5 K in L1544, and 7 K in TMC-1C for the deuterated species, and 6 K in L1544 and 8 K in TMC-1C for the ^{13}C and the main species

5.4   Discussion

In addition to the observation of two lines of c-C_3H_2, one line of c-$H^{13}CC_2H$ (with the ^{13}C not on the molecular axis), two lines of c-C_3HD, and three lines of c-C_3D_2 were also detected in both TMC-1C and L1544. This first interstellar detection of c-C_3D_2 is validated by the following reasons:

- We detected all favorable transitions of c-C_3D_2 available in the covered frequency range.

- The rest frequencies employed have laboratory accuracy [97], and in both sources the line shapes and velocities are in agreement with each other and with those observed for more abundant isotopologues (see Figure 5.5 and Figure 5.6).

- The intensities of the c-C_3D_2 lines are consistent with what is expected from the deuteration of the ring in these sources, i.e. c-C_3H_2/c-C_3HD is consistent with c-C_3HD/c-C_3D_2, as will be discussed below.

In Table 5.3 the relative abundances of the deuterated species are presented with respect to the hydrogenated ones for cyclopropenylidene over the 27″ beam for TMC-1C and L1544 obtained from this work, and also for H_2CO, HCO^+, N_2H^+ and NH_3 obtained from previous works. The abundance of doubly deuterated cyclopropenylidene with respect to the normal species is (0.4 - 0.8)% in TMC-1C and (1.2 - 2.1)% in L1544. This interval has been determined considering the differences in N_{tot} obtained from different lines. The deuteration of c-C_3H_2 follows the same trend observed for other molecules in both sources. It is interesting to note that the ratios [c-C_3D_2]/[c-C_3HD] and [c-C_3HD]/[c-C_3H_2] are quite similar in both sources. The D/H ratio of c-C_3H_2 in prestellar cores has been calculated using the network model of Aikawa [116]. For the physical structure of the core two different models have been adopted, the collapsing core model from a previous work by Aikawa [76] (the α=1.1 model), and the static model of L1544 from Keto and Caselli [109]. For CO depletion factors consistent with those of the two objects, i.e. $f_D = 3.8$ for TMC-1C [110] and $f_D = 14$ for L1544 [117], the calculated column density ratio of c-C_3D_2/c-C_3H_2 is $\sim 10^{-2}$, consistent with the observed value of 0.6% for TMC-1C and 1.5% for L1544. There is no need for any deuterium fractionation reactions of c-C_3H_2 on grain surfaces to account for

the observed D/H ratio: the deuteration of cyclopropenylidene can be explained solely by gas-phase reactions.

TABLE 5.3: Abundance ratios of deuterated molecules in TMC-1C and L1544

	TMC-1C	L1544
[c-C$_3$D$_2$]/[c-C$_3$H$_2$]	(0.4 - 0.8)%	(1.2 - 2.1)%
[c-C$_3$D$_2$]/[c-C$_3$HD]	(3 - 15)%	(7- 17)%
[c-C$_3$HD]/[c-C$_3$H$_2$]	(5 - 13)%	(12 - 17)%
[D$_2$CO]/[H$_2$CO]	-	4%[a]
[DCO$^+$]/[HCO$^+$]	2%[b]	4%[c]
[N$_2$D$^+$]/[N$_2$H$^+$]	8%[b]	20%[c]
[NH$_2$D]/[NH$_3$]	1%[b]	13%[d]

[a][118], [b][119], [c][68], [d][120]

5.4.1 Modeling the observed abundances with MAPLE

In order to define which reactions, among the ones included in the Aikawa model [116], constitute the main formation route for *c*-C$_3$D$_2$, I created a toy model with Maple[‡]. A small set of reactions, shown in Figure 5.7, and reaction rate equations are included in the model. This model reproduces quite well the observed abundances. In the model it is assumed that the overall process of formation of *c*-C$_3$D$_2$ is divided in two steps. The first step consists of the protonation/deuteration of *c*-C$_3$H$_2$ after reactions with H$_3^+$ and deuterated isotopologues. The second step is the dissociative recombination with electrons of the ion produced in the first step. The deuterated isotopologues of H$_3^+$ are formed by the reaction of H$_3^+$ with HD, the reservoir of deuterium in interstellar clouds. This is the key reaction for the formation of deuterated molecules in the cold interstellar medium. It is exothermic by 220 K [121] and this prevents back reactions at temperatures as low as 10 K. Given the high abundance of H$_3^+$ and its fast deuteration, in the toy model I assume to have an infinite reservoir of H$_3^+$, H$_2$D$^+$, D$_2$H$^+$, and D$_3^+$. I also assume $\frac{H_3^+}{H_2D^+} \simeq \frac{H_2D^+}{D_2H^+} \simeq \frac{D_2H^+}{D_3^+} \simeq 1$. At first approximation, this is a reasonable assumption, see Caselli et al. (2008) [122], even if these ratios vary with time and density, and strongly depend on the CO depletion on grains. I also assume the reactions of the different isotopologues of *c*-C$_3$H$_2$ with H$_3^+$, H$_2$D$^+$, D$_2$H$^+$, and D$_3^+$ to proceed with the same velocity. The rate for the reaction of *c*-C$_3$H$_2$ with

---

[‡]Maple is a mathematical and analytical software developed and distributed by Maplesoft

H$_3^+$ is $k \simeq 5\times 10^{-8}$ cm^3 s^{-1} (from the KIDA catalog[§]). Finally, I assume the dissociative recombination of the ions with the electrons, the last step, to be the fastest. Hence the bottleneck of the whole process is the protonation/deuteration of c-C$_3$H$_2$ and isotopologues. By considering that these reactions proceed statistically, a set of matrices is developed to consider all the possibilities to form (and destroy) first the ions (c-C$_3$H$_3^+$, c-C$_3$H$_2$D$^+$, c-C$_3$D$_2$H$^+$, and c-C$_3$D$_3^+$), and then, after a dissociative recombination with electrons, to form c-C$_3$H$_2$, c-C$_3$HD, and c-C$_3$D$_2$. The whole model is given in Appendix A. The results from this model are shown in Figure 5.9 and Figure 5.10. The overall timescale of the process τ is given by the proton/deuteron transfer, as it is the slowest step, so $\frac{1}{\tau} = k[H_3^+]$. By considering $[\text{H}_3^+] \simeq 10^{-4}$ cm^{-3} [123] and $k \simeq 5\times 10^{-8}$ cm^3 s^{-1}, then $\tau \approx 10^5$ years. In Figure 5.9 is shown how the abundance of c-C$_3$H$_2$, c-C$_3$HD, and c-C$_3$D$_2$ vary with time within the model. At the beginning only the fully hydrogenated isotopologue is assumed to be present. As the deuteration reactions proceed, the deuterated isotopologues are formed up to a steady state after 10^6 years. The time t in the model is expressed as t/τ, and we assume that the time constant of the process, τ, is defined solely by the rate of protonation/deuteration of either c-C$_3$H$_2$, c-C$_3$HD, or c-C$_3$D$_2$. In order to obtain the time, one has to multiply the x value (t/τ) by $\tau \approx 10^5$ years. In Figure 5.10 is shown how the ratios c-C$_3$HD/c-C$_3$H$_2$ and c-C$_3$D$_2$/c-C$_3$H$_2$ develop in time within the model. The ratios derived from the observations correspond to timescales comparable to the age of prestellar cores, around 10^4 years. The contribution from other deuteration processes, e.g. the formation of c-C$_3$HD from the reaction of C$_3$H$^+$ with HD, were found to be negligible within this model. The D/H ratio of cyclopropenylidene is, therefore, directly related to that of H$_3^+$, the main deuterium donor in dark interstellar clouds, and may be used as a chemical clock.

The main route of formation of deuterated cyclopropenylidene that I propose is the successive deuteration of the main species via reactions with H$_2$D$^+$, D$_2$H$^+$, and D$_3^+$. An example of the reaction scheme is sketched in Figure 5.8, considering only H$_2$D$^+$ as reaction partner. The depicted cycle of reactions starts with c-C$_3$H$_2$ and H$_2$D$^+$, producing in the first step c-C$_3$HD and subsequently c-C$_3$D$_2$. The same reactions happen with H$_3^+$, D$_2$H$^+$ and D$_3^+$. The overall process is a series of two reactions: the proton-deuteron transfer (slow step, red arrows), and the subsequent dissociative recombination with electrons (fast step, blue arrows). Doubly deuterated cyclopropenylidene appears to be a very interesting probe for

---

[§]http://kida.obs.u-bordeaux1.fr/

the earliest stages of star formation. Its formation mechanism puts important constraints on gas-phase deuteration models, and suggests the possibility of using *c*-C_3D_2 as a chemical clock since the presence of this deuteration cycle results in a time dependent deuterium fractionation. Assuming low levels of deuteration at the start, it is expected that this level increases as a function of time, reaching a stationary level after some time.

$$H_3^+ + HD \longrightarrow H_2D^+ + H_2$$
$$H_2D^+ + HD \longrightarrow D_2H^+ + H_2$$
$$D_2H^+ + HD \longrightarrow D_3^+ + H_2$$

$$C_3H_2 + H_3^+ \longrightarrow C_3H_3^+$$
$$C_3H_2 + H_2D^+ \longrightarrow C_3H_3^+ \text{ or } C_3H_2D^+$$
$$C_3H_2 + D_2H^+ \longrightarrow C_3H_3^+ \text{ or } C_3H_2D^+$$
$$C_3H_2 + D_3^+ \longrightarrow C_3H_2D^+$$

$$C_3HD + H_3^+ \longrightarrow C_3H_2D^+$$
$$C_3HD + H_2D^+ \longrightarrow C_3H_2D^+ \text{ or } C_3D_2H^+$$
$$C_3HD + D_2H^+ \longrightarrow C_3H_2D^+ \text{ or } C_3D_2H^+$$
$$C_3HD + D_3^+ \longrightarrow C_3D_2H^+$$

$$C_3D_2 + H_3^+ \longrightarrow C_3D_2H^+$$
$$C_3D_2 + H_2D^+ \longrightarrow C_3D_2H^+ \text{ or } C_3H_2D^+$$
$$C_3D_2 + D_2H^+ \longrightarrow C_3D_2H^+ \text{ or } C_3H_2D^+$$
$$C_3D_2 + D_3^+ \longrightarrow C_3D_3^+$$

$$C_3H_3^+ + e^- \longrightarrow C_3H_2$$
$$C_3H_2D^+ + e^- \longrightarrow C_3H_2 \text{ or } C_3HD$$
$$C_3D_2H^+ + e^- \longrightarrow C_3HD \text{ or } C_3D_2$$
$$C_3D_3^+ + e^- \longrightarrow C_3D_2$$
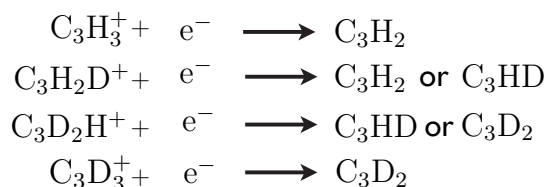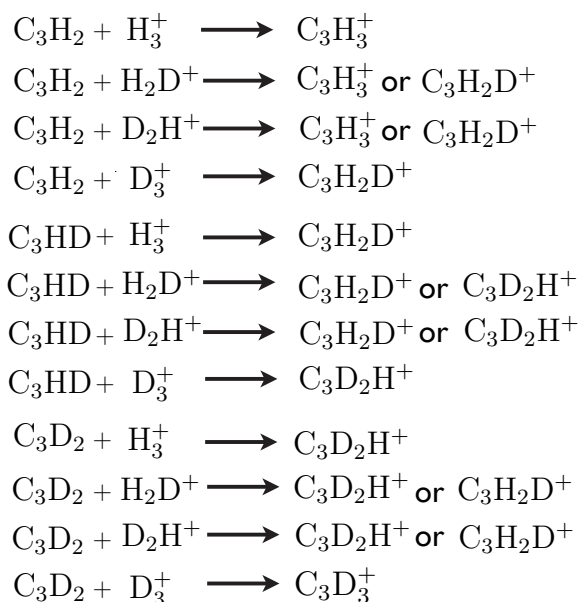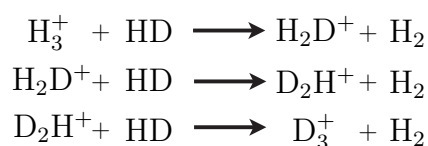
FIGURE 5.7: Set of reactions included in the Maple model
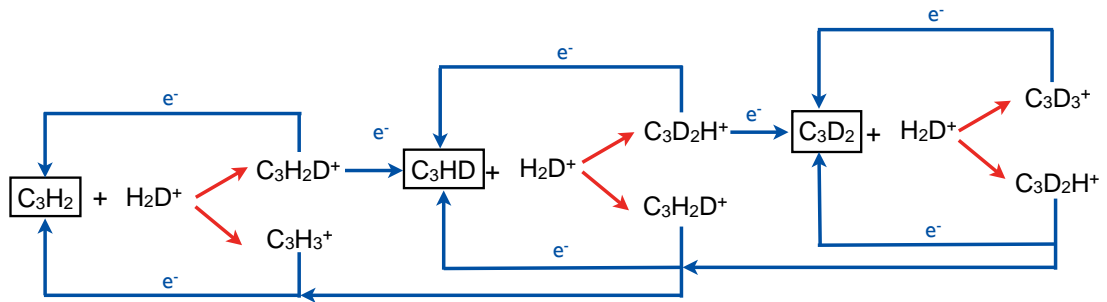
FIGURE 5.8: Mechanism of formation of c-C_3D_2: a cycle of proton/deuteron transfer and dissociative recombination with electrons
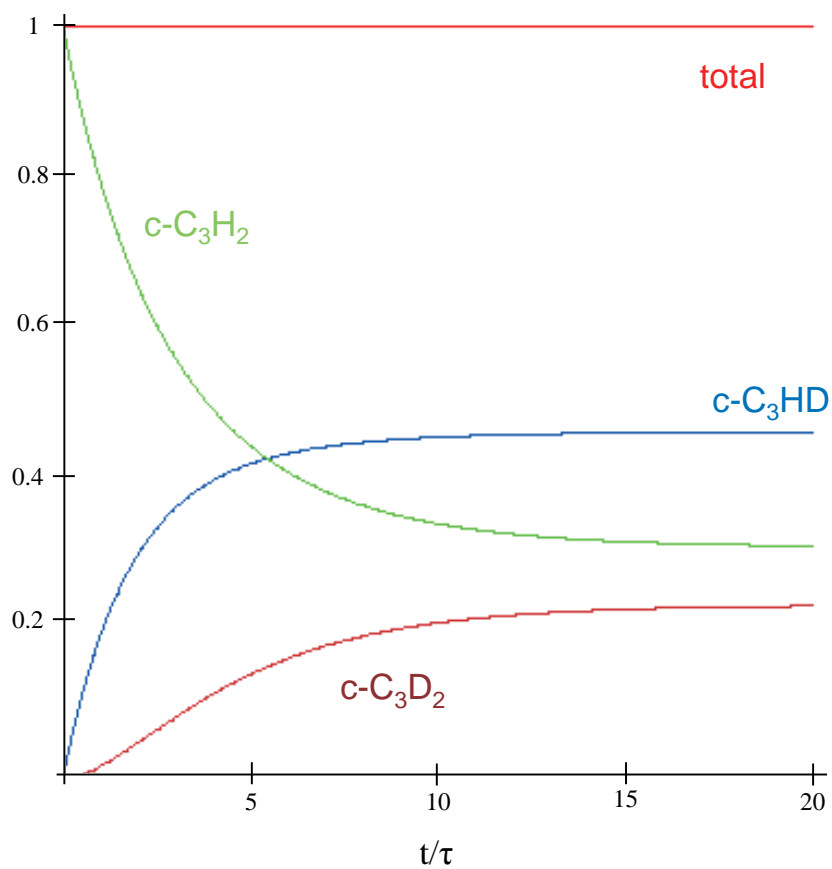
FIGURE 5.9: Results of the MAPLE model: the abundances of c-C_3H_2 and deuterated isotopologues, whose sum is normalized to one, are plotted against time. Time is defined as the time constant of the process τ, which depends on the abundance of H_3^+, so $\tau \approx 10^5$ years
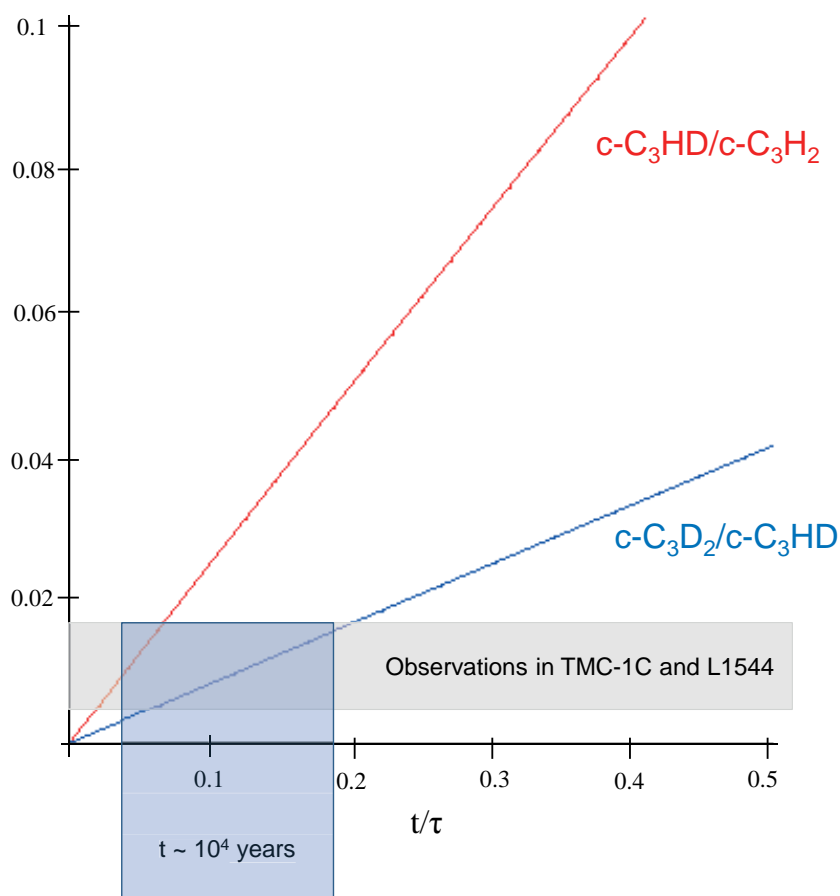
FIGURE 5.10: Results of the MAPLE model: the abundances of the deuterated isotopologues with respect to the fully hydrogenated c-C$_3$H$_2$ are plotted against time, where time is defined as the time constant of the process τ, which depends on the abundance of H$_3^+$, so $\tau \approx 10^5$ years

5.4.2 Perspectives

Recently Huang and Lee [124] have calculated highly accurate spectroscopic constants for ^{13}C and D isotopologues of c-C$_3$H$_3^+$ in order to guide the laboratory and astronomical search. Since these species are intermediates in the formation of isotopic species of c-C$_3$H$_2$, their detection would be useful to put more constraints on the models.

During a recent observation run at the IRAM 30 m telescope (beginning of October 2013), the lines of c-C$_3$H$_2$, c-H^{13}CC$_2$H$_2$, c-C$_3$HD, and c-C$_3$D$_2$ have been mapped toward L1544. The preliminary results are presented in Figure 5.11. The maps cover an area of 10 arcmin^2. The coordinates of L1544 for the center of the

map are the same used for the first detection of c-C_3D_2, $\alpha_{2000} = 05^h04^m17^s.21$ $\delta_{2000} = 25°10'42''.8$.
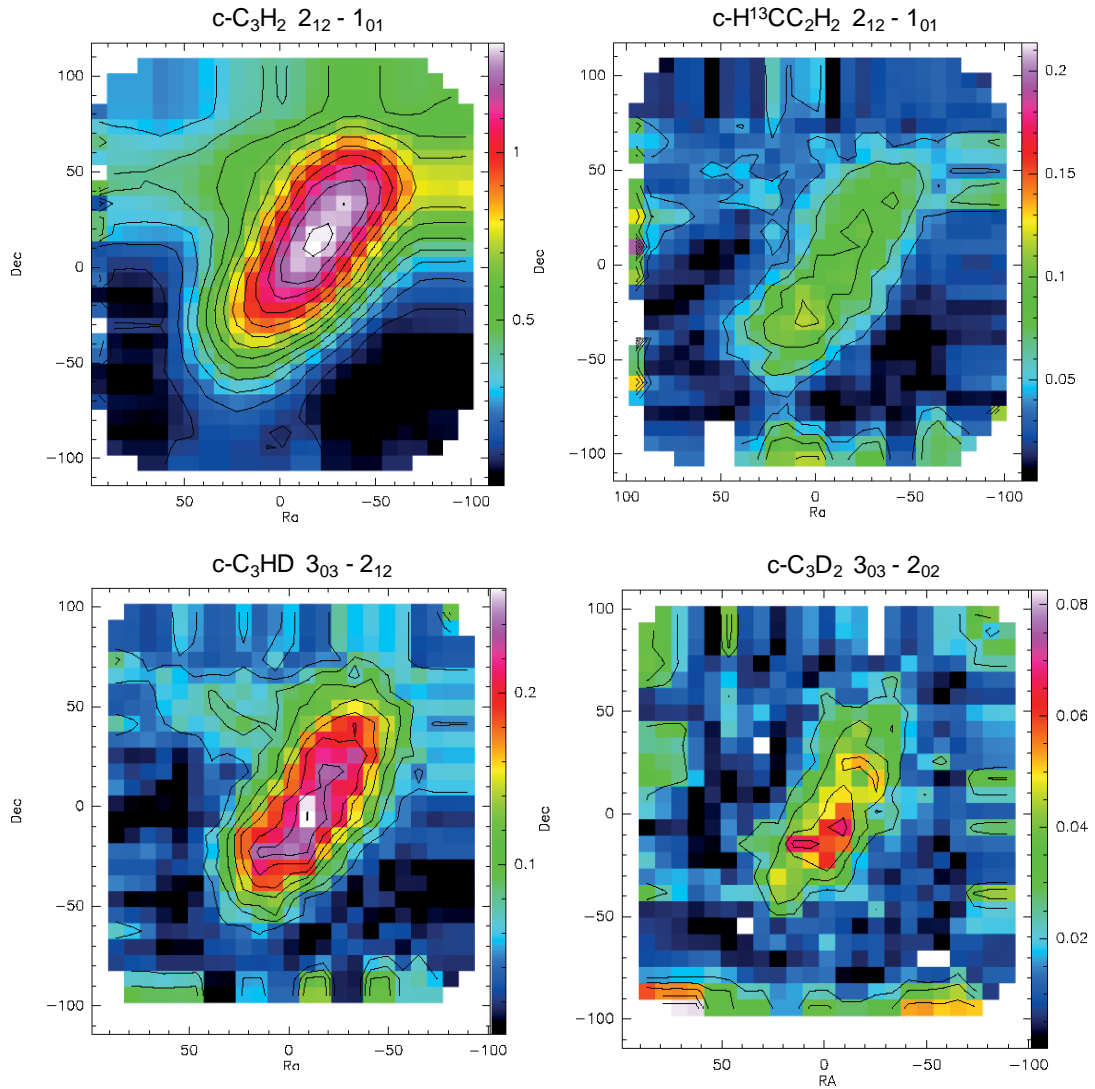
FIGURE 5.11: Preliminary reduction of the maps of cyclopropenylidene and isotopologues toward L1544 observed with the 30 m telescope in an observing run in the beginning of October 2013. The Ra and Dec, right ascension and declination, are expressed in arcseconds. The intensity scale of the maps is in Kelvin.

This results is important to unveil the deuterium fractionation processes in the gas phase of a carbon-bearing species, and compare them to the well-known deuteration of N_2H^+, already mapped in the region [68].

The maps clearly show that the deuterated isotopologues, c-C_3HD and even more c-C_3D_2, are concentrated in the center of the cloud and are co-spatial. Detailed

maps of the morphology of the deuteration will allow to better constrain current chemical models and to unveil possible differences between carbon-bearing and nitrogen-bearing species deuteration. Cyclopropenylidene, being a carbon chain molecule, is more abundant in regions where carbon is not mostly locked in CO and it is expected to trace material further out from the center compared to N_2H^+.

Chapter 6

Tentative Detection of l-C$_3$HD

6.1 Introduction

As shown in the previous chapter, in September 2012 I have observed for the first time c-C$_3$D$_2$ in the starless cores TMC-1C and L1544 with the IRAM 30 m telescope. The broad coverage of the Fourier Transform Spectrometer (FTS) resulted in a very wide frequency coverage of both sources ranging from 84 GHz up to 114 GHz. Two lines of the less abundant linear isomer, l-C$_3$H$_2$, and possibly one line of its singly deuterated isotopologue l-C$_3$HD have also been observed toward TMC-1C. If confirmed, this will be the first interstellar detection of l-C$_3$HD. Propadienylidene, l-C$_3$H$_2$, is a very polar carbene, and the less stable isomer (~ 10 kcal mol^{-1} [125]) of the astronomically widely distributed cyclopropenylidene. The structures of the two isomers are reported in Figure 6.1. Propadienylidene is usually not as widespread as its cyclic isomer. After its first detection in the laboratory [126], it was detected in TMC-1, in IRC+10216 [127, 128], and in few other galactic sources [129, 130].

6.1.1 Linear C$_3$H$_2$ in the laboratory

Vrtilek and coworkers succeeded in producing and characterizing linear C$_3$H$_2$ in the laboratory for the first time [126]. Propadienylidene was produced by discharging acetylene and carbon monoxide in helium, in approximate molar ratios of 70:20:1. The discharge current used was quite high, half an Ampere, and the

81
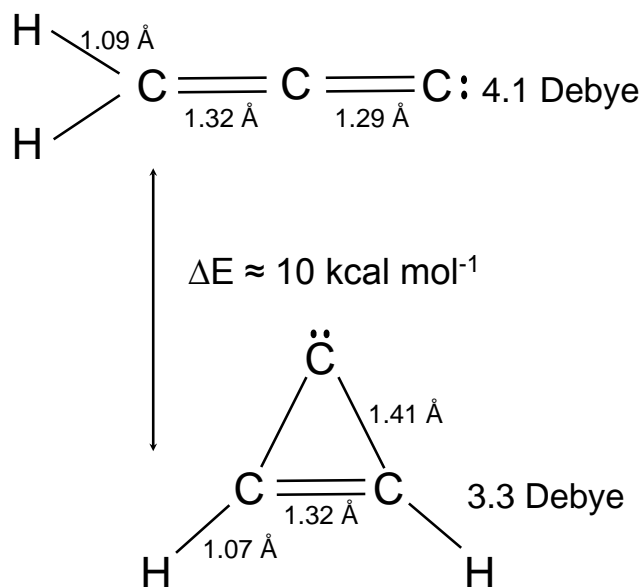
FIGURE 6.1: Molecular geometries of the linear and cyclic C$_3$H$_2$. The double dots indicate the two characteristic carbene electrons not involved in a bond

temperature of the cell was kept at 160 K during the measurements. The laboratory search was based on ab initio structures [131, 132]. In total, 54 millimeter- and submillimeter-wave lines have been measured, with frequencies ranging from 145 up to 370 GHz.

6.1.2   Linear C$_3$H$_2$ in space

Linear C$_3$H$_2$ was detected in space shortly after its first detection in the laboratory. Three lines have been observed toward TMC-1 showing a rotational temperature around 6 K, and two lines have been observed toward IRC+10216 showing a rotational temperature of 25 K [127]. In the observed position in TMC-1, Cernicharo and coworkers determined the linear isomer to have a column density 70 times lower than the cyclic one. Subsequently propadienylidene has been observed in absorption toward the continuum emission of W51E1/E2, W51D, and W49 [133]. In these sources, the abundance ratio between the cyclic and the linear isomer is one order of magnitude lower than toward TMC-1. The precursors of linear and cyclic C$_3$H$_2$ are the linear and cyclic C$_3$H$_3^+$. They are believed to be formed at the same rate [134]. The dissociative recombination (DR) of *c*-C$_3$H$_3^+$ has been calculated to be more efficient than the DR of *l*-C$_3$H$_3^+$ [135], leading to

a cyclic-to-linear ratio bigger than one. The difference in abundance of the linear and cyclic isomer can also originate from different destruction processes, more efficient for the linear isomer than from the cyclic one. The proposed mechanisms to explain the observational results so far are:

- More destruction mechanisms are available for the linear C$_3$H$_2$ compared to the cyclic. The cyclic is, for example, inert to neutral-neutral reaction [134].

- *l*-C$_3$H$_3^+$ has alternative reaction routes competitive to the dissociative recombination with electrons, e.g. reaction with acetylene [133].

- The photodissociation rate for *c*-C$_3$H$_2$ is larger than for *l*-C$_3$H$_2$, and this would explain the lower abundance ratio toward sources less protected from photons than cold cores such as TMC-1 [133].

The cyclic to linear C$_3$H$_2$ abundance ratio has been studied also in the Horsehead Nebula photon-dominated region [129]: a value of 3-5 is found in the diffuse gas (consistent with the results of Cernicharo [133]). This value increases by a factor larger than 4 while penetrating the denser region of the cloud.

l-C$_3$H$_2$ has been proposed to be the carrier of the diffuse interstellar bands (DIBs) [136]. This hypothesis is controversial since the abundance of *l*-C$_3$H$_2$ appears to be too low to account for the DIBs features [130].

6.1.3   Previous laboratory studies on *l*-C$_3$HD

Kim and Yamamoto [137] measured the $1_{0,1}$ - $0_{0,0}$ and $2_{0,2}$ - $1_{0,1}$ rotational transitions of *l*-C$_3$HD with a Fourier Transform Microwave Spectrometer (FTMW), at 19 and 38 GHz respectively, and derived effective rotational constant and centrifugal distortion constant. The predicted catalog on the Cologne Database for Molecular Spectroscopy (CDMS) [6] is based solely on these two transitions, therefore predictions at frequencies higher than 100 GHz have to be regarded with caution.

6.2   Linear C$_3$HD in space

The spectrum of *l*-C$_3$HD observed toward TMC-1C is shown in Figure 6.2, together with the spectra of *l*-C$_3$H$_2$. A small shift in velocity can be seen in the line of

l-C$_3$HD with respect to the lines of *l*-C$_3$H$_2$. The frequency that I used for *l*-C$_3$HD is the one reported in the CDMS, and the shift can be motivated with the fact that the rest frequency employed is extrapolated from two centimeter-wave transitions, see 6.1.3.

In order to confirm the detection of this new interstellar molecule in TMC-1C, the observation of at least another line of *l*-C$_3$HD is necessary. Owing to the very low line density in this source in the 3 mm region (about 20 lines in 1.8 GHz in our observations), one can estimate the probability of a misidentification by considering the probability of another line falling within 2 times the typical line width (2×100 kHz). The probability of the line tentatively identified as *l*-C$_3$HD to belong to another carrier is very low (1:454). With the detection of a second line, the probability of a misidentification will be reduced to 1:206000. For this reason, the observations of a second line would give the confidence necessary for a firm first detection.
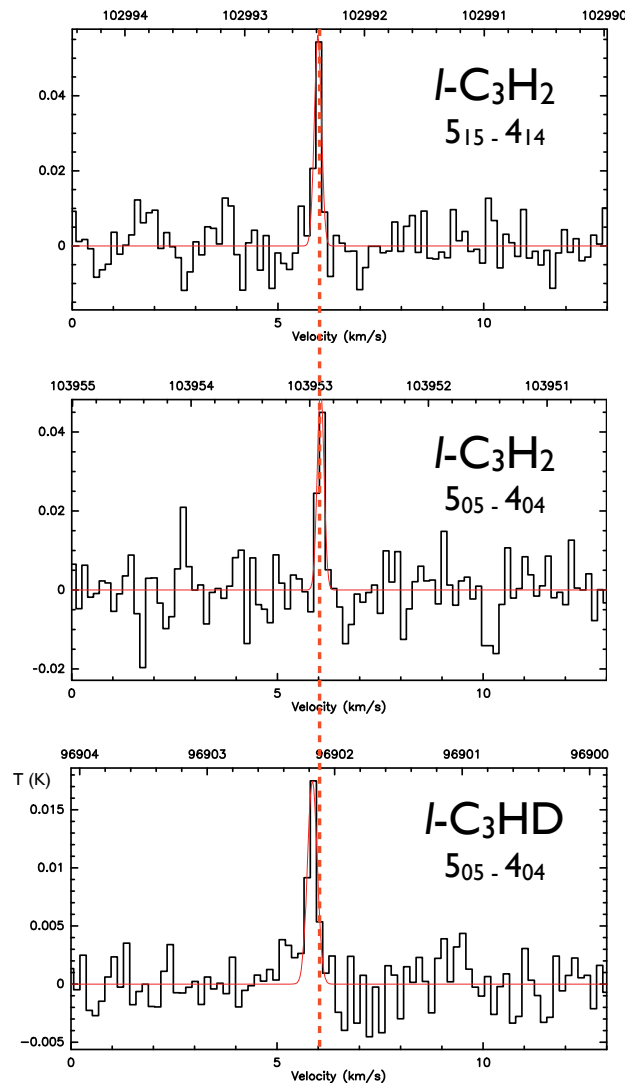
FIGURE 6.2: Linear C$_3$H$_2$ and C$_3$HD observed toward TMC-1C with the IRAM 30m telescope during our observations in late September 2012. By using the frequency in the CDMS catalog for the *l*-C$_3$HD, a small shift in velocity is present.

6.2.1   Extreme deuteration

The *l*-C$_3$HD/*l*-C$_3$H$_2$ ratio that I observed in TMC-1C is extremely high, around 50%. For the cyclic isomer the same ratio is about 10%. In Table 6.1 the column densities in TMC-1C are reported for the linear and cyclic C$_3$H$_2$ and C$_3$HD. In order to understand which processes are responsible for this extreme deuteration, a model has to be set up, which treats the deuteration reactions for linear and

cyclic C$_3$H$_2$ separately. The column densities have been calculated using the same expression reported in Chapter 5, equations 5.1 - 5.3. Also interesting is that the temperature estimated for the *l*-C$_3$H$_2$ from the intensity ratio between the 2 lines shown in Figure 6.2, is around 18 K. This temperature is considerably higher than the 9 K of the cyclic isomer in the same source [105]. The difference in temperature between the linear and cyclic isomer would suggest that the linear isomer is tracing a warmer part of the cloud. Cernicharo et al. [127], derived a T$_{rot}$ = (6 ± 1) K for *l*-C$_3$H$_2$ in TMC (α_{1950} = $04^h 38^m 36^s$.9, δ_{1950} = $+25°36'00''$). The source position that has been used for our observations of TMC-1C is α_{1950} = $04^h 38^m 12^s$, δ_{1950} = $+25°44'00''$). As the coordinates used in the two observations differ in declination by an amount larger than the telescope beam, the difference in temperature between our measurements and those by Cernicharo [127] is reasonable.

In case this detection will be confirmed, the deuteration of the linear C$_3$H$_2$ will pose new challenges to the current deuteration models because it is extremely high, and because of the possibility that the linear isomer of C$_3$H$_2$ is tracing the outer and warmer part of the cloud. In present models, the enhancement in deuterium fractionation is related also to the freeze out of CO on dust grains in the inner parts of the clouds [118]. This mechanisms would possibly not apply for *l*-C$_3$H$_2$. Furthermore the singly and doubly deuterated isotopologues of *c*-C$_3$H$_2$ have already been detected in the ISM [138]. The detection of the monodeuterated isotopologue of the linear isomer, *l*-C$_3$HD, will finally allow to test deuteration models that treat the cyclic and linear isomers of C$_3$H$_2$ separately.

TABLE 6.1: Observed line parameters for *l*-C$_3$H$_2$ and *l*-C$_3$HD toward TMC-1C. T$_{ex}$ is assumed to be 18 K for *l*-C$_3$H$_2$ and 9 K for *l*-C$_3$HD.

	l-C$_3$H$_2$	*l*-C$_3$H$_2$	*l*-C$_3$HD
Transition ($J_{K_a K_c}$)	5_{15} - 4_{14}	5_{05} - 4_{04}	5_{05} - 4_{04}
Frequency (GHz)	102.992	103.952	96.902
E$_{up}$ (cm^{-1})	19.59	10.40	9.70
T$_{mb}$ (mK)	57	52	17
W ($\times 10^{-2}$ K km s^{-1})	1.2(2)	1.1(2)	0.5(1)
V$_{LSR}$ (km s^{-1})	5.97(1)	6.05(2)	6.09(2)
δV (km s^{-1})	0.21(3)	0.20(4)	0.26(4)
N$_u$ ($\times 10^9$) cm^{-2}	2.8(4)	2.5(5)	1.1(2)
N$_{tot}$ ($\times 10^{10}$) cm^{-2}	6.1(9)	7.8(2)	3.3(5)

6.3   New laboratory measurements for *l*-C$_3$HD

Prior to this work just two cm-wave lines of *l*-C$_3$HD had been measured at 19 and 38 GHz [137]. In order to obtain precise rest frequencies for the observations, some rotational lines of linear C$_3$HD have been measured between 96 and 194 GHz by Carl Gottlieb at the Harvard Smithsonian Center for Astrophysics (priv. comm.). All new measurements are summarized in Table 6.2. By using the laboratory measured rest frequency for the $5_{0,5} - 4_{0,4}$ line of linear C$_3$HD, the small velocity shift present in Figure 6.2 disappears, as shown in Figure 6.3. Having accurate rest frequencies measured in the laboratory is crucial to have a secure detection when observing narrow line sources like TMC-1C. The differences between the observed frequencies and the ones present in the CDMS [6] span a range from 60 to almost 600 kHz, see Table 6.2, while the line width in TMC-1C is around 100 kHz. Such differences do not allow for a firm identification of new species in space. High resolution laboratory spectroscopy is therefore necessary.

TABLE 6.2: Measured rotational transitions frequencies of *l*-C$_3$HD with uncertainties, quantum numbers and residuals $O-C$ between the observed frequencies and those calculated reported on the CDMS.

$J_{K_a K_c} \rightarrow J'_{K'_a K'_c}$	Frequency (MHz)	$O - C$ (kHz)
$4_{04} \rightarrow 5_{05}$	96902.187(5)	60
$5_{05} \rightarrow 6_{06}$	116271.438(5)	114
$6_{06} \rightarrow 7_{07}$	135634.586(5)	188
$8_{08} \rightarrow 9_{09}$	174338.544(5)	419
$9_{09} \rightarrow 10_{010}$	193677.324(5)	561
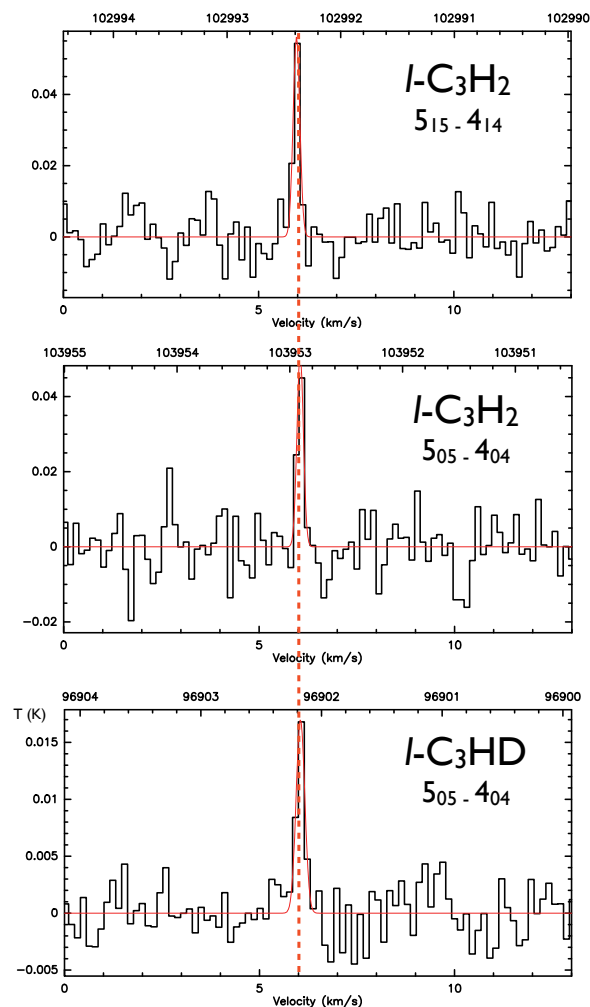
FIGURE 6.3: Linear C_3H_2 and C_3HD observed toward TMC-1C with the IRAM 30m telescope during our observations in late September 2012. By using the rest frequency measured in the laboratory for l-C_3HD (Gottlieb, priv. comm.), the small shift in velocity present in Figure 6.2 disappears.

6.4   Proposal for the IRAM 30 m telescope

A proposal for observing one additional line of l-C_3HD in TM-1C has been submitted to the IRAM 30 m telescope for the winter season 2013/2014. Our previous observations have shown that the $5_{0,5} - 4_{0,4}$ line of l-C_3HD at 96 GHz in TMC-1C has a main beam temperature of 17 mK, see Figure 6.2 or Figure 6.3. For l-C_3H_2 we have derived an excitation temperature of about 18 K from the line ratio of the two lines we detected in the previous observations, assuming local thermodynamic equilibrium (LTE). In order to plan the observations the expected line temperatures have been calculated assuming an excitation temperature of 18 K for l-C_3H_2

and 9 K for *l*-C$_3$HD. A lower temperature has been assumed for *l*-C$_3$HD since deuterated isotopologues usually trace colder parts of the clouds. The expected line temperatures have been calculated in the following way. Once calculated the total column density (N_{tot}) for the observed line of *l*-C$_3$H$_2$ and *l*-C$_3$HD, see Table 6.1, the upper state column density (N_{up}) for a given transition, has been calculated using this expression:

$$N_{up} = \frac{N_{tot} g_u}{Q_{rot}(T_{ex}) e^{\left(\frac{E_u}{kT_{ex}}\right)}} \tag{6.1}$$

where g_u is the degeneracy of the upper state defined as the nuclear spin statistical weight (see Table 2.1) times the spin rotation degeneracy $2J + 1$, E_u is the energy of the upper state, k is the Boltzmann constant, and Q_{rot} is the partition function of the molecule at the excitation temperature T_{ex}. The optical depth is calculated as following:

$$\tau = \frac{N_{up} c^3 A_{ul} 2\sqrt{\ln 2}(e^{\frac{h\nu}{kT_{ex}}} - 1)}{8\pi\nu^3 \sqrt{\pi}\Delta\nu} \tag{6.2}$$

and subsequently the expected main beam temperature for the given transition is determined via

$$T_{mb} = (J(T_{ex}) - J(T_{bg}))(1 - e^{-\tau}) \tag{6.3}$$

where ν is the frequency of the line, h is the Planck constant, c is the speed of light, A_{ul} is the Einstein coefficient of the transition, $\Delta\nu$ is the full width at half maximum, T_{bg} and T_{mb} are the background (2.7 K) and the main beam temperatures respectively.

The expected main beam temperatures for different transitions of *l*-C$_3$H$_2$ and *l*-C$_3$HD falling in the frequency ranges covered by the 30 m telescope are reported in Table 6.3. The expected temperatures have been calculated at both temperatures for both isotopologues, but when planning the observations we assume 18 K for the fully hydrogenated molecule and 9 K for the deuterated molecule. It is not possible to observe the line of *l*-C$_3$HD at 116 GHz in a reasonable amount of time, because it is too close to an atmospheric O$_2$ line. Given the very low expected temperature for the line at 155 GHz, and the non feasibility to observe

simultaneously two sub-bands with the EMIR E150 receiver*, the only line that I proposed to observe is the 7_{07} - 6_{06} line at 136 GHz. The observational set-up proposed to the IRAM 30 telescope is sketched in Figure 6.4. I plan to perform the observations using three EMIR setups. By combining different receiver bands and backends, it will be possible to observe other frequency windows while integrating on the weak l-C$_3$H$_2$ line.

One line for each isomer will also be observed with high resolution and high S/N ratio to model the line profile and understand which part of the cloud is tracing. In order to better understand the formation of deuterated isotopologues of linear and cyclic C$_3$H$_2$, it is important to know which part of the cloud they are tracing. This is possible by modeling the line profile of the line [139]. To do so, I want to observe both the linear and cyclic isomer at high frequency resolution and with high signal to noise, namely the $5_{0,5} - 4_{0,4}$ transition of l-C$_3$H$_2$ at 103 GHz, and the $2_{1,2} - 1_{0,1}$ transitions of c-C$_3$H$_2$ at 85 GHz.

In order to constrain the measurement of the rotational temperature of l-C$_3$H$_2$ in TMC-1C, two additional lines respect to the ones shown in Figure 6.2 will be observed. The rotational temperature of 18 K has been inferred just by comparing the intensity ratio of the two lines in Figure 6.2 with the intensity ratio calculated with the CDMS intensity values at 18 K and 9 K. With the observation of two additional lines it will be possible to make a rotational temperature diagram.

---

*The E150 band of EMIR covers the 125-186 GHz frequency range. http://www.iram.es/IRAMES/mainWiki/EmirforAstronomers

Table 6.3: Expected main beam temperatures for three transitions of *l*-C$_3$HD, calculated assuming T$_{ex}$ = 9 and T$_{ex}$ = 18 K.

Transition	Frequency	T$_{mb}(9K)$	T$_{mb}(18$ K$)$
	(GHz)	mK	mK
l-C$_3$HD			
6_{06} - 5_{05}	116.27	15	18
7_{07} - 6_{06}	135.63	10	17
8_{08} - 7_{07}	154.99	5	15
l-C$_3$H$_2$			
4_{14} - 3_{13}	82.39	59	45
4_{04} - 3_{03}	83.16	92	34
7_{17} - 6_{16}	144.18	28	56
7_{07} - 6_{06}	145.52	47	45
8_{18} - 7_{17}	164.77	16	48
8_{08} - 7_{07}	166.30	20	26

EMIR BAND E150
LI sub-band FTS 50 kHz
F$_{LO}$: 142.2 GHz rms: 4 mK
TARGET: detection of l-C$_3$H$_2$ @ 136 GHz
TIME ESTIMATED: 24 h

+

EMIR BAND E090
LO sub-band FTS 50 kHz
F$_{LO}$: 91.9 GHz rms: 8 mK
TARGET: detection of l-C$_3$H$_2$ @ 83.1 & 82.3 GHz
TIME ESTIMATED: 4 h

EMIR BAND E090
LI sub-band VESPA 10 kHz
F$_{LO}$: 103.9 GHz rms: 12 mK
TARGET: line profile of c-C$_3$D$_2$ @ 97 GHz
TIME ESTIMATED: 8 h

EMIR BAND E090
LI sub-band FTS 50 kHz
F$_{LO}$: 110.3 GHz rms: 10 mK
TARGET: line profile of l-C$_3$H$_2$ @ 103 GHz
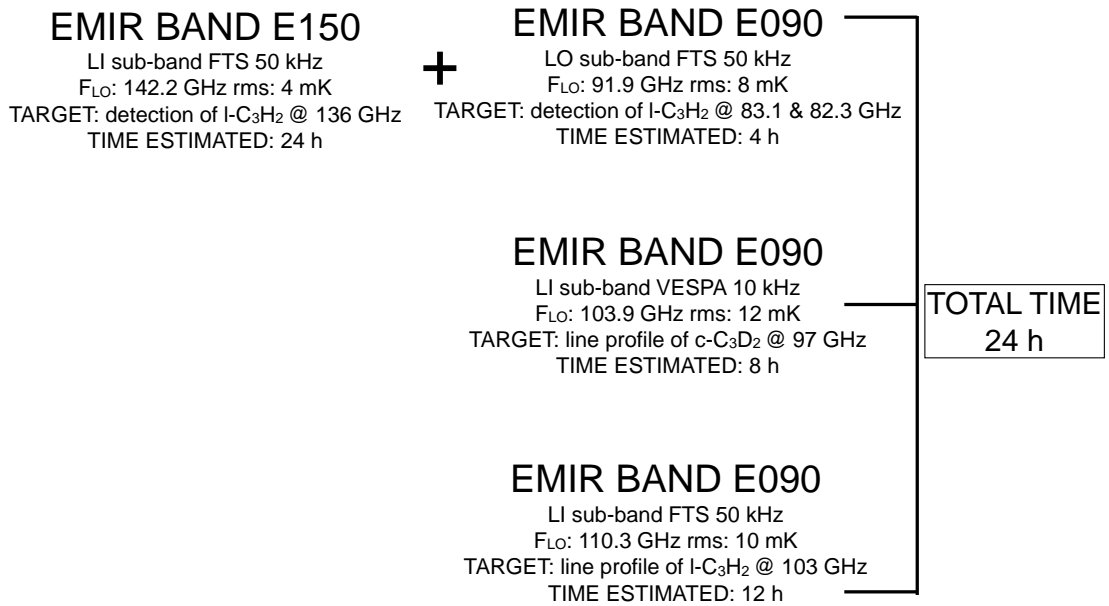TIME ESTIMATED: 12 h

TOTAL TIME
24 h

Figure 6.4: Proposed observational setups. The EMIR bands E090 and E150 cover the 83-117 and 125-186 GHz frequency ranges, respectively. FTS and VESPA are the backends. FTS is the Fourier Transform Spectrometer. VESPA is the VErsatile SPectrometer Array.

6.4.1   Additional noise

When combining two bands of EMIR, additional noise is added by the use of the dichroic elements. Additional noise could compromise a secure detection in case you are observing a weak line. This is the case for l-C$_3$HD, so I have calculated the additional amount of noise. On the IRAM 30 m web pages, the losses due to the dichroics are reported in terms of increase of receiver temperature. In order to take into account this losses, the increase in receiver temperature has to be expressed in terms of increase of system temperature, this can subsequently be converted in rms noise temperature. The radiometer equation for a total power measurement is

$$\sigma = \frac{T_{sys}}{\eta_{spec}\sqrt{\Delta\nu t}} \tag{6.4}$$

where σ is the rms noise obtained when integrating for a time t with a frequency resolution of $\Delta\nu$, T_{sys} is the system temperature and η_{spec} is the efficiency of the spectrometer. The system temperature is defined as following:

$$T_{sys} = \frac{(1 + G_{im}e^{\tau_s A})}{F_{eff}}[F_{eff}T_{atm}(1 - e^{-\tau_s A}) + (1 - F_{eff})T_{cab} + T_{rec}] \tag{6.5}$$

where G_{im} is the receiver image gain, τ_s is the atmospheric opacity, $A = 1/\sin(\text{elevation})$, F_{eff} is the telescope forward efficiency ($\sim$0.9), T_{amb} is the mean atmospheric temperature, T_{cab} is the temperature in the receiver cabin, and T_{rec} is the receiver temperature. For our purposes we just need to know the change in T_{sys} related to a change in T_{rec}. Which is:

$$\Delta T_{sys} = \frac{(1 + G_{im}\exp\tau_s A)}{F_{eff}}\Delta T_{rec} \tag{6.6}$$

By using the characteristic values of $G_{im} = 0.1$, $\tau_s \simeq 0.1$, and $F_{eff} \simeq 0.9$ from the IRAM 30 m manual, and considering an elevation of the source of 50 degrees, we obtain:

$$\Delta T_{sys} = 4.25 \times \Delta T_{rec} \tag{6.7}$$

By combining 6.4 and 6.7, the increase in T_{rec} tabulated for different receiver bands combinations at different frequency ranges, has been converted in additional rms

noise (σ). Table 6.4 summarizes the different parameters used for calculating the increase in noise for the different lines that we propose to observe.

TABLE 6.4: Additional noise produced by the use of dichroics, calculated for the different lines present in the proposal.

Line(s)	ΔT_{rec} (K)	ΔT_{sys} (K)	$\Delta\nu$ (kHz)	time	$\Delta\sigma$ (mK)
l-C$_3$HD at 136 GHz	4	17	50	36 h	**0.23**
l-C$_3$H$_2$ at 103 GHz	20	85	20	32 h	**2**
l-C$_3$H$_2$ at 82 and 83 GHz	16	68	50	4.5 h	**2.6**
c-C$_3$H$_2$ at 85 GHz	12	51	20	1 min	**69**

6.5   Perspectives

The tentative detection of *l*-C$_3$HD in the starless core TMC-1C is strongly supported from laboratory evidences. The detection of one additional line, despite it is quite challenging in terms of telescope time, is crucial to make a conclusive detection. If the detection will be confirmed, the deuteration of *l*-C$_3$H$_2$ will pose new challenges to the deuteration models. To the best of my knowledge no molecule in the ISM is as enriched in deuterium as *l*-C$_3$H$_2$ appears to be. In Table 6.5 are reported the deuterium fractionation of some molecules detected in TMC-1C. The *l*-C$_3$H$_2$/*l*-C$_3$HD which is inferred from the spectra in Figure 6.2 is around 50%. This exceeds known ratios detected in this source by at least a factor of 4. It is important to confirm such a high enrichment in deuterium for *l*-C$_3$H$_2$, and subsequently adapt the current models to explain this ratio. Should the high degree of deuteration of *l*-C$_3$H$_2$ be confirmed, it would be interesting to observe also the doubly deuterated isotopologue, *l*-C$_3$D$_2$.

The observations that I proposed to perform at the 30 m telescope, furthermore, aim at studying and modeling the deuteration of both isomers for the first time. The singly and doubly deuterated isotopologues of *c*-C$_3$H$_2$ have already been detected in the ISM [138]: the detection of the monodeuterated isotopologue of the linear isomer, *l*-C$_3$HD, will finally allow us to test deuteration models that treat separately the cyclic and linear isomers of C$_3$H$_2$. These models are actually under development in a group of collaborator.

TABLE 6.5: Abundance ratios of deuterated molecules in TMC-1C

	TMC-1C	Reference
[c-C$_3$D$_2$]/[c-C$_3$H$_2$]	(0.4 - 0.8)%	Spezzano et al., 2013
[c-C$_3$D$_2$]/[c-C$_3$HD]	(3 - 15)%	Spezzano et al., 2013
[c-C$_3$HD]/[c-C$_3$H$_2$]	(5 - 13)%	Spezzano et al., 2013
[DCO$^+$]/[HCO$^+$]	2%	Tiné et al., 2000
[N$_2$D$^+$]/[N$_2$H$^+$]	8%	Tiné et al., 2000
[NH$_2$D]/[NH$_3$]	1%	Tiné et al., 2000
[*l*-C$_3$HD]/[*l*-C$_3$H$_2$]	**(42 - 54)%**	**tentatively detected in this work**

Finally it is important to understand which part of the cloud is traced by each isomer. It has been shown by Teyssier and coworkers [129] that the cyclic-to-linear ratio of C$_3$H$_2$ is sensitive to the electron abundance of the medium. The cyclic to linear ratio has been monitored in the Horsehead Nebula photon-dominated region. A value of 3-5 has been found in the diffuse gas, and this value increases by a factor larger than 4 while penetrating the denser region of the cloud. It is possible to model the profile of a molecular line and infer which part of the molecular cloud is traced by that molecule [139]. In order to make this kind of study on the linear and cyclic C$_3$H$_2$, it has been proposed to observe one line of each isomer with high spectral resolution, and high signal to noise ratio.

In a recent observing run at the IRAM 30 m telescope, the line at 96.9 GHz tentatively identified as *l*-C$_3$HD has been observed also toward the starless core L1544. The spectrum is shown in Figure 6.5 in comparison with two previously detected lines of *l*-C$_3$H$_2$. The ratio that can be inferred from this line with respect to the lines of *l*-C$_3$H$_2$ previously observed in the same source is around 30%.

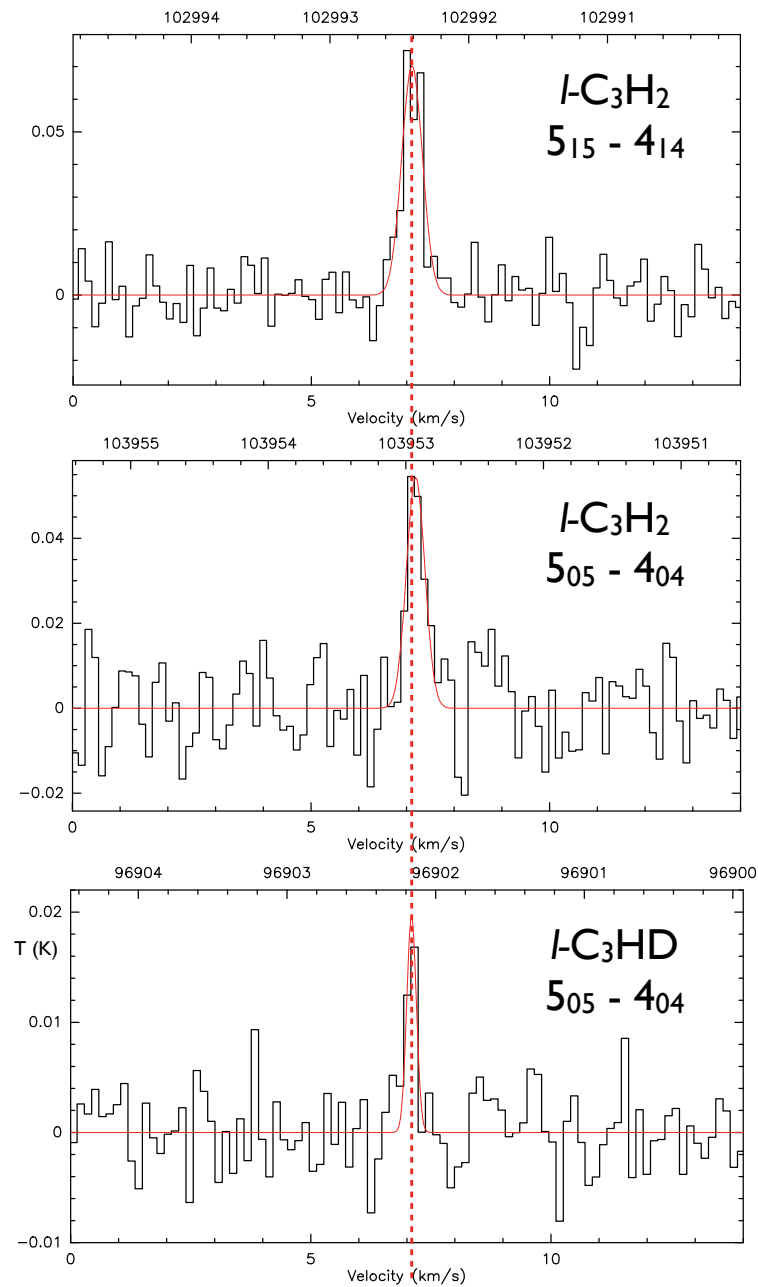FIGURE 6.5: Linear C$_3$H$_2$ and C$_3$HD observed toward L1544 with the IRAM 30m telescope. The spectra of *l*-C$_3$H$_2$ have been observed in September 2012, while the spectrum of *l*-C$_3$HD is an average of scans from September 2012 and October 2013.

Appendix A

MAPLE mini model

Maple is a computer algebra system, very useful to do simple programming. It has been used in this thesis to reproduce the observed abundances of c-C_3H_2, c-C_3HD, and c-C_3D_2 with a simple reaction scheme that is explained in Chapter 5. In reaction rates equations presented here, c0 represents the concentration of c-C_3H_2, c1 the concentration of c-C_3HD, and c2 the concentration of c-C_3D_2. The reaction rates are solved by assuming to have just c-C_3H_2 at the beginning, c0(0) = 1 while c1(0) = c2(0) = 0.

The time t in the model is actually t/τ, and we assume that the time constant of the process, τ, is defined solely by the rate of protonation/deuteration of either c-C_3H_2, c-C_3HD, or c-C_3D_2.

$restart : with(plots) :$

$sys := \dfrac{d}{dt} c0(t) = + \dfrac{1}{4} \cdot \left(-1 \cdot c0(t) + \dfrac{6}{9} \cdot c1(t) \right), \dfrac{d}{dt} c1(t) = \dfrac{1}{4} \cdot \left(1 \cdot c0(t) - \dfrac{12}{9} \cdot c1(t) + \dfrac{12}{9} \right.$
$\left. \cdot c2(t) \right), \dfrac{d}{dt} c2(t) = \dfrac{1}{4} \cdot \left(\dfrac{6}{9} \cdot c1(t) - \dfrac{12}{9} \cdot c2(t) \right); ics := c0(0) = 1, c1(0) = 0, c2(0) = 0; p$
$:= dsolve(\{sys, ics\});$

$\dfrac{d}{dt} c0(t) = -\dfrac{1}{4} c0(t) + \dfrac{1}{6} c1(t), \dfrac{d}{dt} c1(t) = \dfrac{1}{4} c0(t) - \dfrac{1}{3} c1(t) + \dfrac{1}{3} c2(t), \dfrac{d}{dt} c2(t)$

$= \dfrac{1}{6} c1(t) - \dfrac{1}{3} c2(t)$

$$c0(0) = 1, c1(0) = 0, c2(0) = 0$$

$\left\{ c0(t) = -\dfrac{5}{2} \left(-\dfrac{3}{13} + \dfrac{6}{221} \sqrt{17} \right) e^{\frac{1}{24}(-11+\sqrt{17})t} - \dfrac{1}{2} \left(-\dfrac{3}{13} \right.\right.$ **(1)**

$\left. + \dfrac{6}{221} \sqrt{17} \right) e^{\frac{1}{24}(-11+\sqrt{17})t} \sqrt{17} - \dfrac{5}{2} \left(-\dfrac{3}{13} - \dfrac{6}{221} \sqrt{17} \right) e^{-\frac{1}{24}(11+\sqrt{17})t}$

$+ \dfrac{1}{2} \left(-\dfrac{3}{13} - \dfrac{6}{221} \sqrt{17} \right) e^{-\frac{1}{24}(11+\sqrt{17})t} \sqrt{17} + \dfrac{4}{13}, c1(t) = \dfrac{6}{13} + \left(-\dfrac{3}{13} \right.$

$\left. + \dfrac{6}{221} \sqrt{17} \right) e^{\frac{1}{24}(-11+\sqrt{17})t} + \left(-\dfrac{3}{13} - \dfrac{6}{221} \sqrt{17} \right) e^{-\frac{1}{24}(11+\sqrt{17})t}, c2(t) = \dfrac{3}{2} \left(\right.$

$\left. -\dfrac{3}{13} + \dfrac{6}{221} \sqrt{17} \right) e^{\frac{1}{24}(-11+\sqrt{17})t} + \dfrac{1}{2} \left(-\dfrac{3}{13} + \dfrac{6}{221} \sqrt{17} \right) e^{\frac{1}{24}(-11+\sqrt{17})t} \sqrt{17}$

$+ \dfrac{3}{2} \left(-\dfrac{3}{13} - \dfrac{6}{221} \sqrt{17} \right) e^{-\frac{1}{24}(11+\sqrt{17})t} - \dfrac{1}{2} \left(-\dfrac{3}{13} \right.$

$\left.\left. - \dfrac{6}{221} \sqrt{17} \right) e^{-\frac{1}{24}(11+\sqrt{17})t} \sqrt{17} + \dfrac{3}{13} \right\}$

$c0prime := rhs(p[1]);$

$-\dfrac{5}{2} \left(-\dfrac{3}{13} + \dfrac{6}{221} \sqrt{17} \right) e^{\frac{1}{24}(-11+\sqrt{17})t} - \dfrac{1}{2} \left(-\dfrac{3}{13} \right.$ **(2)**

$\left. + \dfrac{6}{221} \sqrt{17} \right) e^{\frac{1}{24}(-11+\sqrt{17})t} \sqrt{17} - \dfrac{5}{2} \left(-\dfrac{3}{13} - \dfrac{6}{221} \sqrt{17} \right) e^{-\frac{1}{24}(11+\sqrt{17})t}$

$+ \dfrac{1}{2} \left(-\dfrac{3}{13} - \dfrac{6}{221} \sqrt{17} \right) e^{-\frac{1}{24}(11+\sqrt{17})t} \sqrt{17} + \dfrac{4}{13}$

$c1prime := rhs(p[2]);$

$\dfrac{6}{13} + \left(-\dfrac{3}{13} + \dfrac{6}{221} \sqrt{17} \right) e^{\frac{1}{24}(-11+\sqrt{17})t} + \left(-\dfrac{3}{13} - \dfrac{6}{221} \sqrt{17} \right) e^{-\frac{1}{24}(11+\sqrt{17})t}$ **(3)**

$c2prime := rhs(p[3]);$

$$\frac{3}{2}\left(-\frac{3}{13}+\frac{6}{221}\sqrt{17}\right)e^{\frac{1}{24}\left(-11+\sqrt{17}\right)t}+\frac{1}{2}\left(-\frac{3}{13}+\frac{6}{221}\sqrt{17}\right)e^{\frac{1}{24}\left(-11+\sqrt{17}\right)t}\sqrt{17} \qquad \textbf{(4)}$$

$$+\frac{3}{2}\left(-\frac{3}{13}-\frac{6}{221}\sqrt{17}\right)e^{-\frac{1}{24}\left(11+\sqrt{17}\right)t}-\frac{1}{2}\left(-\frac{3}{13}\right.$$

$$\left.-\frac{6}{221}\sqrt{17}\right)e^{-\frac{1}{24}\left(11+\sqrt{17}\right)t}\sqrt{17}+\frac{3}{13}$$

$cprime := c0prime + c1prime + c2prime;$

$$1 \qquad\qquad \textbf{(5)}$$

$plot(\{c0prime, c1prime, c2prime, cprime\}, t = 0 ..20, color = [red, blue, green, orange]);$
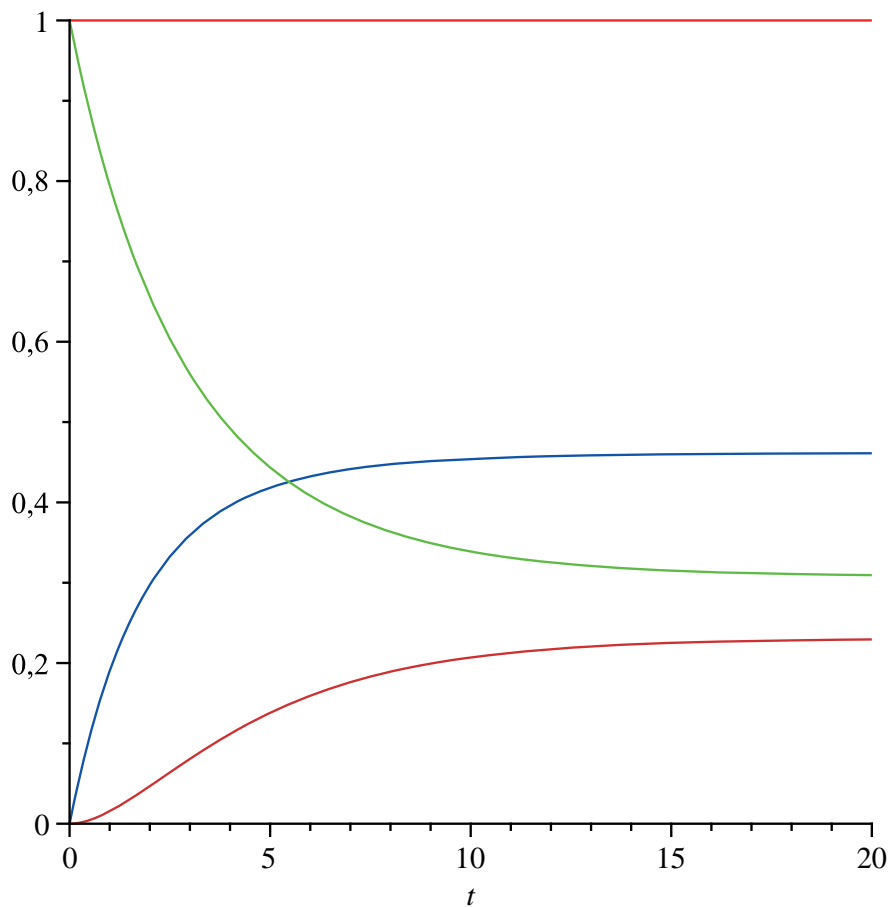
$plot\left(\left\{\dfrac{c1prime}{c0prime}, \dfrac{c2prime}{c1prime}\right\}, t = 0 ..0.5, 0 ..0.1, color = [red, blue]\right);$
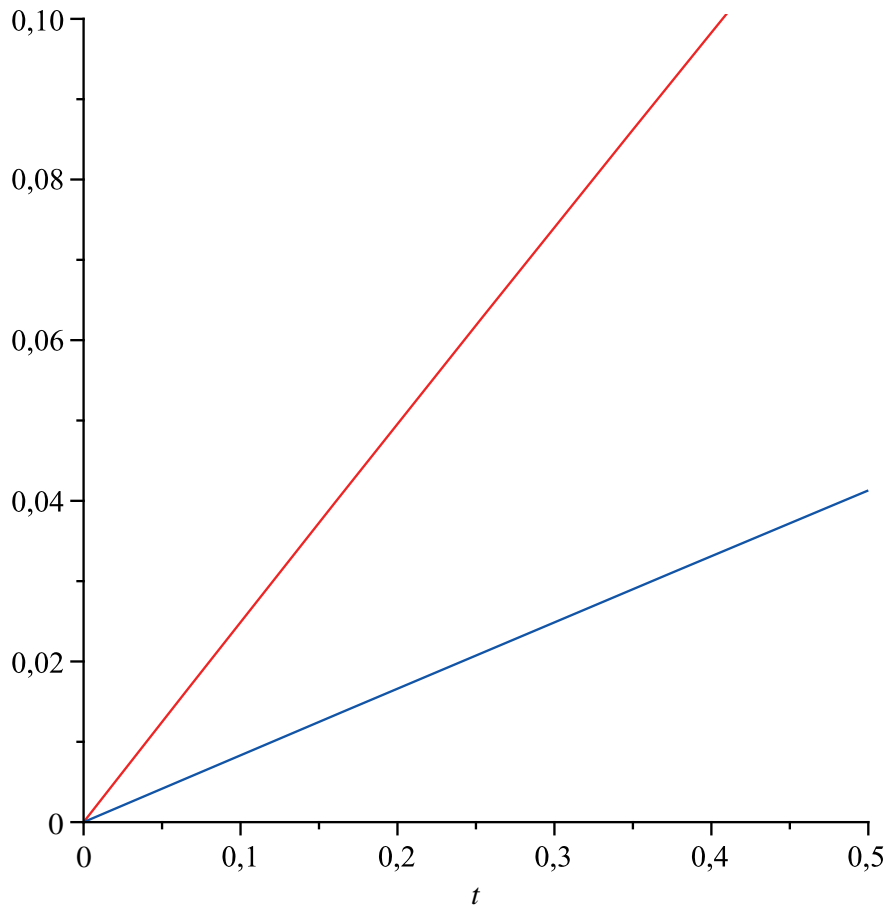
#*logplot({{c0prime, c1prime, c2prime, cprime}, t = 0 ..1, 1e−4 ..0.1 color = [red, blue, green, orange]);*
#*logplot({{c0prime, c1prime, c2prime, cprime}, t = 0 ..0.3, 1e−4 ..0.1 color = [red, blue, green, orange);*

Bibliography

[1] P. Goldreich and J. Kwan. Molecular Clouds. *ApJ*, 189:441–454, May 1974. doi: 10.1086/152821.

[2] B. Zuckerman and N. J. Evans, II. Models of massive molecular clouds. *ApJ*, 192:L149–L152, September 1974. doi: 10.1086/181613.

[3] A. Belloche, P. André, D. Despois, and S. Blinder. Molecular line study of the very young protostar IRAM 04191 in Taurus: infall, rotation, and outflow. *A&A*, 393:927–947, October 2002. doi: 10.1051/0004-6361:20021054.

[4] P. Swings and L. Rosenfeld. Considerations Regarding Interstellar Molecules. *ApJ*, 86:483–486, November 1937. doi: 10.1086/143880.

[5] A. A. Penzias and R. W. Wilson. A Measurement of Excess Antenna Temperature at 4080 Mc/s. *ApJ*, 142:419–421, July 1965. doi: 10.1086/148307.

[6] H. S. P. Müller, F. Schlöder, J. Stutzki, and G. Winnewisser. The Cologne Database for Molecular Spectroscopy, CDMS: a useful tool for astronomers and spectroscopists. *Journal of Molecular Structure*, 742:215–227, May 2005. doi: 10.1016/j.molstruc.2005.01.027.

[7] R. L. Poynter and H. M. Pickett. Submillimeter, millimeter, and microwave spectral line catalog. *Applied Optics*, 24:2235–2240, 1985. doi: 10.1364/AO. 24.002235.

[8] H. M. Pickett. The fitting and prediction of vibration-rotation spectra with spin interactions. *Journal of Molecular Spectroscopy*, 148:371–377, August 1991. doi: 10.1016/0022-2852(91)90393-O.

[9] Z. Nagy. Molecular line tracers of high-mass star forming regions. *PhD Thesis*, 2013.

[10] C. H. Townes and A. L. Schawlow. *Microwave Spectroscopy.* New York: McGraw-Hill, 1955.

[11] P. F. Bernath. *Spectra of Atoms and Molecules.* Oxford University Press, 1995.

[12] W. Gordy and R. L. Cook. *Microwave Molecular Spectroscopy.* Wiley, New York, 1984.

[13] J. L. Dunham. The Energy Levels of a Rotating Vibrator. *Physical Review*, 41:721–731, September 1932. doi: 10.1103/PhysRev.41.721.

[14] M. Born and R. Oppenheimer. Zur Quantentheorie der Molekeln. *Annalen der Physik*, 389:457–484, 1927. doi: 10.1002/andp.19273892002.

[15] J. K. G. Watson. The isotope dependence of diatomic Dunham coefficients. *Journal of Molecular Spectroscopy*, 80:411–421, April 1980. doi: 10.1016/0022-2852(80)90152-6.

[16] J. M. Vrtilek, C. A. Gottlieb, and P. Thaddeus. Laboratory and astronomical spectroscopy of C_3H_2, the first interstellar organic ring. *ApJ*, 314:716–725, March 1987. doi: 10.1086/165099.

[17] C Endres. Aufbau eines Multiplier-Terahertzspektrometers und seine Anwendung in der hochauflosenden Laborspektroskopie. *Diplomarbeit*, 2004.

[18] D. Buhl and L. E. Snyder. Unidentified Interstellar Microwave Line. *Nature*, 228:267–269, October 1970. doi: 10.1038/228267a0.

[19] W. Klemperer. Carrier of the Interstellar 89.190 GHz Line. *Nature*, 227: 1230, September 1970. doi: 10.1038/2271230a0.

[20] R. C. Woods, T. A. Dixon, R. J. Saykally, and P. G. Szanto. Laboratory microwave spectrum of HCO^+. *Phys. Rev. Lett.*, 35:1269–1272, November 1975. doi: 10.1103/PhysRevLett.35.1269.

[21] E. Herbst and W. Klemperer. The Formation and Depletion of Molecules in Dense Interstellar Clouds. *ApJ*, 185:505–534, October 1973. doi: 10.1086/152436.

[22] T. Oka. Observation of the infrared spectrum of H_3^+. *Phys. Rev. Lett.*, 45: 531–534, August 1980. doi: 10.1103/PhysRevLett.45.531.

[23] T. R. Geballe and T. Oka. Detection of H_3^+ in interstellar space. *Nature*, 384:334–335, November 1996. doi: 10.1038/384334a0.

[24] T. Oka. Spectroscopy and astronomy: H_3^+ from the laboratory to the Galactic center. *Faraday Discussions*, 150:9, 2011. doi: 10.1039/c1fd00092f.

[25] M. C. McCarthy, C. A. Gottlieb, H. Gupta, and P. Thaddeus. Laboratory and Astronomical Identification of the Negative Molecular Ion C_6H^-. *ApJ*, 652:L141, 2006. doi: 10.1086/510238.

[26] E. Herbst. Can negative molecular ions be detected in dense interstellar clouds. *Nature*, 289:656, February 1981. doi: 10.1038/289656a0.

[27] S. Brünken, H. Gupta, C. A. Gottlieb, M. C. McCarthy, and P. Thaddeus. Detection of the Carbon Chain Negative Ion C_8H^- in TMC-1. *ApJ*, 664: L43–L46, July 2007. doi: 10.1086/520703.

[28] J. Cernicharo, M. Guélin, M. Agúndez, M. C. McCarthy, and P. Thaddeus. Detection of C_5N^- and Vibrationally Excited C_6H in IRC +10216. *ApJ*, 688:L83–L86, December 2008. doi: 10.1086/595583.

[29] J. Cernicharo, M. Guélin, M. Agündez, K. Kawaguchi, M. McCarthy, and P. Thaddeus. Astronomical detection of C_4H^-, the second interstellar anion. *A&A*, 467:L37–L40, May 2007. doi: 10.1051/0004-6361:20077415.

[30] P. Thaddeus, C. A. Gottlieb, H. Gupta, S. Brünken, M. C. McCarthy, M. Agúndez, M. Guélin, and J. Cernicharo. Laboratory and Astronomical Detection of the Negative Molecular Ion C_3N^-. *ApJ*, 677:1132–1139, April 2008. doi: 10.1086/528947.

[31] M. Agúndez, J. Cernicharo, M. Guélin, C. Kahane, E. Roueff, J. Kłos, F. J. Aoiz, and F. et al. Lique. Astronomical identification of CN^-, the smallest observed molecular anion. *A&A*, 517:L2, February 2010. doi: 10.1051/0004-6361/201015186.

[32] A. von Engel and L. Marton. Ionized Gases. *Physics Today*, 18:64, 1965. doi: 10.1063/1.3046953.

[33] S. C. Foster and A. R. W. McKellar. The nu3 fundamental bands of $HN2^+$, $DN2^+$, and DCO^+. *Journal of Chemical Physics*, 81:3424–3428, October 1984. doi: 10.1063/1.448066.

[34] F. C. van den Heuvel and A. Dymanus. Observation of far-infrared transitions of HCO$^+$, CO$^+$ and HN$_2^+$. *Chemical Physics Letters*, 92:219–222, October 1982. doi: 10.1016/0009-2614(82)80263-7.

[35] F. C. de Lucia, E. Herbst, G. M. Plummer, and G. A. Blake. The production of large concentrations of molecular ions in the lengthened negative glow region of a discharge. *Journal of Chemical Physics*, 78:2312–2316, March 1983. doi: 10.1063/1.445004.

[36] T. Amano. Extended negative glow and "hollow anode" discharges for submillimeter-wave observation of CN$^-$, C$_2$H$^-$, and C$_4$H$^-$. *Journal of Chemical Physics*, 129(24):244305, December 2008. doi: 10.1063/1.3043739.

[37] C. S. Gudeman, M. H. Begemann, J. Pfaff, and R. J. Saykally. Velocity-modulated infrared laser spectroscopy of molecular ions: The nu$_1$ band of HCO$^+$. *Phys. Rev. Lett.*, 50:727–731, March 1983. doi: 10.1103/PhysRevLett.50.727.

[38] C. S. Gudeman and R. J. Saykally. Velocity Modulation Infrared Laser Spectroscopy of Molecular Ions. *Annual Review of Physical Chemistry*, 35: 387–418, October 1984. doi: 10.1146/annurev.pc.35.100184.002131.

[39] F. Tinti, L. Bizzocchi, C. Degli Esposti, and L. Dore. Improved Rest Frequencies of HCO$^+$ at 1 THz. *ApJ*, 669:L113–L116, November 2007. doi: 10.1086/523850.

[40] V. Lattanzi, A. Walters, B. J. Drouin, and J. C. Pearson. Rotational Spectrum of the Formyl Cation, HCO$^+$, to 1.2 THz. *ApJ*, 662:771–778, June 2007. doi: 10.1086/517602.

[41] A. Sternberg and A. Dalgarno. Chemistry in Dense Photon-dominated Regions. *ApJS*, 99:565, August 1995. doi: 10.1086/192198.

[42] W. B. Latter, C. K. Walker, and P. R. Maloney. Detection of the Carbon Monoxide Ion CO$^+$ in the Interstellar Medium and a Planetary Nebula. *ApJ*, 419:L97, December 1993. doi: 10.1086/187146.

[43] A. Fuente and J. Martin-Pintado. Detection of CO$^+$ toward the Reflection Nebula NGC 7023. *ApJ*, 477:L107, March 1997. doi: 10.1086/310532.

[44] C. Savage and L. M. Ziurys. Ion Chemistry in Photon-dominated Regions: Examining the [HCO$^+$]/[HOC$^+$]/[CO$^+$] Chemical Network. *ApJ*, 616:966–975, December 2004. doi: 10.1086/424964.

[45] J. R. Rizzo, A. Fuente, A. Rodríguez-Franco, and S. García-Burillo. Detection of Reactive Ions in the Ultracompact H II Regions Monoceros R2 and G29.96-0.02. *ApJ*, 597:L153–L156, November 2003. doi: 10.1086/379867.

[46] P. Stäuber and S. Bruderer. Excitation and abundance study of CO$^+$ in the interstellar medium. *A&A*, 505:195–203, October 2009. doi: 10.1051/0004-6361/200912381.

[47] T. A. Dixon and R. C. Woods. Microwave absorption spectrum of the CO$^+$ ion. *Phys. Rev. Lett.*, 34:61–63, January 1975. doi: 10.1103/PhysRevLett.34.61.

[48] K. V. L. N. Sastry, P. Helminger, E. Herbst, and F. C. De Lucia. Laboratory millimeter and submillimeter spectra of CO$^+$. *ApJ*, 250:L91, November 1981. doi: 10.1086/183680.

[49] N. D. Piltch, P. G. Szanto, T. G. Anderson, C. S. Gudeman, T. A. Dixon, and R. C. Woods. The microwave spectrum of isotopically substituted CO$^+$ ion. *Journal of Chemical Physics*, 76:3385–3388, April 1982. doi: 10.1063/1.443438.

[50] M. Bogey, C. Demuynck, and J. L. Destombes. Millimetre wave spectrum of CO in excited vibrational states. *Molecular Physics*, 46:679–681, 1982. doi: 10.1080/00268978200101521.

[51] M. Bogey, C. Demuynck, and J. L. Destombes. Equilibrium structure of CO$^+$ from its millimeter wave spectrum - Breakdown of the Born-Oppenheimer approximation. *Journal of Chemical Physics*, 79:4704–4707, November 1983. doi: 10.1063/1.445611.

[52] I. Savíc, S. Schlemmer, and D. Gerlich. Low-Temperature Experiments on the Formation of Deuterated C$_3$H$_3^+$. *ApJ*, 621:1163–1170, March 2005. doi: 10.1086/427648.

[53] G. Klapper. Präzisionsmessungen des Reinen Rotationspectrums von CO, CO$^+$ und ihren isotopomeren. *PhD Thesis, Universität zu Köln*, 2001.

[54] R. Gendriesch, K. Pehl, T. Giesen, , G. Winnewisser, and F. Lewen. Terahertz spectroscopy of linear tratomic CCC: high precision laboratory measurements and analysis of the ro-vibrational bending transitions. *Z. Naturforsch.*, 58, January 2003.

[55] J. K. Thompson, S. Rainville, and D. E. Pritchard. Cyclotron frequency shifts arising from polarization forces. *Nature*, 430:58–61, July 2004. doi: 10.1038Natureure02682.

[56] M. Redshaw, B. J. Mount, and E. G. Myers. Penning-trap measurement of the atomic masses of ^{18}O and ^{19}F with uncertainties 0.1 parts per 10^9. *Phys. Rev. A*, 79(1):012507, January 2009. doi: 10.1103/PhysRevA.79.012507.

[57] A. Carrington and P. Sarre. Electronic absorption spectrum of CO$^+$ in an ion beam. *Molecular Physics*, 33:1495–1497, May 1977. doi: 10.1080/00268977700101251.

[58] J. Gauss and C. Puzzarini. Quantum-chemical calculation of Born-Oppenheimer breakdown parameters to rotational constants. *Molecular Physics*, 108:269–277, February 2010. doi: 10.1080/00268970903433507.

[59] C. Puzzarini and J. Gauss. Quantum-chemical determination of Born-Oppenheimer breakdown parameters for rotational constants: the open-shell species CN, CO$^+$ and BO. *Molecular Physics*, 2013. doi: 10.1080/00268976.2013.797614.

[60] T. George, W. Urban, and A. Lefloch. Improved Mass-Independent Dunham Parameters for the Ground State of CO and Calibration Frequencies for the Fundamental Band. *Journal of Molecular Spectroscopy*, 165:500–505, June 1994. doi: 10.1006/jmsp.1994.1153.

[61] A. H. Saleck, R. Simon, and G. Winnewisser. Interstellar CN rotational spectra: ^{12}C^{15}N. *ApJ*, 436:176–182, November 1994. doi: 10.1086/174890.

[62] H. S. P. Müller, M. C. McCarthy, L. Bizzocchi, H. Gupta, S. Esser, H. Lichau, M. Caris, F. Lewen, J. Hahn, C. Degli Esposti, S. Schlemmer, and P. Thaddeus. Rotational spectroscopy of the isotopic species of silicon monosulfide, SiS. *Physical Chemistry Chemical Physics (Incorporating Faraday Transactions)*, 9:1579, 2007. doi: 10.1039/b618799d.

[63] R. Kępa, A. Kocan, M. Ostrowska-Kopeć, I. Piotrowska-Domagała, and M. Zachwieja. New spectroscopic studies of the Comet Tail ($A^2\Pi_i$ $X^2\Sigma^+$) system of the CO^+ molecule. *Journal of Molecular Spectroscopy*, 228:66–75, November 2004. doi: 10.1016/j.jms.2004.06.014.

[64] T. A. Bell, W. Whyatt, S. Viti, and M. P. Redman. A search for CO^+ in planetary nebulae. *MNRAS*, 382:1139–1144, December 2007. doi: 10.1111/j.1365-2966.2007.12398.x.

[65] R. T. Garrod, S. L. W. Weaver, and E. Herbst. Complex Chemistry in Star-forming Regions: An Expanded Gas-Grain Warm-up Chemical Model. *ApJ*, 682:283–302, July 2008. doi: 10.1086/588035.

[66] E. A. Bergin and M. Tafalla. Cold Dark Clouds: The Initial Conditions for Star Formation. *ARA&A*, 45:339–396, September 2007. doi: 10.1146/annurev.astro.45.071206.100404.

[67] M. Guelin, W. D. Langer, R. L. Snell, and H. A. Wootten. Observations of DCO^+ - The electron abundance in dark clouds. *ApJ*, 217:L165–L168, November 1977. doi: 10.1086/182562.

[68] P. Caselli, C. M. Walmsley, A. Zucconi, M. Tafalla, L. Dore, and P. C. Myers. Molecular Ions in L1544. II. The Ionization Degree. *ApJ*, 565:344–358, January 2002. doi: 10.1086/324302.

[69] S. Cazaux, P. Caselli, and M. Spaans. Interstellar Ices as Witnesses of Star Formation: Selective Deuteration of Water and Organic Molecules Unveiled. *ApJ*, 741:L34, November 2011. doi: 10.1088/2041-8205/741/2/L34.

[70] V. Taquet, C. Ceccarelli, and C. Kahane. Formaldehyde and Methanol Deuteration in Protostars: Fossils from a Past Fast High-density Pre-collapse Phase. *ApJ*, 748:L3, March 2012. doi: 10.1088/2041-8205/748/1/L3.

[71] C. Ceccarelli, P. Caselli, E. Herbst, A. G. G. M. Tielens, and E. Caux. Extreme Deuteration and Hot Corinos: The Earliest Chemical Signatures of Low-Mass Star Formation. *Protostars and Planets V*, pages 47–62, 2007.

[72] H. Roberts, E. Herbst, and T. J. Millar. The importance of new rate coefficients for deuterium fractionation reactions in interstellar chemistry. *MN-RAS*, 336:283–290, October 2002. doi: 10.1046/j.1365-8711.2002.05738.x.

[73] E. Roueff, E. Herbst, D. C. Lis, and T. G. Phillips. The Effect of an Increased Elemental D/H Ratio on Deuterium Fractionation in the Cold Interstellar Medium. *ApJ*, 661:L159–L162, June 2007. doi: 10.1086/518863.

[74] H. Roberts, E. Herbst, and T. J. Millar. The chemistry of multiply deuterated species in cold, dense interstellar cores. *A&A*, 424:905–917, September 2004. doi: 10.1051/0004-6361:20040441.

[75] H. Roberts and T. J. Millar. Gas-phase formation of doubly-deuterated species. *A&A*, 364:780–784, December 2000.

[76] Y. Aikawa, E. Herbst, H. Roberts, and P. Caselli. Molecular Evolution in Collapsing Prestellar Cores. III. Contraction of a Bonnor-Ebert Sphere. *ApJ*, 620:330–346, February 2005. doi: 10.1086/427017.

[77] B. E. Turner. Detection of doubly deuterated interstellar formaldehyde (D_2CO) - an indicator of active grain surface chemistry. *ApJ*, 362:L29–L33, October 1990. doi: 10.1086/185840.

[78] D. C. Lis, E. Roueff, M. Gerin, T. G. Phillips, L. H. Coudert, F. F. S. van der Tak, and P. Schilke. Detection of Triply Deuterated Ammonia in the Barnard 1 Cloud. *ApJ*, 571:L55–L58, May 2002. doi: 10.1086/341132.

[79] J. L. Linsky, A. Brown, K. Gayley, A. Diplas, B. D. Savage, T. R. Ayres, W. Landsman, S. N. Shore, and S. R. Heap. Goddard high-resolution spectrograph observations of the local interstellar medium and the deuterium/hydrogen ratio along the line of sight toward Capella. *ApJ*, 402:694–709, January 1993. doi: 10.1086/172170.

[80] C. Ceccarelli, A. Castets, L. Loinard, E. Caux, and A. G. G. M. Tielens. Detection of doubly deuterated formaldehyde towards the low-luminosity protostar IRAS 16293-2422. *A&A*, 338:L43–L46, October 1998.

[81] B. Parise, A. Castets, E. Herbst, E. Caux, C. Ceccarelli, I. Mukhopadhyay, and A. G. G. M. Tielens. First detection of triply-deuterated methanol. *A&A*, 416:159–163, March 2004. doi: 10.1051/0004-6361:20034490.

[82] A. Dalgarno and S. Lepp. Deuterium fractionation mechanisms in interstellar clouds. *ApJ*, 287:L47–L50, December 1984. doi: 10.1086/184395.

[83] P. Caselli, C. M. Walmsley, M. Tafalla, L. Dore, and P. C. Myers. CO Depletion in the Starless Cloud Core L1544. *ApJ*, 523:L165–L169, October 1999. doi: 10.1086/312280.

[84] H. Roberts, E. Herbst, and T. J. Millar. Enhanced Deuterium Fractionation in Dense Interstellar Cores Resulting from Multiply Deuterated H_3^+. *ApJ*, 591:L41–L44, July 2003. doi: 10.1086/376962.

[85] C. Vastel, T. G. Phillips, and H. Yoshida. Detection of D_2H^+ in the Dense Interstellar Medium. *ApJ*, 606:L127–L130, May 2004. doi: 10.1086/421265.

[86] B. Parise, E. Caux, A. Castets, C. Ceccarelli, L. Loinard, A. G. G. M. Tielens, A. Bacmann, S. Cazaux, C. Comito, F. Helmich, C. Kahane, P. Schilke, E. van Dishoeck, V. Wakelam, and A. Walters. HDO abundance in the envelope of the solar-type protostar IRAS 16293-2422. *A&A*, 431:547–554, February 2005. doi: 10.1051/0004-6361:20041899.

[87] H. M. Butner, S. B. Charnley, C. Ceccarelli, S. D. Rodgers, J. R. Pardo, B. Parise, J. Cernicharo, and G. R. Davis. Discovery of Interstellar Heavy Water. *ApJ*, 659:L137–L140, April 2007. doi: 10.1086/517883.

[88] E. Roueff, D. C. Lis, F. F. S. van der Tak, M. Gerin, and P. F. Goldsmith. Interstellar deuterated ammonia: from NH_3 to ND_3. *A&A*, 438:585–598, August 2005. doi: 10.1051/0004-6361:20052724.

[89] C. Vastel, T. G. Phillips, C. Ceccarelli, and J. Pearson. First Detection of Doubly Deuterated Hydrogen Sulfide. *ApJ*, 593:L97–L100, August 2003. doi: 10.1086/378261.

[90] N. Marcelino, J. Cernicharo, E. Roueff, M. Gerin, and R. Mauersberger. Deuterated Thioformaldehyde in the Barnard 1 Cloud. *ApJ*, 620:308–320, February 2005. doi: 10.1086/426934.

[91] W. D. Geppert, M. Hamberg, R. D. Thomas, F. Österdahl, F. Hellberg, V. Zhaunerchyk, A. Ehlerding, T. J. Millar, H. Roberts, J. Semaniak, M. A. Ugglas, A. Källberg, A. Simonsson, M. Kaminska, and M. Larsson. Dissociative recombination of protonated methanol. *Faraday Discussions*, 133: 177, 2006. doi: 10.1039/b516010c.

[92] A. Luca, D. Voulot, and D. Gerlich. Low temperature reactions between stored ions and condensable gases: formation of protonated methanol via radiative association. *WDS'02 Proceedings of contributed papers*, 2002.

[93] N. Watanabe and A. Kouchi. Efficient Formation of Formaldehyde and Methanol by the Addition of Hydrogen Atoms to CO in H_2O-CO Ice at 10 K. *ApJ*, 571:L173–L176, June 2002. doi: 10.1086/341412.

[94] A. G. G. M. Tielens. Surface chemistry of deuterated molecules. *A&A*, 119: 177–184, March 1983.

[95] I. H. Park, V. Wakelam, and E. Herbst. Modeling the ortho-to-para abundance ratio of cyclic C_3H_2 in cold dense cores. *A&A*, 449:631–639, April 2006. doi: 10.1051/0004-6361:20054420.

[96] Q. Wu, Q. Cheng, Y. Yamaguchi, Q. Li, and H. F. Schaefer. Triplet states of cyclopropenylidene and its isomers. *J. Chem. Phys.*, 132(4):044308, January 2010. doi: 10.1063/1.3273321.

[97] S. Spezzano, F. Tamassia, S. Thorwirth, P. Thaddeus, C. A. Gottlieb, and M. C. McCarthy. A High-resolution Isotopic Study of the Rotational Spectrum of c-C_3H_2. *ApJS*, 200:1, May 2012. doi: 10.1088/0067-0049/200/1/1.

[98] F. J. Lovas, R. D. Suenram, T. Ogata, and S. Yamamoto. Microwave spectra and electric dipole moments for low-J levels of interstellar radicals: SO, C_2S, C_3S, c-HC_3, CH_2CC, and c-C_3H_2. *ApJ*, 399:325–329, November 1992. doi: 10.1086/171928.

[99] P. Thaddeus, M. Guelin, and R. A. Linke. Three new 'nonterrestrial' molecules. *ApJ*, 246:L41–L45, May 1981. doi: 10.1086/183549.

[100] P. Thaddeus, J. M. Vrtilek, and C. A. Gottlieb. Laboratory and astronomical identification of cyclopropenylidene, C_3H_2. *ApJ*, 299:L63–L66, December 1985. doi: 10.1086/184581.

[101] C. A. Gottlieb, J. M. Vrtilek, E. W. Gottlieb, P. Thaddeus, and A. Hjalmarson. Laboratory detection of the C_3H radical. *ApJ*, 294:L55–L58, July 1985. doi: 10.1086/184508.

[102] P. Cox, R. Guesten, and C. Henkel. Detection of the hydrocarbon ring molecule C_3H_2 in the planetary nebula NGC 7027. *A&A*, 181:L19–L22, July 1987.

[103] S. C. Madden, W. M. Irvine, D. A. Swade, H. E. Matthews, and P. Friberg. A survey of cyclopropenylidene (C3H2) in Galactic sources. *AJ*, 97:1403–1422, May 1989. doi: 10.1086/115081.

[104] R. Lucas and H. S. Liszt. Comparative chemistry of diffuse clouds. I. C_2H and C_3H_2. *A&A*, 358:1069–1076, June 2000.

[105] M. Gerin, H. A. Wootten, F. Combes, F. Boulanger, W. L. Peters, III, T. B. H. Kuiper, P. J. Encrenaz, and M. Bogey. Deuterated C_3H_2 as a clue to deuterium chemistry. *A&A*, 173:L1–L4, February 1987.

[106] M. C. McCarthy, M. J. Travers, A. Kovacs, C. A. Gottlieb, and P. Thaddeus. Eight New Carbon Chain Molecules. *ApJS*, 113:105, November 1997. doi: 10.1086/313050.

[107] C. A. Gottlieb, P. C. Myers, and P. Thaddeus. Precise Millimeter-Wave Laboratory Frequencies for CS and $C^{34}S$. *ApJ*, 588:655–661, May 2003. doi: 10.1086/368378.

[108] E. Herbst and C. M. Leung. Gas-phase production of complex hydrocarbons, cyanopolyynes, and related compounds in dense interstellar clouds. *ApJS*, 69:271–300, February 1989. doi: 10.1086/191314.

[109] E. Keto and P. Caselli. Dynamics and depletion in thermally supercritical starless cores. *MNRAS*, 402:1625–1634, March 2010. doi: 10.1111/j. 1365-2966.2009.16033.x.

[110] S. Schnee, P. Caselli, A. Goodman, H. G. Arce, J. Ballesteros-Paredes, and K. Kuchibhotla. TMC-1C: An Accreting Starless Core. *ApJ*, 671:1839–1857, December 2007. doi: 10.1086/521577.

[111] M. B. Bell, L. W. Avery, H. E. Matthews, P. A. Feldman, J. K. G. Watson, S. C. Madden, and W. M. Irvine. A study of C_3HD in cold interstellar clouds. *ApJ*, 326:924–930, March 1988. doi: 10.1086/166150.

[112] D. Ward-Thompson, F. Motte, and P. Andre. The initial conditions of isolated star formation - III. Millimetre continuum mapping of pre-stellar cores. *MNRAS*, 305:143–150, May 1999. doi: 10.1046/j.1365-8711.1999. 02412.x.

[113] J. Pety. Successes of and Challenges to GILDAS, a State-of-the-Art Radioas-
tronomy Toolkit. In F. Casoli, T. Contini, J. M. Hameury, and L. Pagani,
editors, *SF2A-2005: Semaine de l'Astrophysique Francaise*, page 721, De-
cember 2005.

[114] T. L. Wilson and R. Rood. Abundances in the Interstellar Medium. *ARA&A*,
32:191–226, 1994. doi: 10.1146/annurev.aa.32.090194.001203.

[115] M. Bogey, C. Demuynck, J. L. Destombes, and H. Dubus. Molecular struc-
ture of cyclopropenylidene, H-CCC-H from the millimeter wave spectra of
its isotopomers. *Journal of Molecular Spectroscopy*, 122:313–324, April 1987.
doi: 10.1016/0022-2852(87)90007-5.

[116] Y. Aikawa, V. Wakelam, F. Hersant, R. T. Garrod, and E. Herbst. From
Prestellar to Protostellar Cores. II. Time Dependence and Deuterium Frac-
tionation. *ApJ*, 760:40, November 2012. doi: 10.1088/0004-637X/760/1/40.

[117] A. Crapsi, P. Caselli, C. M. Walmsley, P. C. Myers, M. Tafalla, C. W.
Lee, and T. L. Bourke. Probing the Evolutionary Status of Starless Cores
through N_2H^+ and N_2D^+ Observations. *ApJ*, 619:379–406, January 2005.
doi: 10.1086/426472.

[118] A. Bacmann, B. Lefloch, C. Ceccarelli, J. Steinacker, A. Castets, and
L. Loinard. CO Depletion and Deuterium Fractionation in Prestellar Cores.
ApJ, 585:L55–L58, March 2003. doi: 10.1086/374263.

[119] S. Tiné, E. Roueff, E. Falgarone, M. Gerin, and G. Pineau des Forêts. Deu-
terium fractionation in dense ammonia cores. *A&A*, 356:1039–1049, April
2000.

[120] R. Y. Shah and A. Wootten. Deuterated Ammonia in Galactic Protostellar
Cores. *ApJ*, 554:933–947, June 2001. doi: 10.1086/321396.

[121] T. J. Millar. Modelling deuterium fractionation in interstellar clouds.
Planet. Space Sci., 50:1189–1195, October 2002. doi: 10.1016/
S0032-0633(02)00082-X.

[122] P. Caselli, C. Vastel, C. Ceccarelli, F. F. S. van der Tak, A. Crapsi, and
A. Bacmann. Survey of ortho-H_2D^+ $(1_{1,0}-1_{1,1})$ in dense cloud cores. *A&A*,
492:703–718, December 2008. doi: 10.1051/0004-6361:20079009.

[123] B. J. McCall, T. R. Geballe, K. H. Hinkle, and T. Oka. Observations of H_3^+ in Dense Molecular Clouds. *ApJ*, 522:338–348, September 1999. doi: 10.1086/307637.

[124] X. Huang and T. J. Lee. Spectroscopic Constants for ^{13}C and Deuterium Isotopologues of Cyclic and Linear $C_3H_3^+$. *ApJ*, 736:33, July 2011. doi: 10.1088/0004-637X/736/1/33.

[125] R. A. Seburg, E. V. Patterson, J. F. Stanton, and R. J. McMahon. Structures, Automerizations, and Isomerizations of C_3H_2 Isomers. *Journal of the American Chemical Society*, 119, 1997.

[126] J. M. Vrtilek, . A. Gottlieb, E. W. Gottlieb, T. C. Killian, and P. Thaddeus. Laboratory detection of propadienylidene, H_2CCC. *ApJ*, 364:L53–L56, December 1990. doi: 10.1086/185873.

[127] J. Cernicharo, C. A. Gottlieb, M. Guelin, T. C. Killian, G. Paubert, P. Thaddeus, and J. M. Vrtilek. Astronomical detection of H_2CCC. *ApJ*, 368:L39–L41, February 1991. doi: 10.1086/185943.

[128] K. Kawaguchi, N. Kaifu, M. Ohishi, S.-I. Ishikawa, Y. Hirahara, S. Yamamoto, S. Saito, S. Takano, A. Murakami, J. M. Vrtilek, C. A. Gottlieb, P. Thaddeus, and W. M. Irvine. Observations of cumulene carbenes, H_2CCCC and H_2CCC, in TMC-1. *PASJ*, 43:607–619, August 1991.

[129] D. Teyssier, P. Hily-Blant, M. Gerin, J. Cernicharo, E. Roueff, and J. Pety. Variation of the C_3H_2 cyclic/linear abundance ratio across the Horsehead nebula Photo-Dominated Region. In A. Wilson, editor, *ESA Special Publication*, volume 577 of *ESA Special Publication*, pages 423–424, January 2005.

[130] H. Liszt, P. Sonnentrucker, M. Cordiner, and M. Gerin. The Abundance of C_3H_2 and Other Small Hydrocarbons in the Diffuse Interstellar Medium. *ApJ*, 753:L28, July 2012. doi: 10.1088/2041-8205/753/2/L28.

[131] D. L. Cooper and S. C. Murphy. AB Initio Geometries for $C_{2n+1}H$, $C_{2n+1}H^+$, and $C_{2n+1}H_2$ Species for N = 1,2,3. *ApJ*, 333:482, October 1988. doi: 10.1086/166761.

[132] D. J. Defrees and A. D. McLean. Ab initio molecular orbital studies of low-energy, metastable isomers of the ubiquitous cyclopropenylidene. *ApJ*, 308: L31–L35, September 1986. doi: 10.1086/184738.

[133] J. Cernicharo, P. Cox, D. Fossé, and R. Güsten. Detection of linear C_3H_2 in absorption toward continuum sources. *A&A*, 351:341–346, November 1999.

[134] N. G. Adams and D. Smith. On the synthesis of c-C_3H_2 in interstellar clouds. *ApJ*, 317:L25–L27, June 1987. doi: 10.1086/184906.

[135] D. Talbi. A Quantum Chemical Study of the Dissociative Recombination of $C_3H_3^+$ - The Formation of Interstellar C_3H_2. In *IAU Symposium*, volume 235 of *IAU Symposium*, page 176P, 2005.

[136] J. P. Maier, G. A. H. Walker, D. A. Bohlender, F. J. Mazzotti, R. Raghunandan, J. Fulara, I. Garkusha, and A. Nagy. Identification of H_2CCC as a Diffuse Interstellar Band Carrier. *ApJ*, 726:41, January 2011. doi: 10.1088/0004-637X/726/1/41.

[137] E. Kim and S. Yamamoto. Rotational spectra of the deuterated carbon chain molecules: C_3D, C_4D, C_3HD, and C_4HD. *Journal of Molecular Spectroscopy*, 233:93–97, September 2005. doi: 10.1016/j.jms.2005.05.010.

[138] S. Spezzano, S. Brünken, P. Schilke, P. Caselli, K. M. Menten, M. C. McCarthy, L. Bizzocchi, S. P. Treviño-Morales, Y. Aikawa, and S. Schlemmer. Interstellar Detection of c-C_3D_2. *ApJ*, 769:L19, June 2013. doi: 10.1088/2041-8205/769/2/L19.

[139] L. Bizzocchi, P. Caselli, E. Leonardo, and L. Dore. Detection of $^{15}NNH^+$ in L1544: non-LTE modelling of dyazenilium hyperfine line emission and accurate $^{14}N/^{15}N$ values. *A&A*, 555:A109, July 2013. doi: 10.1051/0004-6361/201321276.

Acknowledgements

I am grateful to my supervisor Prof. Schlemmer for having given me the opportunity to join his group 4 years ago, and to perform such an exciting and challenging research. I am also very thankful to my thesis committee: Prof. Menten, Prof. Schilke and Dr. Brünken for the care taken of my work. I wish to thank the whole Laboratory Astrophysics group at the I. Physikalisches Institut, in particular my officemates: Lars, Sabrina, Doris and Marius. I cherished the moments we shared, and I am thankful for the company and support over the last 4 years. During the last years I had the chance to collaborate with many great scientists that helped me a lot: the whole Cologne spectroscopy group (in particular Holger, Monika, Frank and Doris), Michael McCarthy, Carl Gottlieb, Valerio Lattanzi, Luca Bizzocchi, Paola Caselli and Yuri Aikawa. A owe a particular thank to Monika and Şenol for revising very carefully my whole thesis, and to Sandra for having guided me in the last four years.

I thank the IMPRS, and in particularly Manolis, its pulsating hearth, for the support. Being a chemist in a graduate school of astronomers has contributed a lot to the results listed in my thesis. A part from the scientific growth, the IMPRS has given me the opportunity to meet great people that are now a part of my "german family": Angela, Banafsheh, Monica, Nadeen, Hananeh, Lilia, Nico, Giannis (the first, the second and the third!), Jeff, Matteo, Arti, Patrick, and the whole IMPRS community.. I fell so lucky I met you all!

Non posso non ringraziare tutti i miei amici "bolognesi"! Sono passati 5 anni da quando sono partita, eppure siete sempre al mio fianco. Grazie di tutto l'amore e il supporto incondizionato (lo so che vi state ancora chiedendo che ci faccio con le molecole e i telescopi)! É strano pensare di finire una tappa universitaria senza una delle famose e famigerate feste open-bar di Chimica Industriale, cosí come é stato strano passare tutto questo tempo senza una grigliata sui colli, o una birretta in piazza San Francesco.. ma quando ripasso per Bologna siete tutti invitati per un amaro al Pratello! :)

Grazie al Nive e alla Franca per il supporto e l'affetto.

Grazie anche alla mia brand new "famiglia tedesca"! Grazie alle mie ragazze: Mari, Nini, Diana, Elisa e Matilde per la dolcezza e la compagnia. Thanks to Rosaria, Silvia, Dela, Piroz, Forugh, Melissa, Flo, Vicky, Yvonne, Kasia, Luca, Bene, Sabsi and the little Milosz and Karl.

Grazie a Davide, Nunzia, Filippo e Alfredo per un'amicizia ventennale!

Grazie a Şenol, che mi ha preso la mano e non l'ha piú lasciata andare.

Ultimi, ma sempre primi nel mio cuore, grazie a mamma, papá , Giulio e Ale per tutto.

Erklärung

Ich versichere, dass ich die von mir vorgelegte Dissertation selbständig angefertigt, die benutzten Quellen und Hilfsmittel vollständig angegeben und die Stellen der Arbeit – einschließlich Tabellen, Karten und Abbildungen –, die anderen Werken im Wortlaut oder dem Sinn nach entnommen sind, in jedem Einzelfall als Entlehnung kenntlich gemacht habe; dass diese Dissertation noch keiner anderen Fakultät oder Universität zur Prüfung vorgelegen hat; dass sie – abgesehen von unten angegebenen Teilpublikationen – noch nicht veröffentlicht worden ist sowie, dass ich eine solche Veröffentlichung vor Abschluß des Promotionsverfahrens nicht vornehmen werde. Die Bestimmungen dieser Promotionsordnung sind mir bekannt. Die von mir vorgelegte Dissertation ist von Prof. Dr. Stephan Schlemmer betreut worden.

Teilpublikationen

Spezzano, S.; Brünken, S.; Müller, H. S. P.; Klapper, G.; Lewen, F.; Menten, K M.; Schlemmer, S.
"High-N Rest Frequencies of CO^+: an Ideal Tracer of Photon-Dominated Regions"
Journal of Physical Chemistry A, 2013, 117, 9814

Spezzano, S.; Brünken, S.; Schilke, P.; Caselli, P.; Menten, K. M.; McCarthy, M. C.; Bizzocchi, L.; Trevino-Morales S. P.; Aikawa, Y; Schlemmer, S.
"Interstellar detection of c-C_3D_2"
Astrophysical Journal Letters, 2013, 769, L19

Weitere Publikationen

Müller, H. S. P.; **Spezzano, S.**; Bizzocchi, L.; Gottlieb, C. A.; Degli Esposti, C.; McCarthy, M. C.
"Rotational Spectroscopy of Isotopologues of Silicon Monoxide, SiO, and Spectroscopic Parameters from a Combined Fit of Rotational and Rovibrational Data"
Journal of Physical Chemistry A, 2013, accepted

Spezzano, S.; Tamassia, F.; Thorwirth, S.;Thaddeus, P.; Gottlieb, C. A. and McCarthy, M. C.
"A high resolution Isotopic Study of the Rotational Spectrum of c-C_3H_2"
Astrophysical Journal Supplement Series, 2012, 200, 1

Neill, J. L.; Muckle, M. T.; Zaleski, D. P.;Steber, A.; Pate, B. H.; Lattanzi, V.; **Spezzano**, S.; McCarthy, M. C.; Remijan, A. J.
"Laboratory and Tentative Interstellar Detection of Trans-Methyl Formate Using the Publicly Available Green Bank Telescope Primos Survey"
Astrophysical Journal, 2012, 755, 153

Neill, J. L.; Steber, A.; Muckle, M. T.; Zaleski, D. P.; Lattanzi, V.; **Spezzano**, S.; McCarthy, M. C.; Remijan, A. J.; Friedel, D. N.; Widicus Weaver, S.; Pate, B. H.
"Spatial Distributions and Interstellar Reaction Processes"
The Journal of Physical Chemistry A, 2011, 115, 6472

Fusinal, L.,; Nivellini, G.; and **Spezzano**, S.
"The ν1 and ν3 band system of $^{15}NH_3$"
Molecular Physics, 2011, 109, 2209

Lebenslauf

Persönliche Angaben

Name:	Silvia Spezzano
Anschrift:	Luxemburger Str. 316
	50937 Köln, Deutschland
Email:	spezzano@ph1.uni-koeln.de
Geburtsort:	Corigliano Calabro, Italien
Geburtsdatum:	17 Mai 1985

Ausbildung

Seit März 2010	Promotionstudentin
	I. Physikalisches Institut der Universität zu Köln
	IMPRS-studentin am Max-Planck-Institut für Radioastronomie
	Köln, Deutschland
Feb 2009 - Jan 2010	Pre-Doctoral Fellow
	Harvard Smithsonian Center for Astrophysics
	Cambridge (MA), USA
2006 - 2008	Master in Chemie
	Universitá degli Studi di Bologna
	Bologna, Italien
2003 - 2006	Bachelor in Chemie
	Universitá degli Studi di Bologna
	Bologna, Italien

Stipendium

Feb 2009 - Jan 2010	Stipendium Fondazione Toso Montanari
Mär 2010 - Feb 2013	Stipendium der "International Max Planck Research School
	IMPRS for Astronomy and Astrophysics"
Mär 2013 - Jun 2013	Stipendium Fondazione Angelo della Riccia

Köln, Oktober 2013